USDOT Tier 1
University Transportation Center
on Improving Rail Transportation
Infrastructure Sustainability and Durability

Final Report UNLV-3

NON-CONTACT ACOUSTIC EMISSION APPROACH FOR RAIL HEALTH MONITORING

By

Lei Jia, Graduate Research Assistant
Jee Woong Park, Ph.D., Associate Professor
Department of Civil and Environmental Engineering and Construction

Ming Zhu, Ph.D., Lab Director
Yingtao Jiang, Ph.D., Professor
Lihao Qiu, Graduate Research Assistant
Department of Electrical and Computer Engineering

and

Hualiang (Harry) Teng, Professor
Department of Civil and Environmental Engineering and Construction

\
Date: July 2024
Grant Number: 69A3551747132

DISCLAIMER

The contents of this report reflect the views of the authors, who are responsible for the facts and the accuracy of the information presented herein. This document is disseminated in the interest of information exchange. The report is funded, partially or entirely, by a grant from the U.S. Department of Transportation's University Transportation Centers Program. However, the U.S. Government assumes no liability for the contents or use thereof.

ABSTRACT

Rail defects, whether internal or external, present significant safety risks. Acoustic Emission (AE) technology has emerged as a promising technique for monitoring damage progression and detecting these rail defects. This project addresses this critical concern by testing two different AE detection systems: 1) bone-conduct sensors for contact-based AE detection, and 2) air-coupled optical microphones for non-contact AE detection. The goal of the project is to investigate AE signal propagation using both rail-mounted and vehicle-mounted methods, enhancing our understanding of AE signals in relation to defects and their effectiveness in identifying them.

The first phase of the study focused on developing and testing a prototype detection system using bone-conduct sensors. Initial field tests were conducted at the Nevada Railroad Museum, where the test track featured two pre-damaged internal welding defects. Subsequent evaluations followed at the Transportation Technology Center Inc. (TTCI) in Colorado, involving three rail loops with various defects. These tests were particularly designed to assess the prototype's performance under different conditions, including varying speeds and defect types. However, the bone-conduct sensors proved inadequate for detecting AE signals when mounted on moving vehicles, necessitating a shift in approach.

In the second phase, the research transitioned to implementing air-coupled optical microphones within the prototype system. This non-contact rail health monitoring technique leverages AE technology to detect defects without the need for direct contact with the rail. Laboratory tests under controlled conditions were conducted to evaluate the attenuation characteristics of AE signals in various scenarios. Subsequently, real-world field tests at the Nevada Railroad Museum and TTCI were performed to assess the capability of the system installed on a moving train in detecting internal and external rail defects

The results from both lab and field tests were promising for detecting internal defects as the non-contact sensor system effectively captured AE signals related to these defects, indicating its potential as a real-time rail health monitoring without disrupting train operations. However, the detection of external defects presented low performance due to indistinct signal propagation characteristics and significant environmental noise. Further application of continuous wavelet transforms (CWT) and wavelet packet power (WPP) analysis presented more results by identifying energy distributions and frequency peaks associated with defect types. Although these methods enhanced the detection of external defects, additional research is required to refine the identification process.

In conclusion, the findings offer valuable insights into the development of more effective and reliable AE-based monitoring solutions. They highlight the current capabilities of these systems in detecting different types of defects, ultimately contributing to improved railway safety and maintenance efficiency.

Keyword: railroad infrastructure, rail defect detection, rail health monitoring, wavelet analysis, acoustic emission detection

TABLE OF CONTENTS

LIST OF FIGURES

LIST OF TABLES

CHAPTER 1: INTRODUCTION

1.1 Background

In railroad transportation, the rail and wheels directly interact while trains move forward (Figure 1). The railroads would experience wear and tear during daily operations, leading to defects both internally and on its surface.

Head checks at higher side

Side shells corrosion

Flaking caused by centralized loading

Thermal cracks on burned stock railhead

Figure 2 Rail Surface Defects (Office of Railroad Safety, 2015)

Transverse fissure

Vertical split head

Defective weld with slag entrapment

Piped Rail

Figure 3 Rail Internal Defects (Office of Railroad Safety, 2015)

presents external defects such as head checks at the higher side, side shell corrosion, flaking caused by centralized loading, and thermal cracks on burned stock railheads. Internal defects include transverse fissure, vertical split head, defective weld with slag entrapment, and piped rail as shown in

Figure 3. Internal defects are invisible from the exterior.

Figure 1 Rail Wheel Interaction (Elements, 2019)

Head checks at higher side

Side shells corrosion

Flaking caused by centralized loading

Thermal cracks on burned stock railhead

Figure 2 Rail Surface Defects (Office of Railroad Safety, 2015)

Transverse fissure

Vertical split head

Defective weld with slag entrapment

Piped Rail

Figure 3 Rail Internal Defects (Office of Railroad Safety, 2015)

1.2 Rail Surface Defect Detection

Currently, various inspection and detection technologies, including imaging and ultrasound detection, have been applied to monitor rail surface health conditions against rail defects. In addition, some unique methods, such as field hammer test measurements and electromagnetic tomography technology, have been proposed for addressing specific detection problems. The following sections will provide an overview of these techniques for surface defect inspection.

1.2.1 Optical Imaging Technologies

The optical imaging method is a recognition technology that uses graphics scanning and processing. The core component of this testing system is a high-speed, high-resolution camera. An optical encoder is used for graphics recognition and classification. Recent experimental research has demonstrated surface defect detection at speeds over 135 mph (Li & Ren, 2012). An automatic optical detecting system can detect flaws using color line-scan cameras and a spectral image differencing procedure (Deutschl et al., 2004). This system is particularly advantageous for detecting minor defects, including invisible cracks. Also, the employment of the system enables automation of about 95% of the inspection work, significantly increasing the efficiency of inspection compared to previous techniques. However, the system is limited to only inline checking of new rails. Advances in software for optical detection have been made. A new algorithm filters the image background through wavelet transformation (Bojarczak, 2013; He et al., 2016).

Advanced optical technologies include a 3D laser profiling system (3D-LPS) (Xiong et al., 2017). The system contains a laser scanner, odometer, inertial measurement unit (IMU), and GPS to collect the rail surface information. The results showed that the algorithm could recognize the surface defect and locate the defect area with a relatively good recognition rate. However, the whole experiment was performed in limited setting at approximately 3.4 mph; thus, further

research on the application at higher speeds is necessary for more rigorous validation. While research has improved the optical detection system, several problems still exist, limiting the system-wide implementation. The primary challenges stem from complex disturbance factors, limited recognition features, and limited capability to detect internal defects (Office of Railroad Policy and Development, 2011).

1.2.2 Electromagnetic Methods

Electromagnetic techniques include Eddy current technique and alternative current field measurement methods. Eddy current technique employs electromagnetic induction to inspect rail surfaces (Thomas Heckel, 2009; Thomas et al., 2007). The method involves a magnetic field near the rail, where discontinuities on the rail surface affect the magnitude of the eddy current. The detector collects and recognizes these changes. Studies have shown that the Eddy current technique can be effectively employed at high-speed rails up to 90 km/h. However, the testing devices must be close to the rail surface and are highly sensitive to variations in the lift-off distance.

Alternating current field measurement (ACFM) is one of the non-destructive testing technologies capable of sizing surface-breaking cracks through the disturbance of magnetic field measurements (Papaelias et al., 2010). The technology does not require direct electrical contact with the surface, allowing it to work through many different environments. Research results from various simulated defect conditions suggest ACFM can be employed for accurately and reliably detecting surface-breaking defects at speeds over 150 mph (Papaelias et al., 2010; Sadeghi et al., 2009). The results confirmed that the ACFM sensor could detect visible crack lengths as small as 1.2 mm. However, such techniques still fall short of detecting internal defects, which limit the application in real-world scenarios.

1.2.3 Magnetic Induction Technique

Magnetic-related techniques, such as electromagnetic tomography technology (EMT), are less commonly utilized rail defect detection methods (Liu et al., 2015). This EMT uses a tomographic approach to measure the alternating magnetic signal modulated by cracks in the rail and then reconstructs the distribution of cracks. One of the EMT's advantages is its ability to detect and reconstruct internal cracks within the rail, offering a non-contact, continuous inspection method that can operate at higher speeds compared to traditional inspection techniques.
However, its disadvantages include high costs and the need for specialized expertise to operate the equipment. The system's complexity demands professional knowledge for the proper use and interpretation of the equipment, making it less accessible than other standard inspection methods. Additionally, the non-encircling sensor structure of EMT must be adapted to the mechanical constraints of rail tracks, such as rail bed mounting clips and turnout junctions, which can complicate sensor installation.

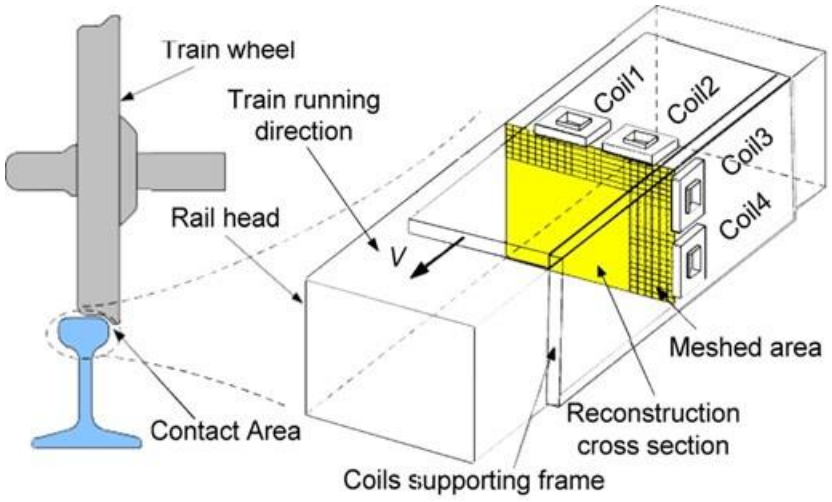

Figure 4 Sensor structure of the EMT rail defect inspection (Liu et al., 2015)

1.3 Rail Internal Defect Detection

Detecting internal defects poses a greater challenge than detecting external defect due to its hidden nature. Although various methods have been proposed in past research, the success has been limited for several reasons. Nonetheless, past proposed methods are reviewed and discussed in the following subsections. In response to the identified challenges and research gaps, a relatively newly applied technique using acoustic technology is also discussed for its potential to detect both external and interior defects.

1.3.1 Non-Contact Ultrasonic (NCU)

This inspection utilizes ultrasonic without having the sensor making direct contact with the material being inspected. While NCU technology is widely used in structure health inspections, past research (Lanza di Scalea et al., 2005) employed pulse-echo for rail scanning with an excitation frequency of approximately 200 kHz. The frequency provided a suitable surface wave mode and sufficient penetration depth for inspection. Concurrently, a spatial averaging technique was employed to remove unusable wave modes and reduce signal complexity. The results demonstrated that the technology worked well on artificial and real defects. Despite these findings, the research suffers a critical limitation with the very low speeds in static conditions, a common drawback of ultrasonic detection methods.

Guided-wave defect detection in rails has also been applied for non-contact testing, and a prototype is under development (Rizzo, 2009). Research has shown that high-frequency waves of approximately 200 kHz are dominant. The penetration depth is related to the wavelength; hence, defect sizing is possible by monitoring different frequency bands of the propagating waves. The researchers at the University of California at San Diego (UCSD) developed a novel non-contact ultrasonic rail inspection system (Mariani et al., 2016). The new system employs a focused air-coupled transmitter, symmetrically placed air-coupled receivers, and a novel statistical algorithm to maximize true outliers (defects) and minimize false positives. Results demonstrate excellent performance at low speeds between 1 and 5 mph and show promise at speeds of 10 and 15 mph.

Laser ultrasonics was proposed as another non-contact detection technique. The laser ultrasonic system employed an Nd-Yag pulse laser for ultrasonic wave generation and a laser Doppler vibrometer for signal measurement (Kim et al., 2012). This study presented the adaptability of laser ultrasonics in defect characterization, with the transformation of the laser beam's shape to cater to different defect types—a line source for surface damage and a point source for internal defects. This method underscores the interaction of ultrasonic waves with defects, enabling the detection of both surface and subsurface anomalies at high speeds.

A passive extraction method has been used to isolate defect signals based on non-contact ultrasonic monitoring (Lanza di Scalea et al., 2018). Three options were listed to present the differences in isolating the defect signal: cross-correlation, normalized cross-correlation, and deconvolution. According to previous research, ultrasonic energy and properties will change due to the rails' discontinuities (Coccia, Bartoli, et al., 2011; Coccia, Phillips, et al., 2011). A defect inspection prototype was developed in the experiment, placing two arrays of air-coupled receivers to collect ultrasonic waves (Figure 5). Normalized cross-correlation and deconvolution operations were used to extract the defect properties during the data analysis. In their discussion, rail lubrication is an uncertain factor that may affect the wheel-rail contact behavior. Meanwhile, many improvements need to be made to increase detection accuracy and faster data analysis.

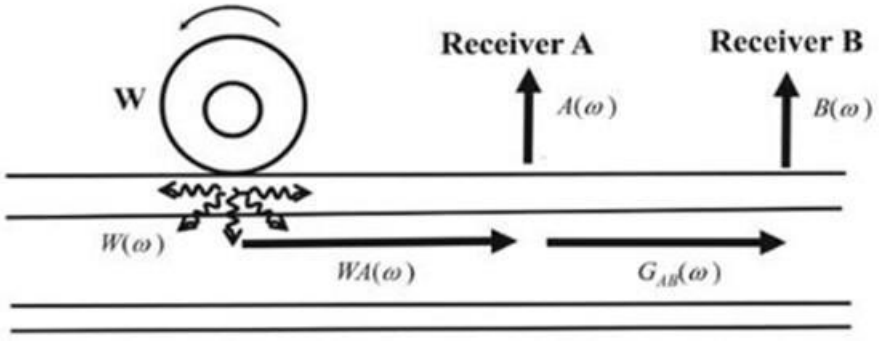

Figure 5 Theoretical consideration of passive extraction of defect information (Lanza di Scalea et al., 2018)

In summary, non-contact ultrasonic detection methods have shown excellent performance in detecting both surface and internal defects. Lab and field tests have demonstrated a high recognition rate in field detection. However, most ultrasonic technologies can only be employed below 25 mph. The inspection rate is the most critical obstacle to ultrasonic detection experimental studies.

1.3.2 AE Techniques and Its Applications

AE is an elastic wave generated by changes in the material's internal structure, which are typically caused by a sudden change in internal stress or external impact (Bruzelius & Mba, 2004; Nivesrangsan et al., 2007). These changes can include crack growth in the body, sectional displacement in material, phase change, fiber breakage, and decomposition.

An AE testing system that can be used for detection of such changes contains bone-conduct sensors, preamplifiers, and a data acquisition (DAQ) system (e.g., control software, data recording devices,

and personal computers). When AE signals are generated due to elastic deformation, sensors respond to the dynamic motion and collect the signals. However, these signals can be too weak to effectively present the AE patterns. In response to this, preamplifiers are used to filter interference signals. The frequency of collected AE signals is generally between 20KHz and 1MHz; a high-pass filter is applied to filter out the ambient noise. After the noise filtering, the signals are transferred to the AE processing equipment for analysis and storage. During signal processing, the signal goes through a measurement circuit that compares the conditioned signals with a threshold voltage value previously programmed. Finally, the signal is recorded into the storage device.

AE technology differs from other non-destructive testing technologies in several aspects (Bruzelius & Mba, 2004; Huang et al., 1998). First, the origin of the signal is different. Instead of providing energy to the object during the examination, AE technology receives the energy released by the material. Second, AE technology only responds to dynamic processes or changes in a material. Dynamic response is critical because it can be used to trace the continuous changes in the material. Through the initial research on AE technology, advantages have been presented, such as the ability to detect rail defects at speeds over 100 mph, easy installation and manipulation, and the ability to monitor internal structural changes (Bruzelius & Mba, 2004; Zhang et al., 2015; Zumpano & Meo, 2006).
Initial research has been conducted to apply AE to rail inspection for rail-track defect diagnosis (Bruzelius & Mba, 2004). Although the research presents only simple experimental tests, the results have demonstrated encouraging potential for further applications. Following this, a series of application studies have been conducted in AE rail defect detection. AE detection of rail defects at high speed based on a rail-wheel test rig was performed in a study (Zhang et al., 2015). The presented results proved that the proposed method could effectively detect rail defects over 77 mph.

Studies were performed on simulated AE sources with different propagation distances, types, and depths for rail defect detection (Zhang et al., 2014). In the study, three simulated AE sources with different frequencies were used on the rail, and the depths of AE sources were changed in the vertical direction. However, due to the limitations in propagation distance, the method only performed well in a very short distance when reflection and mode mixing were not significant. Also, an improved rail defect detection method by multi-level Adaptive Noise Cancellation (ANC) with Variable Step-Size Least Mean Square (VSS-LMS) was presented (Zhang et al., 2018). Multi-level noise cancellation based on Self-Adaptive Noise Cancellation (SANC) and ANC was utilized to eliminate complex noises at high speed. A tongue-shaped curve with an index adjustment factor was proposed to enhance the performance of the variable step-size algorithm. The findings demonstrated the significant development against noise interference at high speeds (over 80 mph). The correlation technique has been researched to investigate the ability of noise cancelation in AE detection (Sadoudi et al., 2016). A series of research studies have been conducted, including active response measurement, noise correlation measurement, sensitivity of detection, and application in rail defect inspection. In noise correlation measurement, a higher correlation was observed with multiple noise sources, making extracting AE signals from ambient noises possible. The isolation experiment presents the characteristics of defect signals that can be extracted and located - proving the possibility of utilizing noise correlation to reconstruct AE signals. It is noted that this study did not discuss the application in running vehicles and extraction of defects in random ambient noises.

Multi-branch convolutional neural network (CNN) was employed to classify rail defects (D. Li et al., 2021). Railroad field and laboratory fatigue tests were performed to collect different types of AE waves. Synchrosequeezed wavelet transform (SWT) was utilized to present the intrinsic characteristics of AE waves in the time-frequency domain. Then, a multi-branch CNN with two branches was developed to identify the different types of AE waves. The results showed that the test accuracy was achieved at 99.52%, and the proposed method was able to detect both surface and internal rail defects.

In summary, traditional AE techniques present the potential to monitor rail health conditions passively. This potential can be understood in several terms: the capability of detecting both internal and external defects, the potential to monitor the development progress of defects, and the classification of defect types. However, due to the utilization of bone-conduct sensors, such an approach can only be installed on the rails due to the requirement of contact. This installation requirement for contact is translated into an extensive network of sensors to cover the wholte rail track where inspection is required. While technically promising, this technique can be practically unfeasible.

1.6 Research Objectives

This research acknowledges past literature and finds AE technology as one of the most promising solutions for detecting internal defects in rail. AE technology can be implemented using bone-conduct sensors and air-coupled optical sensors for rail inspection. The project explores both sensor types through 1) conducting lab tests, small-scale actual rail-train tests, and real-world scale rail-train tests, and 2) analytical studies using various algorithmic investigations to analyze AE signals in relation to defects.

The research is divided into two stages. In the first stage, bone-conduct sensors are deployed on running trains to detect rail defects in real-world tests. This involves an investigation on the characteristics of the rail defect-induced AE signals for defect identification and evaluating the AE characteristics and identification algorithms. The conclusion of the first objective will reveal insights into the bone-conduct sensor-based detection system's feasibility, performance, and potential limitations in automated railroad safety inspections.

In the second stage, air-coupled optical sensors are applied to detect defects on running trains. The tests involve both internal defects and external defects, with follow-up analysis and evaluations focusing on the characteristics of the AE signals induced by both defect types. The conclusion of testing the optical sensors will reveal insights into the air-coupled sensor-based detection system's feasibility, performance, and potential limitations in automated railroad safety inspections.

1.7 Research Gap and Potential Problems

Past research on the application of AE techniques for detecting damage in railway tracks has primarily focused on lab tests and rail-mounted field experiments. These studies include fatigue tests of rail steel specimen experiments with small-scale models to simulate the wheel-rail impact and installing the sensors on the rails to collect AE signals as trains pass by. However, these approaches have limitedly demonstrated potential for real-world applications due to several

constraints. A notable one is the requirement of an extensive network of sensors along the entire length of the railway, which poses significant challenges for real-world implementation. To address these limitations, vehicle-mounted AE techniques proposed in this research are essential for advancing automated rail health monitoring in practical scenarios.

CHAPTER 2: INITIAL INVESTIGATION ON THE RAIL DEFECT DETECTION USING BONE-CONDUCT SENSORS

Previous studies have presented the potential of the AE inspection technique to identify rail defects in lab tests or on-rail field tests. This research extends these findings by implementing AE techniques to monitor rail defects in the on-vehicle field tests. In real-world environments, ambient noise will affect the AE signals more than the data collected in laboratory or stationery on-rail tests. This chapter outlines the performance evaluation in AE rail defect detection using bone-conduct sensors and the exploration of the characteristics of AE signals in on-vehicle scenarios.

2.1 Introduction

As stated above, current research on detecting rail defects with the AE approach focuses primarily on lab tests such as small-scale test rigs and stationary field tests with the sensor fixed on the rail. Conducting real-world field tests with the sensor installed on the train is necessary to study AE signals in environments with ambient noise interference and better understand their characteristics in real-world conditions. Several factors must be considered in on-vehicle tests: (1) In field conditions, the signal-to-noise ratio of AE signals is typically low due to significant ambient noise. Meanwhile, AE signals generated are generally weak when crack growth is in the early stage. When AE signals associated with cracks are covered by ambient noise, additional evaluation is needed to explore the crack-related AE features. (2) Differences between real and Pencil Lead Break (PLB)AE signals: The signal patterns in real-world environments differ from those produced by artificial cracks in lab tests, which are conducted under controlled conditions l. Additionally, PLB sources, commonly used to simulate cracks in laboratory studies, do not accurately represent real cracks in terms of signal intensity, frequency characteristics, and dispersive features (Hamstad, 2007). (3) multiple AE waves: Various AE events might be detected in field conditions due to surface unevenness. For example, surface irregularities can lead to distinct impacts when wheels pass over Rolling Contact Fatigue (RCF) cracks, generating multiple AE transients. While these AE signals can serve as indicators for detecting RCF cracks, it is crucial to accurately differentiate these signals from those generated by crack propagation. Proper identification and separation of these signal sources are essential for precise crack characterization and identification.

In this chapter, an AE testing prototype is developed. Various data analysis techniques, such as fast Fourier transform (FFT) and continuous wavelet transform (CWT), are introduced to explore the characteristics of AE waves. Then, machine learning is introduced to identify the existence of cracks in rail tracks.

2.2 AE Detection Prototype

The prototype developed included data acquisition equipment, bone-conduct sensors, pre-amplifiers, and high-speed cameras (Figure 6). The AE sensors S9215 were employed; the operating bandwidth is 50-650 KHz, with a resonant frequency of 100 kHz. They have a very high limit of working temperature up to 540 ºC, which allows the testing prototype to work properly in the extreme weather conditions in the summertime of Nevada. National Instrumental cRio 9041 with module NI 9223 were utilized as DAQ equipment, the sampling rate was 1 MHz. Mistras

2/4/6 voltage preamplifiers (PAC 2/4/6) were employed to amplify the AE signals before they were recorded by DAQ equipment. The gain was set to 60 dB for all the tests to ensure the AE signal qualities. During the test, the band-pass filter was selected to be 20-500 kHz to eliminate the effects of low-frequency noises unrelated to the AE events. Labview was used to control the data collection and storage (Figure 7). To ensure long-time data recording without interruption, the producer and consumer modules were employed to save current data and keep recording new data simultaneously (Figure 8). A go-pro camera was utilized to record geo-information during the field tests. It provides up to 240 frames video recording. Hammer hit was employed when each test started, to sync the time between video and AE signals.

Figure 6 AE detection prototype

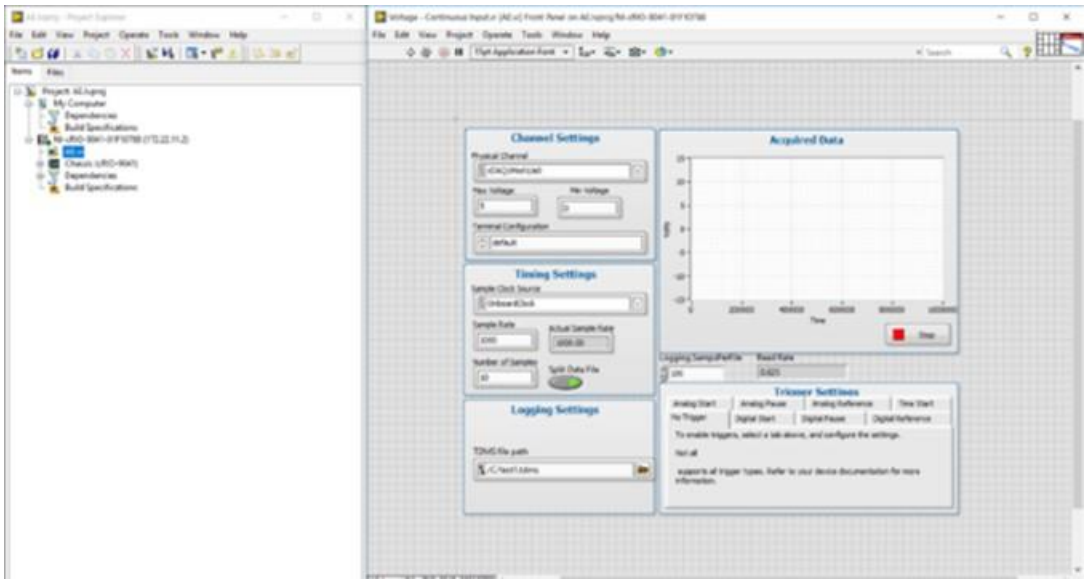

Figure 7 LabVIEW interface

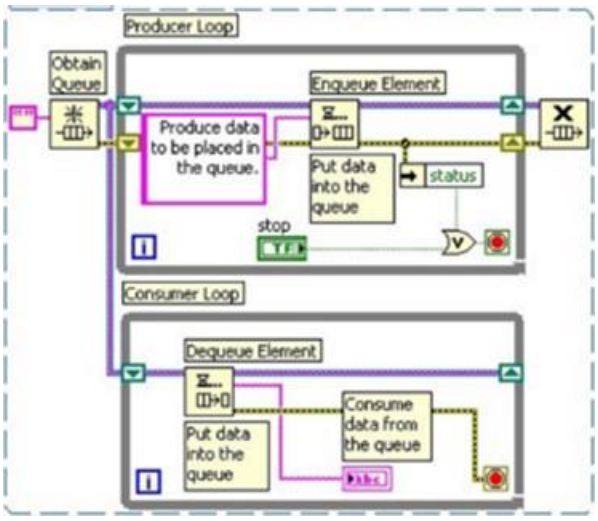

Figure 8 Producer & Consumer module in LabVIEW

2.3 Field Test Setup

To assess the feasibility of installing the AE sensors on the train to detect rail defects, on-vehicle field tests were conducted in the Nevada Railroad Museum. One rail section with two pre-damaged internal defects (Figure 9) was selected for the tests. Two internal defects were prepared by replacing about 100 ft of track with pre-damaged defects for the field test. In this stage, the sensors were installed on the vehicle to collect the AE signals when the train ran over the defect locations. The rail track used in the field tests was an AREMA 130-lb rail, and the defects were internal defective welds characterized by the crack types and locations. As illustrated in Figure 10, the size of the first defect was 0.2 inches by 0.3 inches, located 0.7 inches below the rail surface, and the second defect was 0.2 inches by 0.2 inches, located 1 inch below the rail surface. An Olympus Epoch 1000i ultrasonic inspector was used to evaluate the defect information, which indicated that both defects were in the early stages of development based on size. The rail track was supported by wood sleepers and ballast. The rail gauge was 4 feet 8.5 inches, and the distance between the sleepers was about 19 inches.

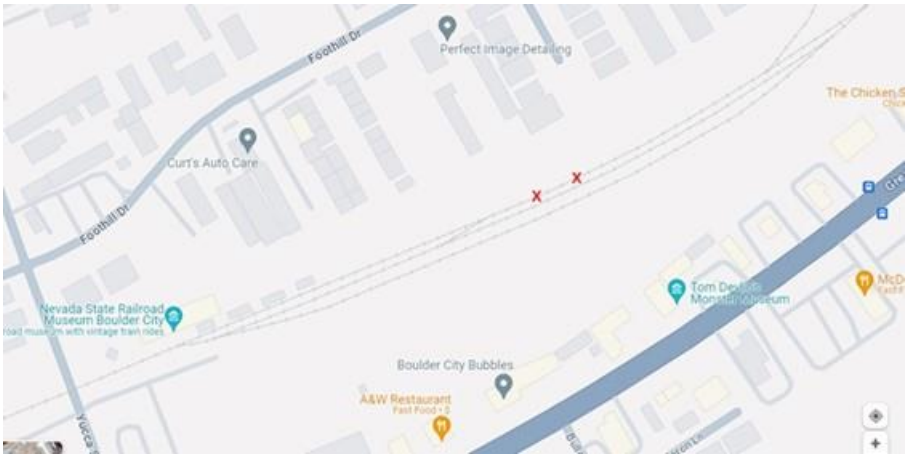

Figure 9 Internal defect location (red x-marked)

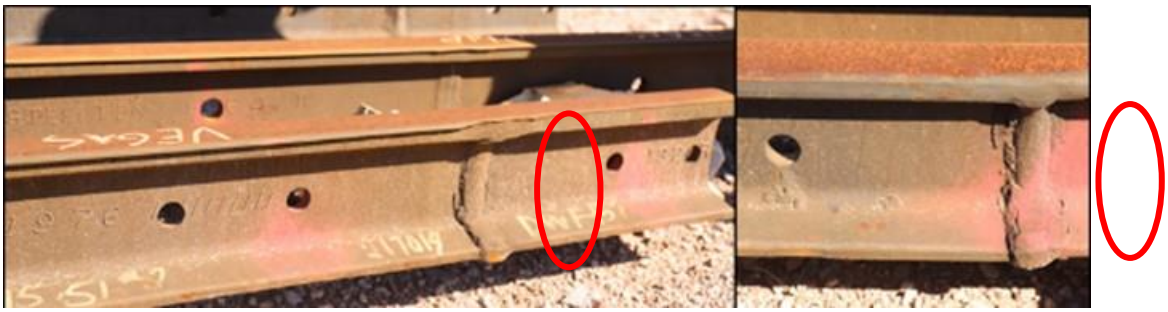

Figure 10 Two welding defects

Three identical sets of AE sensors were installed on a steel plate, which was mounted on the rail suspension frame (
Figure 11a). This location was selected as it is optimal for collecting AE signals generated by wheel-rail impacts. Ultrasonic coupling gel was applied to ensure high quality signal propagation between the sensors and steel plate. A GoPro camera was installed on the back of the steel plate to record the track geo-information. The DAQ equipment and laptop were placed on the platform above the bogie (
Figure 11b).

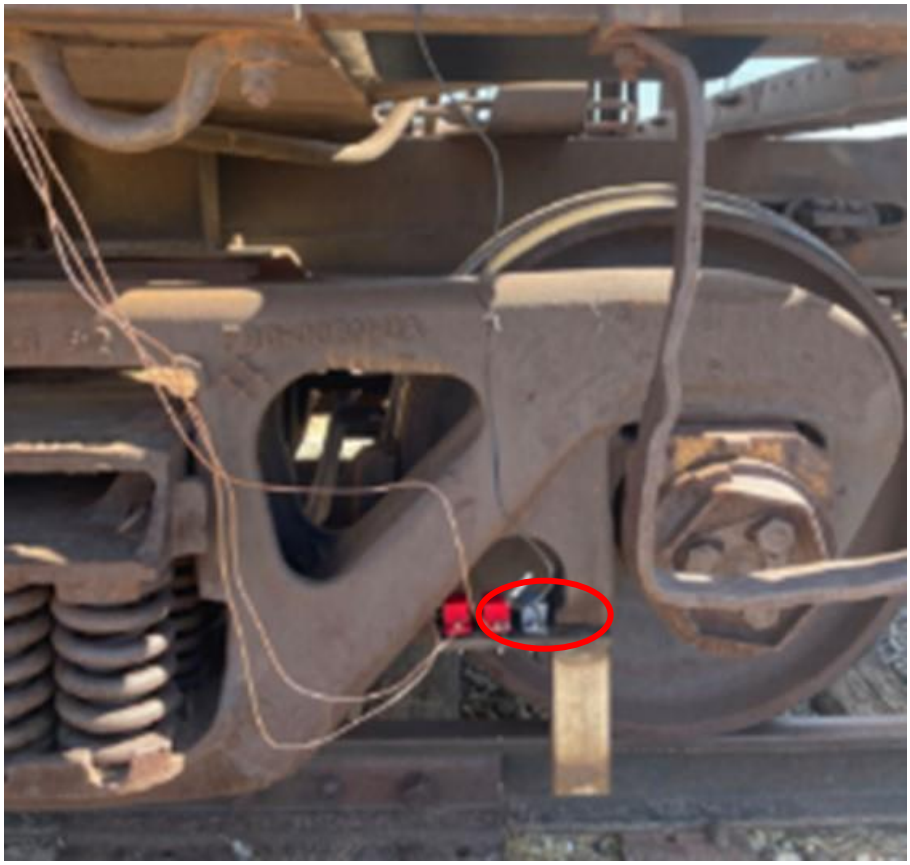

(a)

(b)

Figure 11 Prototype Installation

Acoustic signals were recorded when the hopper moved back and forth over the defect locations. To effectively synchronize the camera and DAQ equipment at the start of each test, a hammer strike was performed at the defect location. The hopper, which was empty and weighed approximately 30 tons, traveled at a speed of about 5 mph. The hopper provided a high axial load to increase the AE event possibilities and ensure the real-world testing environment was used to evaluate the proposed approach. The field tests were conducted in 4 sets with 5 runs per set (back and forth as one run) in order to ensure sufficient rail-wheel impacts to generate AE events. However, due to restricted access to the site, we were limited to conducting tests within specific scheduled time slots. Despite these constraints potentially impacting AE signal collection, this field study offered a valuable opportunity to assess the proposed approach in real-world conditions.

2.4 Time-Frequency Representation of AE Signals

For accurate characterization of AE signals, especially those signals change over time, it is essential to process and present signals effectively. Non-stationary signals, whose frequencies and amplitudes vary with time, pose a particular challenge for traditional methods like the Fourier transform. While the Fourier transform provides a global view of the frequency components, it can fail to capture localized variations in time. In contrast, time-frequency analysis, particularly wavelet techniques, offers significant advantages in this aspect (Zhang et al., 2015). Wavelet transforms, such as continuous wavelet transform (CWT) and discrete wavelet transform (DWT),

enable multi-resolution analysis of signals, effectively capturing both time and frequency information.

In this study, the CWT is utilized instead of DWT due to its ability to operate at narrower scales, offering enhanced multi-resolution capabilities and superior performance in noisy environments, particularly for detecting discontinuity. To minimize computational effort, the analysis is conducted on specific segments of AE waves. This section briefly overviews the CWT theory and the rationale behind the mother wavelet selection.

Based on the definition, CWT is the convolution of the signal $x(t)$ with a set of wavelet functions $\psi_{a,b}(t)$ which are created by dilating and translating a single mother wavelet $\psi(t)$ that meets certain criteria (Peng & Chu, 2004; Yan et al., 2014).

$$\boldsymbol{WT(a,b) = \int_{-\infty}^{\infty} x(t)\psi_{a,b}^{*}(t)\,dt} \tag{1}$$

where,

$$\psi_{a,b}(t) = \frac{1}{\sqrt{a}}\psi\left(\frac{t-b}{a}\right) \qquad (a, b \in R, and\ a > 0) \tag{2}$$

In the equation above, $\psi_{a,b}(t)$ represents the complex conjugate, *a* denotes the scale parameter, *b* indicates the translation parameter, *t* is the time, and $WT(a,b)$ is the wavelet coefficient associated with it. The wavelet function $\psi_{a,b}(t)$ is centered at *b* with a spread proportional to *a*, which is calculated as a window function in the time-frequency domains. During the transform, a series of $\psi_{a,b}(t)$ is produced based on multiple values of *a* and *b*. The selection of the mother wavelet greatly impacts the outcomes of CWT. Therefore, it is essential to determine an appropriate mother wavelet based on various aspects of wavelets (such as symmetry, orthogonality, and support size).

An appropriate mother wavelet is essential to the results of CWT analysis. Various components need to be considered before selecting the optimized mother wavelet. In this chapter, the complex Morlet wavelet was utilized due to its remarkable time-frequency domain resolution (A Teolis, 2017; Dehghan Niri & Salamone, 2012). The function and its corresponding Fourier transform are,

$$\psi(t) = \frac{1}{\sqrt{\pi f_b}}\exp\,(i2\pi f_c t)\exp\,(-\frac{t^2}{f_b}) \tag{3}$$

$$\hat{\psi}(f) = \exp\,\{-\pi^2 f_b (f - f_c)^2\} \tag{4}$$

Here, f_b denotes the non-dimensional bandwidth parameter, f_c denotes the wavelet central frequency in Hz, and *i* represents the imaginary unit. Additionally, f_b and f_c need to be selected based on the analyzed AE signals. Figure 12 presents an example of time-frequency frequency using CWT analysis.

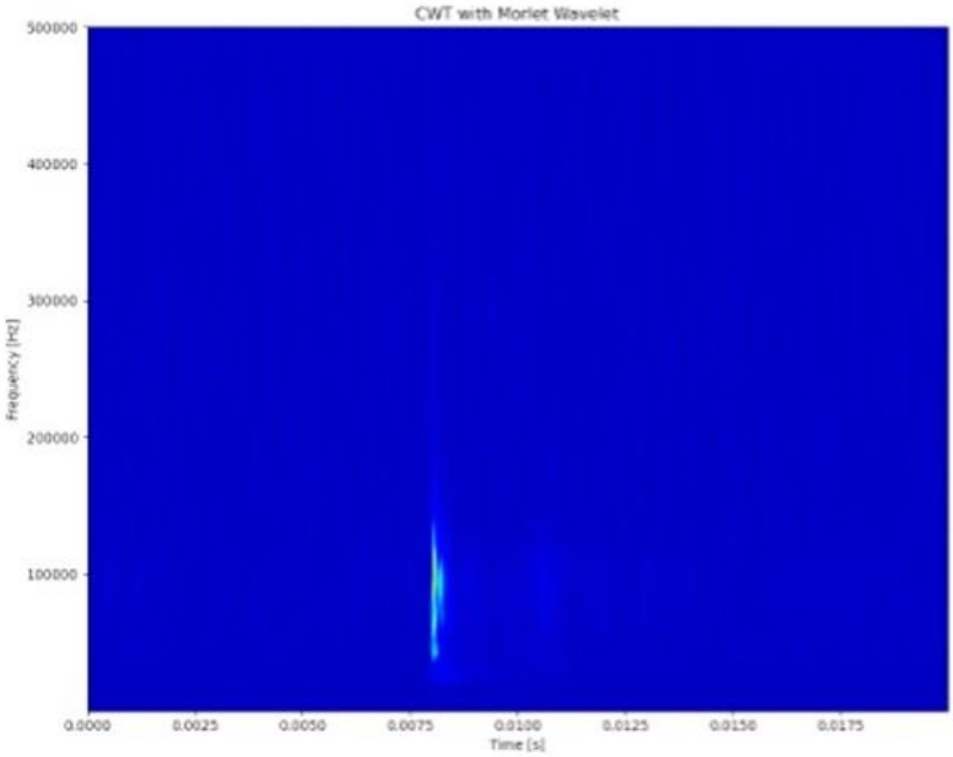

(a)

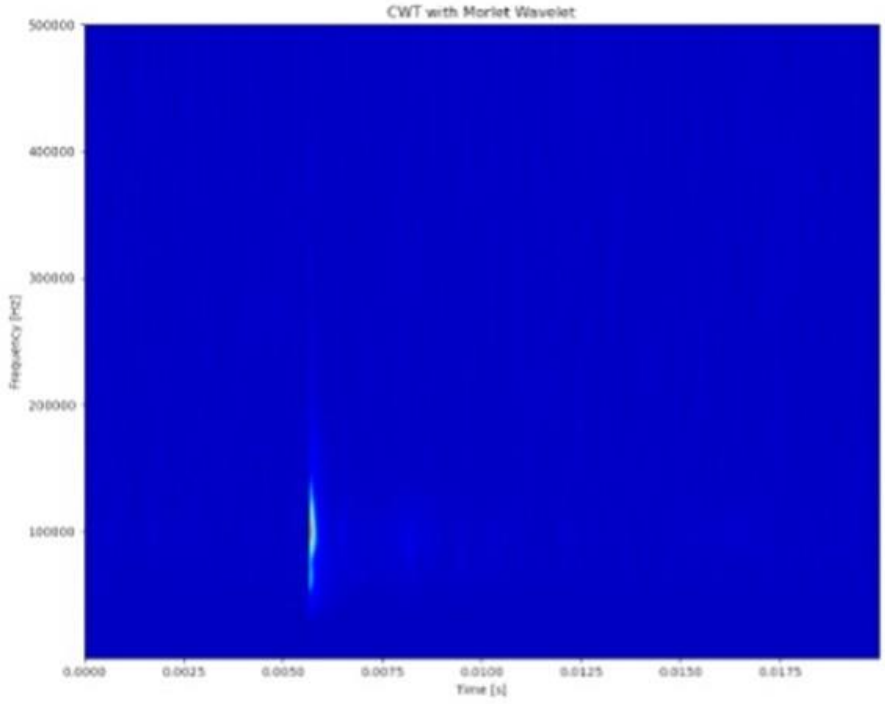

(b)

Figure 12 CWT of AE signal with (a) high amplitude and (b) low amplitude

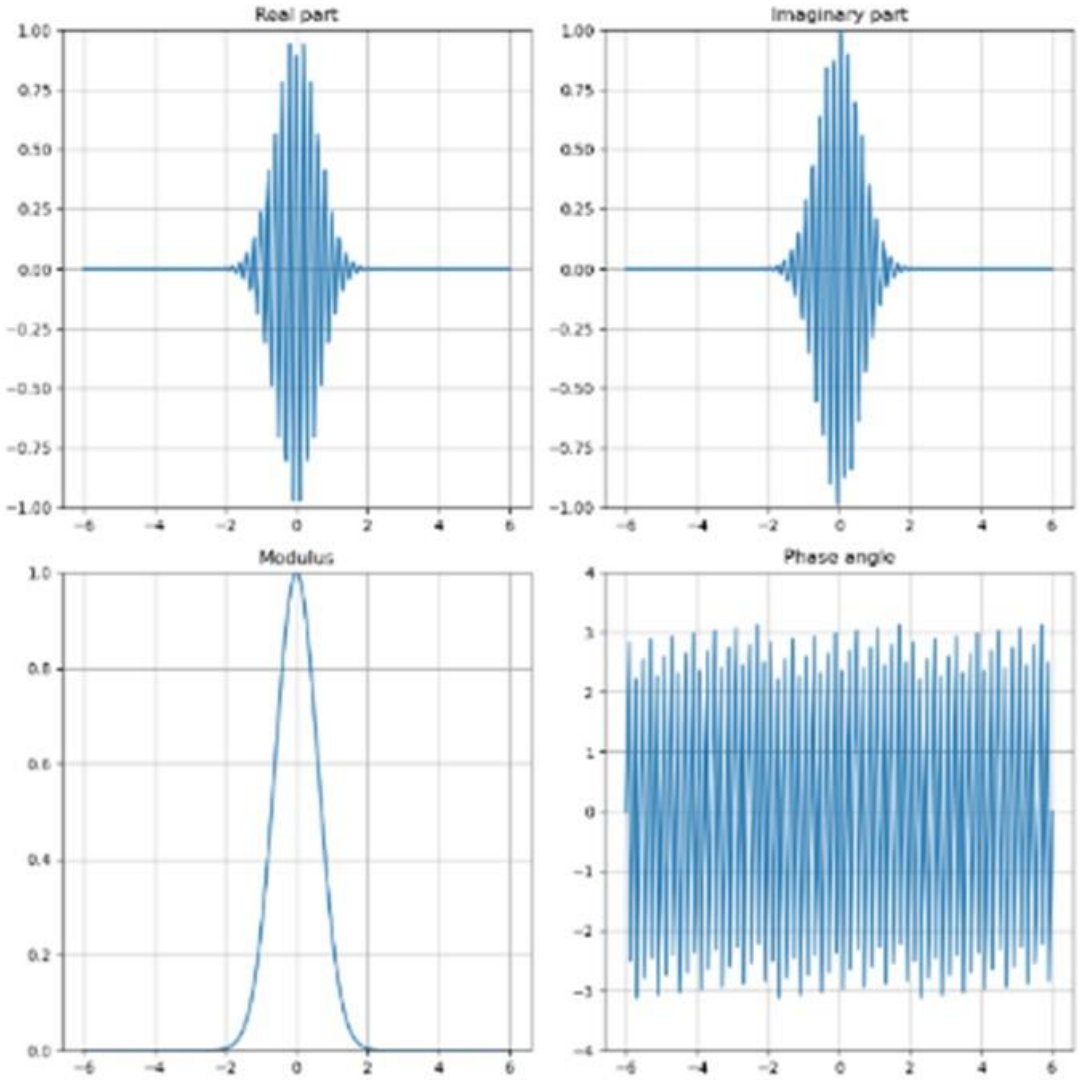

Figure 13 Example of Morlet mother wavelet ($f_b = 0.6, f_c = 5$)

Figure 13 presents an example of a Morlet wavelet. In general, the Morlet wavelet is suggested $f_c \geq \frac{5}{2\pi}$ due to the rapid attenuation in the envelope. Shannon entropy can be utilized to quantify the entropies in order to determine the proper parameters of the mother wavelet, such as f_b and f_c. It indicates the similarity between the basis function and the signal being analyzed. A lower wavelet entropy value signifies a greater similarity, making it a useful criterion for selecting the appropriate basis function for the wavelet transform. In this study, $f_b = 0.5$ and $f_c = 4$ were selected in this study to ensure the lowest wavelet entropy (Li, 2018).

2.5 Time-frequency Analysis Results

The time-frequency characteristics of AE signals collected in the field tests were processed using CWT. Additionally, such visible differences made identifying and canceling ambient noise possible in the future. Figure 14 shows the CWT of the AE events detected and verified locations

with the videos. Due to the early stage of the defect development for both defects, three AE events were detected during the entire test. Two events were collected from the first defect and one from the second defect.

To effectively present the AE features, a high-pass filter with 60 kHz was employed to reduce the effects of low-frequency noises. Figure 14 indicated that the wave energy was primarily concentrated in the 60-120 kHz and a notable amount of energy is in the 200-300 kHz range. In contrast, Figure 15 presented the CWT of two typical ambient noises, where the energy was mainly concentrated below 150 kHz. This is significantly different from the defect-induced AE signals. Therefore, filtering out the lower frequency components of the AE signal can significantly reduce the impact of noise. Additionally, such visible differences made identifying and canceling ambient noise possible in the future.

(a)

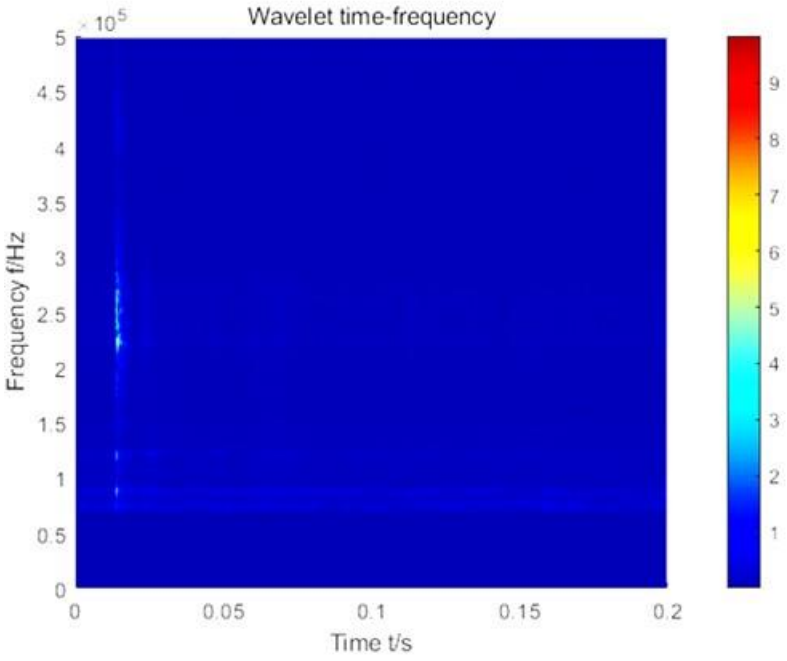

(b)

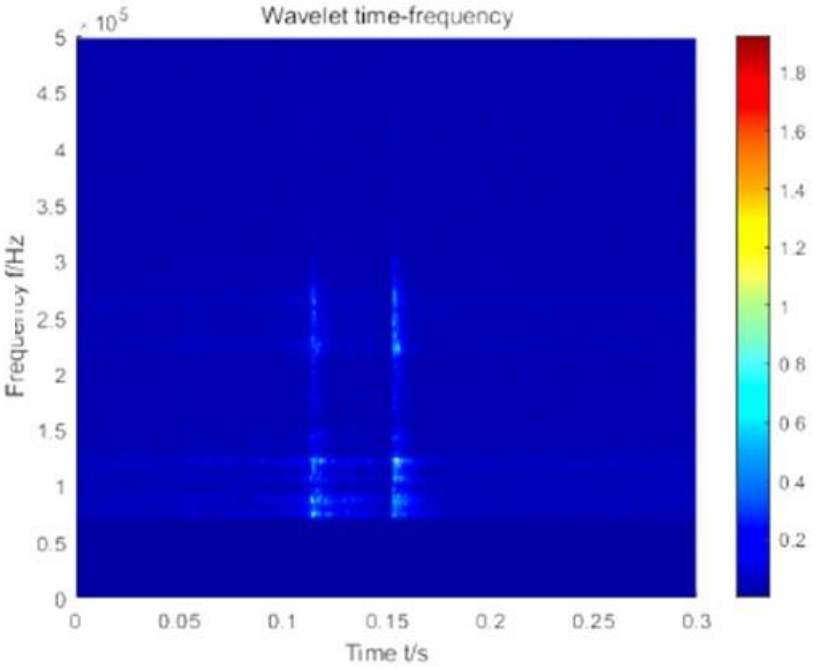

Figure 14 Defect-induced AE signals (a) single impulse (b) dual impulses

(a)

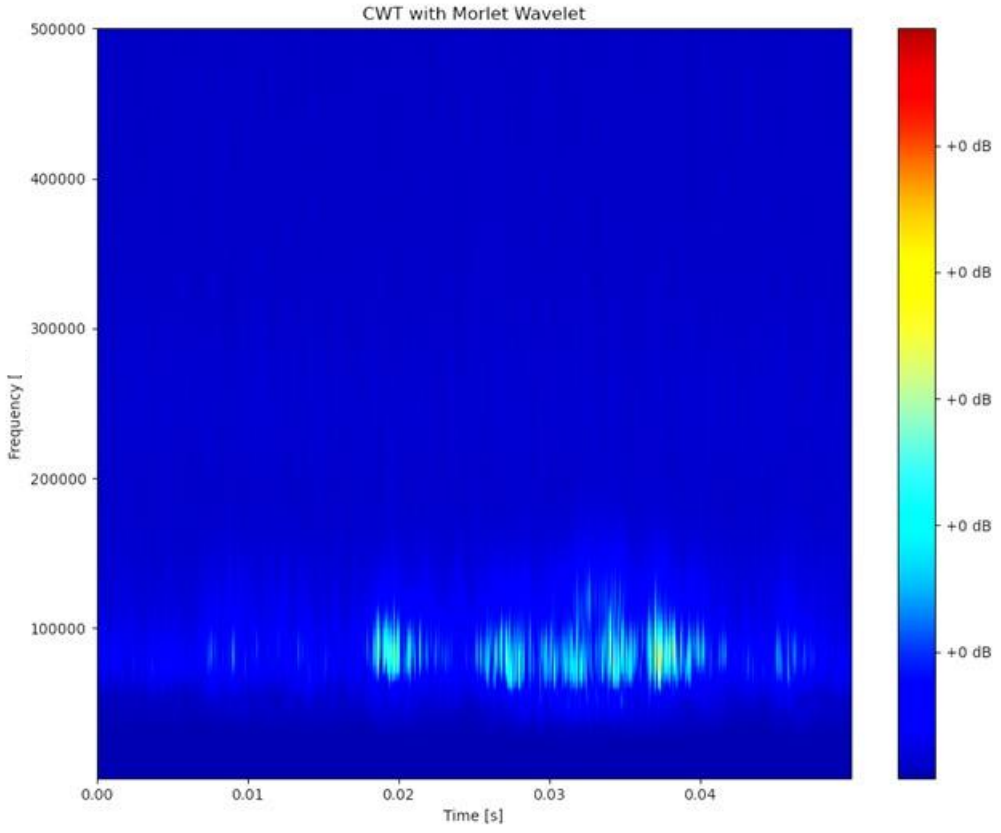

(b)

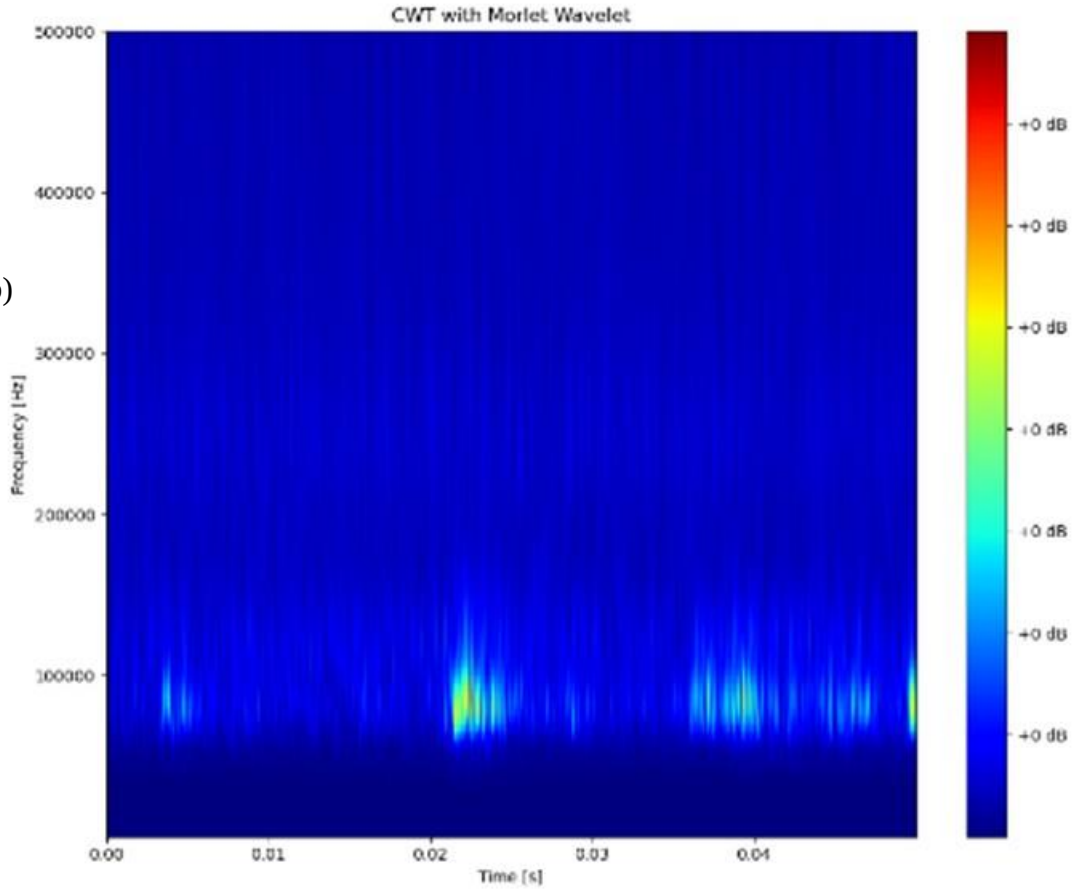

Figure 15 Ambient noise-induced signals (a) braking noise (b) mechanical vibration

The field test in the Nevada Railroad Museum provided a promising result that AE signals caused by rail defect development are able to be detected and recognized. Meanwhile, general ambient noises presented significantly different characteristics from the AE signals. Therefore, based on the preliminary results obtained, real-world field tests were conducted with the attempts to evaluate the AE characteristics of various defect types of development stages and investigate the AE detection performance under high noise environment at high speeds.

CHAPTER 3: FURTHER INVESTIGATION ON RAIL DEFECT DETECTION USING BONE-CONDUCT SENSORS

Preliminary studies conducted in Nevada have presented the potential of applying the AE inspection technique to identify rail defects in real-world conditions. The study in this chapter intended to explore AE characteristics through field tests conducted under various scenarios. In real-world scenarios, higher speeds are expected to produce increased ambient noises, wind vibrations, and stronger vibrations caused by impacts among various train and rail components. These factors can significantly affect AE signals, which are anticipated to be considerably more than the data collected in slow-speed field tests. To take an in-depth investigation into this, the chapter describes a series of field tests performed at Transportation Technology Center Inc. (TTCI) CO, designed to assess the performance of the proposed approach with the consideration of high speeds and intense vibrations.

3.1 Introduction

Following the test at the Nevada Railroad Museum, a series of field tests were designed and conducted at the TTCI, involving three different loops to vary factors, such as defect quantity and types, axial load, and testing speed. Collecting data from differently conditioned loops was critical to rigorously assess the system performance in defect detection.

The chosen loops were the Rail Defect Test Facility (RDTF), the High Tonnage Loop (HTL), and the Railroad Test Track (RTT). The RDTF (Figure 16) contains over 300 known artificial rail defects. It included a System Evaluation Zone, which spans 4,000 feet and contains over 250 defects with known locations, and a System Calibration Zone, which had approximately 30 defects distributed in dense clusters. Additionally, there was a Blind Zone, which contained various defects with unknown locations and characteristics, designed for verification purposes.
It is important to note that artificial defects like ones in the RDTF might not generate AE signals in the same way natural defects do due to inherent differences in how defects are generated. Analysis of defects whether it is natural or artificial should account for these potential differences in a careful examination.

Meanwhile, the tests were conducted using a high-rail vehicle (Figure 17) with an axial load significantly lower than that of real train cars. The low axial load used in testing does not fully replicate real-world scenarios, as commercial railcars typically have much higher weights. Consequently, additional field tests were necessary on the HTL to verify the system's performance under a broader range of load scenarios, ensuring a comprehensive evaluation. Consequently, additional field tests were necessary on the HTL (Figure 18). It is approximately 6.4 miles in length, includes over 30 naturally generated rail defects. The heavy-duty hoppers were utilized for these tests, with a speed limit of 40 mph. The final evaluation test was conducted on the RTT (Figure 18), which is 13.5 miles long with a speed limit of 105 mph. No defect information was provided for this loop; instead, the algorithms developed during the earlier tests were employed to identify defects on the RTT.

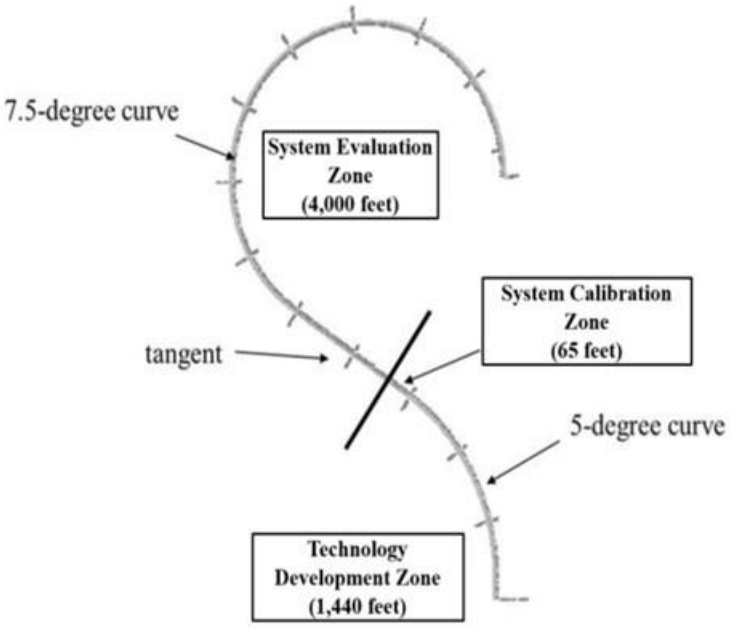

Figure 16 RDTF loop

Figure 17 Hi-Rail vehicle for RDTF

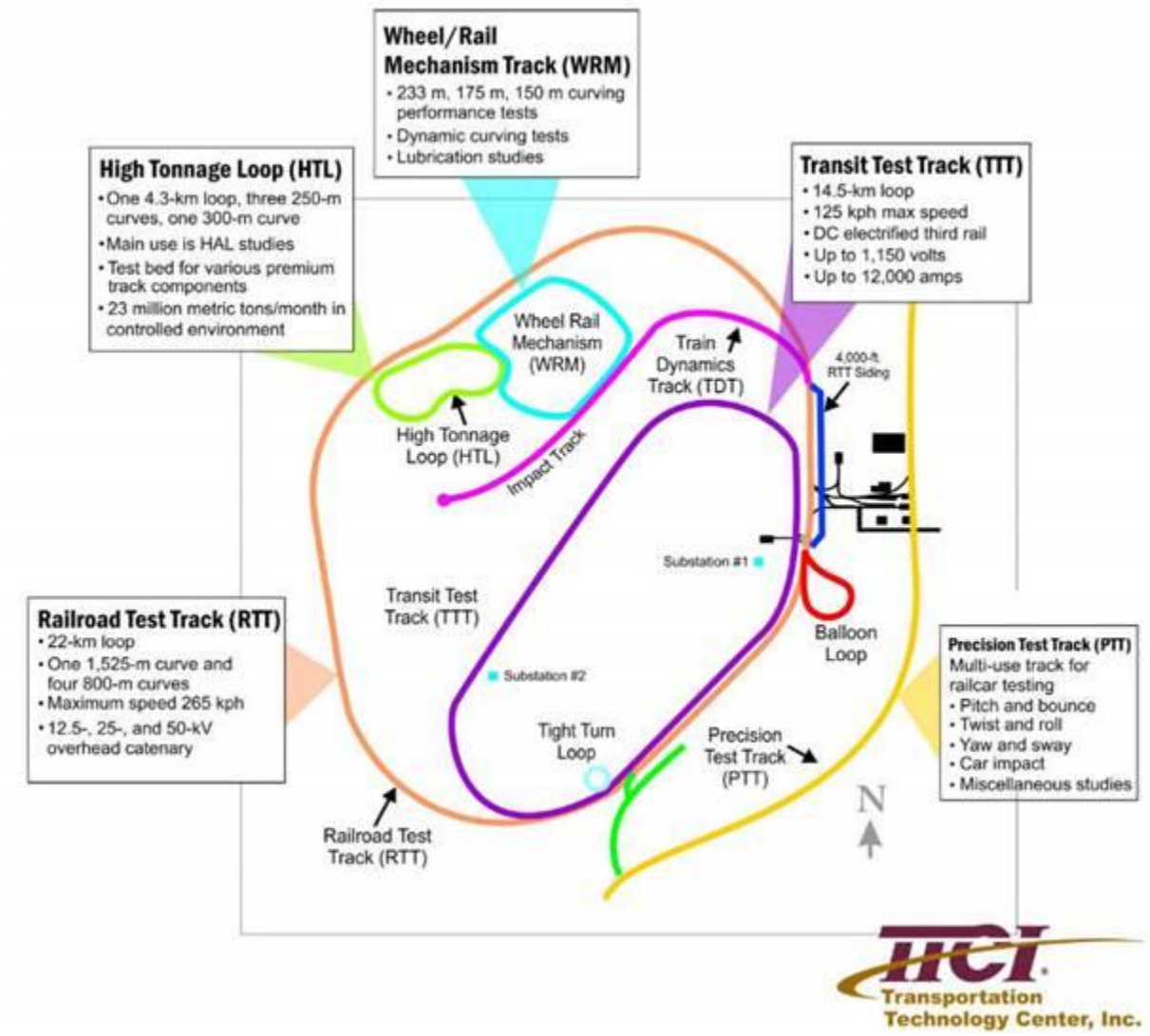

Figure 18 HTL and RTT loops

3.2 Field Tests

3.2.1 RDTF Loop

The purpose of field testing in this study is to collect AE events from various types of defects under different conditions, providing a dataset for further analysis using algorithms such as machine learning. Defects were artificially created by cutting or drilling the tracks, as shown in Figure 19. In this testing loop, three identical sets of AE sensors and two GoPro cameras were installed on a steel plate mounted on the bottom frame of the Hi-rail vehicle (Figure 20). The installation locations were carefully selected to ensure safety, and the detectability of AE signals generated by wheel-rail impacts. Ultrasonic coupling gel was applied to the sensor surfaces to ensure high-quality signal transmission between the sensors and the steel plates. The DAQ equipment and a laptop were housed inside the vehicle (

Figure 21).

Acoustic signals were collected as the Hi-rail vehicle traversed the defects. A hammer hit was used at the beginning of each test to synchronize the cameras with the DAQ equipment. The Hi-rail vehicle, weighing approximately 5 tons, had an axial load significantly lower than that of a commercial hopper. Field tests were conducted at four different speeds—5 mph, 10 mph, 15 mph, and 20 mph. The 20-mph setup included 10 runs (each run consisting of a back-and-forth motion), while the other setups had 5 runs each. This ensured sufficient rail-wheel impacts to generate AE events. The primary goal was to collect AE signals at various speeds, enabling a comprehensive evaluation of AE features based on different defect types and vehicle speeds.

Figure 19 Defects in RDTF loop

Figure 20 Configuration of sensors and cameras on Hi-Rail vehicle

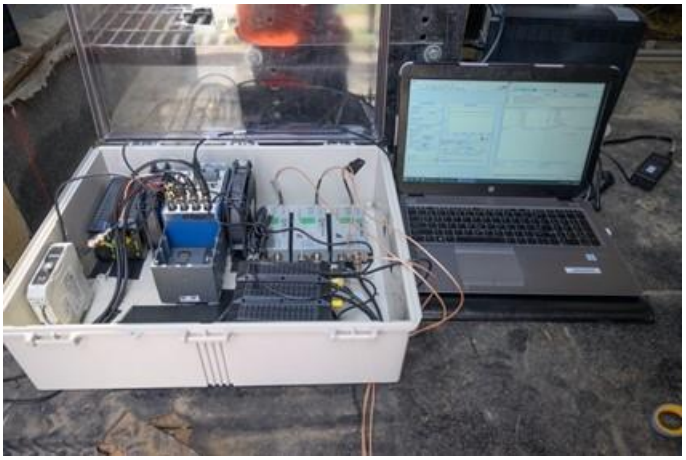

Figure 21 AE prototype and LabVIEW

3.2.2 HTL Loop

The HTL loop field tests are different as this loop involves naturally created rail defects. It had 39 defects over a loop span of 6.4 miles. As an example, a typical web crack defect is shown in Figure 22. For accurate assessment of rail defects, a preliminary inspection was conducted on all defects, one at a time to identify the size, type, and location of each defect. The results were documented by TTCI. Eight defects were located on the bypass track (red circled) and thus were excluded from this field testing. Therefore, 31 defects distributed on the main loop were used for data collection and further analysis (Figure 23). The vehicle used in this field test was a 30 tons empty hopper (Figure 24). The sensors and cameras were installed in the same configuration as in the RDTF tests (Figure 25), and the DAQ equipment was securely placed on top of the bogie.

Three tests were conducted at 20 mph, and ten tests were conducted at 40 mph, the maximum speed allowed on the HTL loop. The 20-mph tests were designed to collect AE signals with relatively low ambient noise, serving as a baseline or "ground truth" for comparison with the 40-mph tests. The AE signals collected during this phase will be compared with those obtained from the previous tests involving artificially induced defects, highlighting differences between natural and artificial defects. Additionally, AE signals and ambient noises from both field test sets will be extracted and used to train machine learning (ML) models to distinguish defects from ambient noise and classify different defect types.

Figure 22 Rail crack in the web

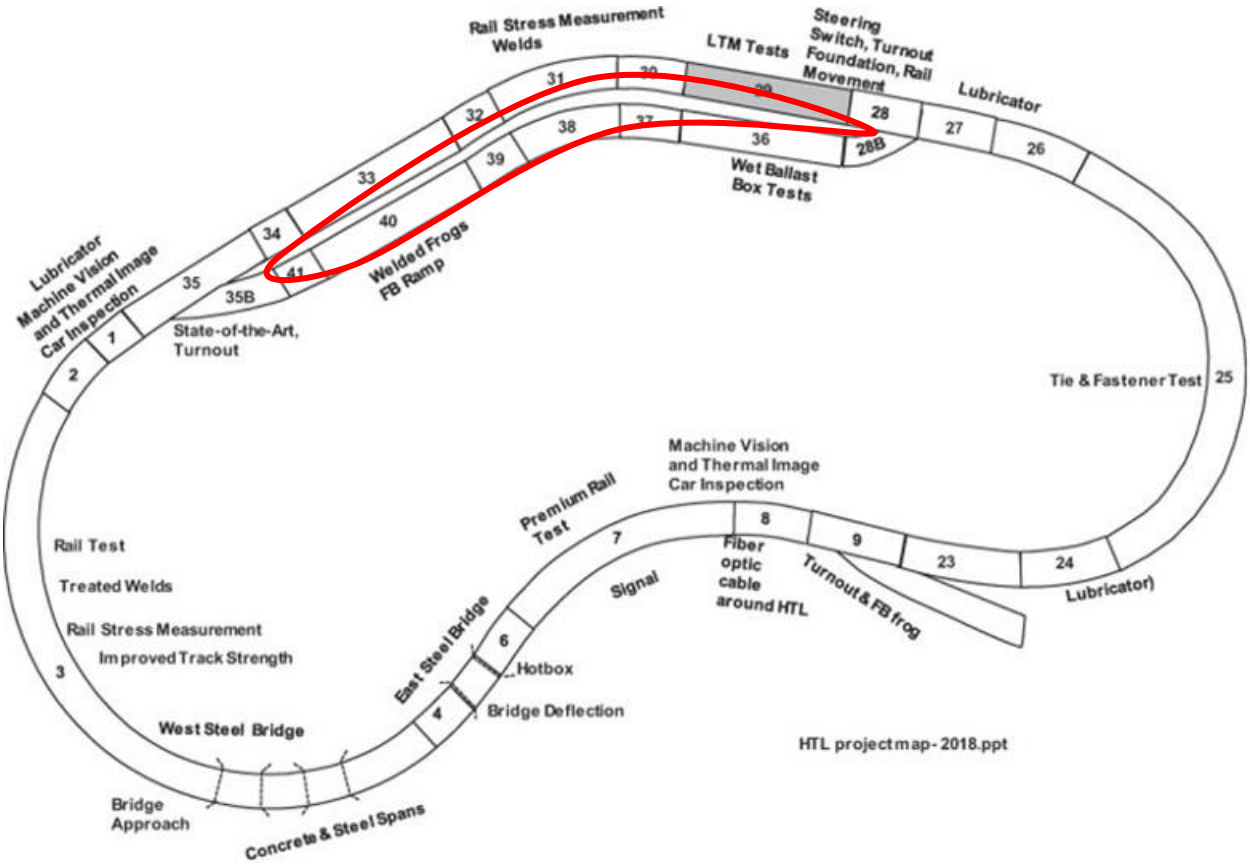

Figure 23 HTL loop

Figure 24 Testing vehicle with 30-ton empty axial load on HTL loop

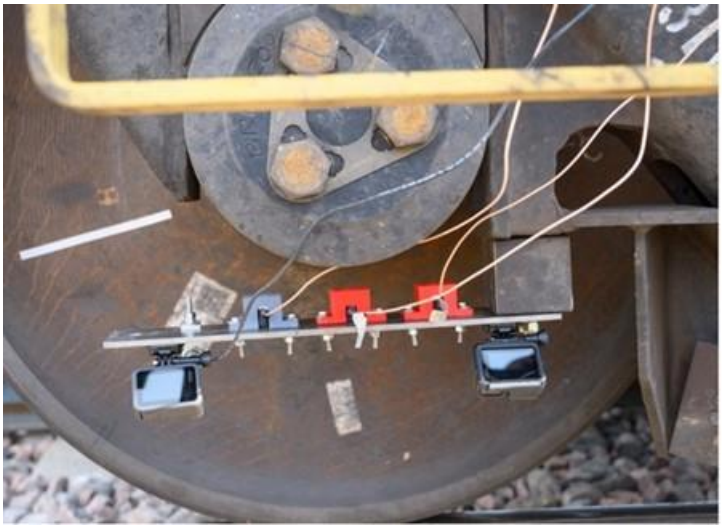

Figure 25 Mounting frame for sensors and cameras

3.2.3 RTT loop

After completing the tests in the RDTF and HTL loops, AE signals were collected with detailed information and precise defect locations, providing a foundational dataset for model training. Unlike the RDTF and HTL, the RTT loop was designed to include defects without their identified information. That is, their locations and sizes are unknown to the research team. This sequence of tests—RDTF, HTL, and RTT—was intentionally structured to allow the research team to utilize advanced machine learning techniques for studying rail defects. The data from RDTF and HTL serves as the training data while the data from RTT is used to make predictions of defects captured during high-speed rail operation. These field tests collectively designed with three real-world loops offer a unique testing environment to validate the system's predictive capabilities under real-

world scenarios. This approach ensures that the machine learning models are both trained on reliable data and validated in scenarios that closely mimic operational challenges. These field tests collectively designed with three real-world loops offer a unique testing environment to validate the system's predictive capabilities under real-world scenarios.

The entire length of the RTT loop was 13.5 miles, with a maximum allowable speed of 165 mph (Figure 26). The testing system was installed similarly as installed in the Nevada field test, as presented in Figure 27. However, due to safety concerns regarding the sensors and cameras, the maximum speed during this test was limited to 105 mph. Five tests were conducted: two at 40 mph and three at 105 mph. The purpose of the 40 mph tests was to evaluate and compare the effects of ambient noise with those observed during the HTL tests.

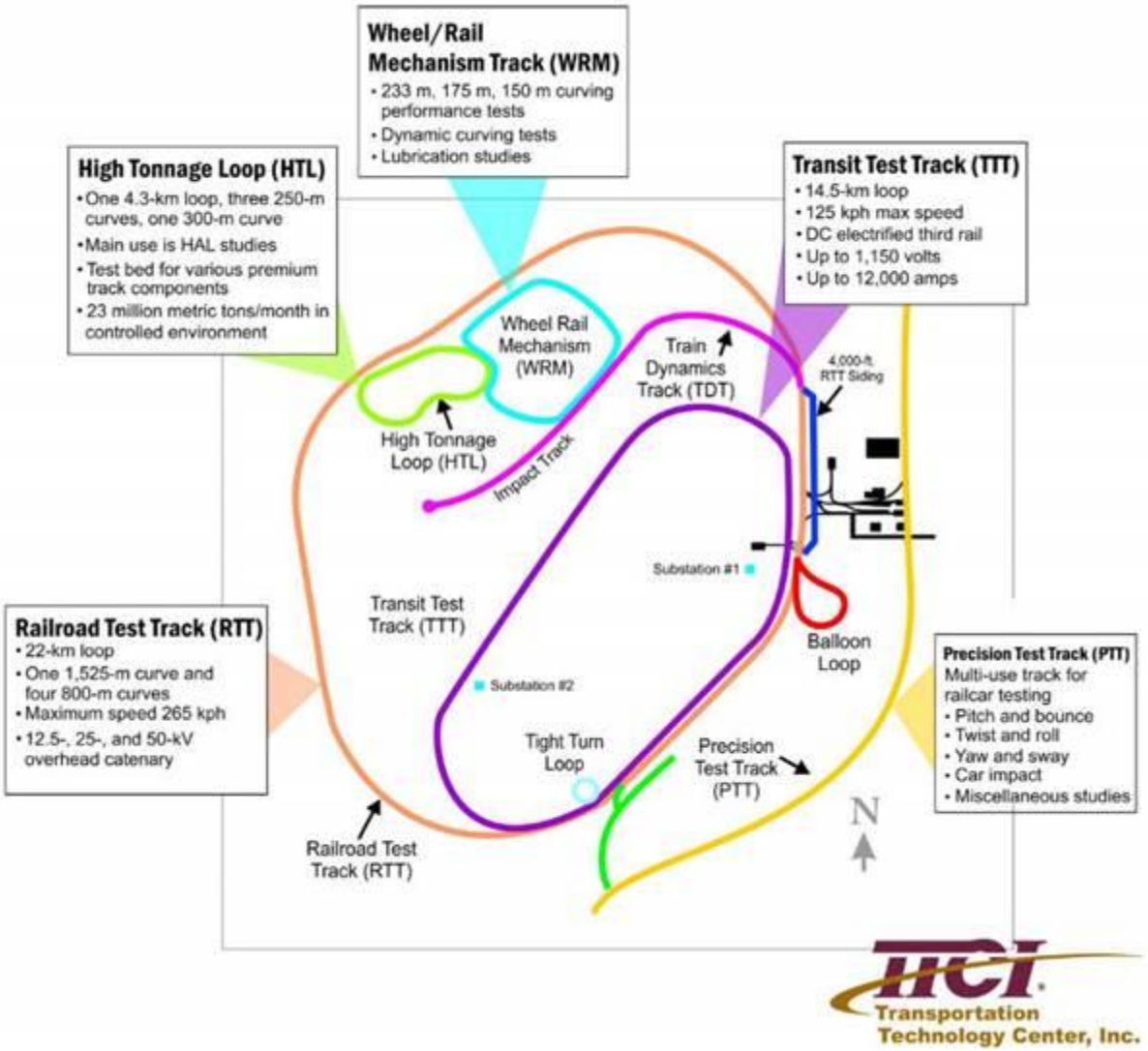

Figure 26 RTT loop (orange line)

Figure 27 Sensor location and testing car

In summary, the field tests conducted in TTCI aimed to collect AE events from various testing loops under different conditions, providing valuable datasets for machine learning analysis. Summarized tests were listed in Table 1. These tests were systematically conducted, with multiple runs at each speed, to ensure robust data collection for subsequent analysis and model training.

Table 1 Summary of Field Tests in TTCI

Test Location	Length (miles)	Defect Amount	Test Speed (MPH)	Number of Runs	Goal
RDTF	1.04	≥ 280	5	5	Evaluate AE features at various speeds
			10	5	
			15	5	
			20	10	
HTL	6.4	39	20	3	Explore and ML models
			40	10	
RTT	13.5	Unknown	40	2	Evaluate ML model at high speed
			105	3	

3.3 AE Characteristics and Classification Using Machine Learning

3.3.1 Time-Frequency Analysis of RDTF Loop

The CWT was employed to evaluate the time-frequency characteristics of the AE signals collected during the field tests. A 20 kHz high-pass filter was applied in this test to mitigate the impact of low-frequency noise. Preliminary CWT analysis was conducted using a 0.05-second time window, a duration chosen to balance signal resolution with data processing efficiency. Afterward, the GoPro video records were cross-referenced with the CWT data to identify potential AE events for further analysis. These AE events, summarized in Table 2, were selected based on the following AE characteristics: notable impulses detected and frequencies typically ranging from 20 to 500 kHz. As shown in the table below, with the testing speed increased, the AE events detected also increased accordingly, which indicated that higher speeds would increase more. The defect developments were due to higher dynamic loads, which resulted in AE events. Additionally, these signals were confirmed with video records that wheel-rail impacts generated them.

Table 2 Summary of AE Events in RDTF loop

Test Location	Test Speed (MPH)	AE Events Amount	Total
RDTF	5	12, 10, 11, 17, 9	59
	10	14, 10, 11, 15, 17	67
	15	23, 15, 19, 11, 15	83
	20	22, 25, 16, 20, 22	204
		17, 24, 18, 21, 19	

Based on these findings, it is essential to analyze the data collected from the HTL loop and compare the characteristics of artificial defects with those of natural defects. Additionally, the comparison should extend to the rate of AE events occurring with the commercial hopper.

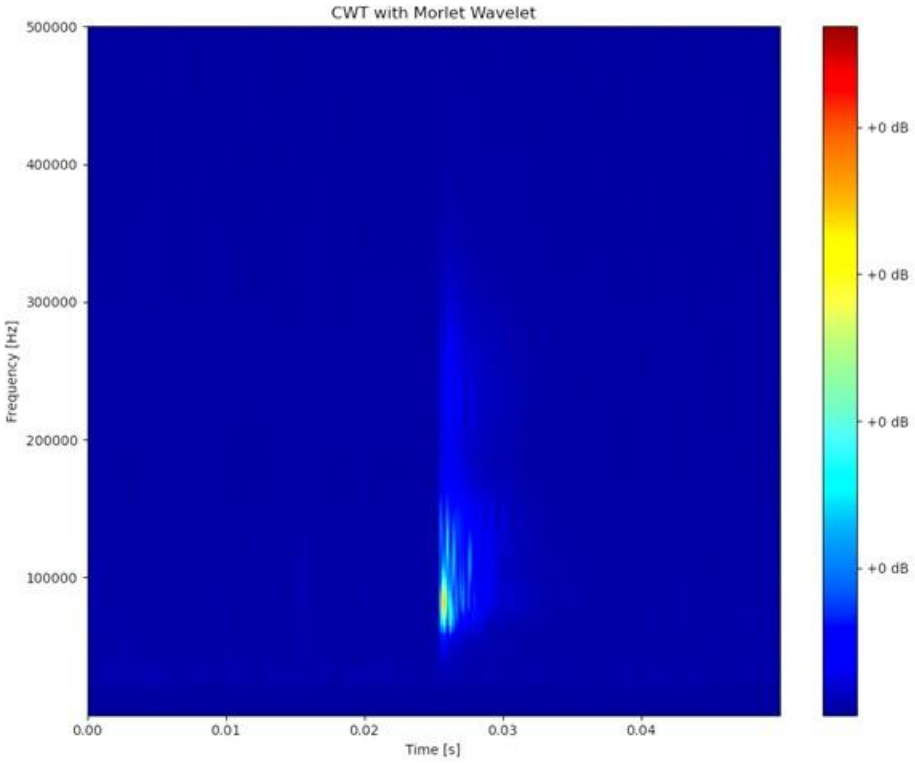

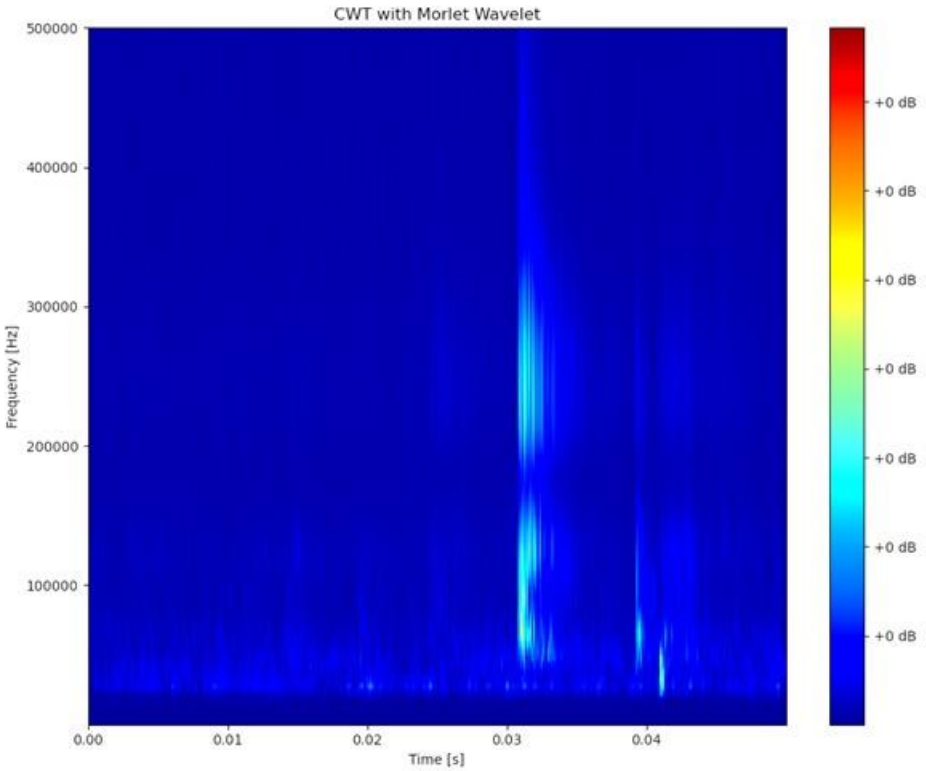
CWT with Morlet Wavelet
500000
400000
300000
200000
100000
Frequency [Hz]
0.00
0.01
0.02
0.03
0.04
Time [s]
+0 dB
+0 dB
+0 dB
+0 dB
+0 dB
+0 dB

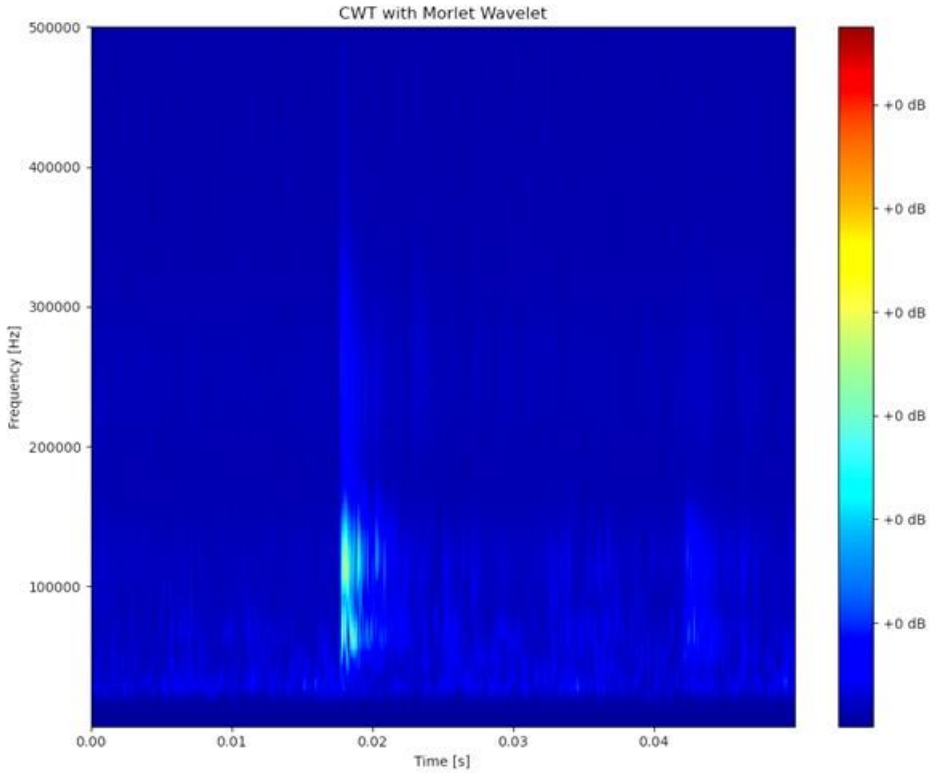
CWT with Morlet Wavelet
500000
400000
300000
200000
100000
Frequency [Hz]
0.00
0.01
0.02
0.03
0.04
Time [s]
+0 dB
+0 dB
+0 dB
+0 dB
+0 dB
+0 dB

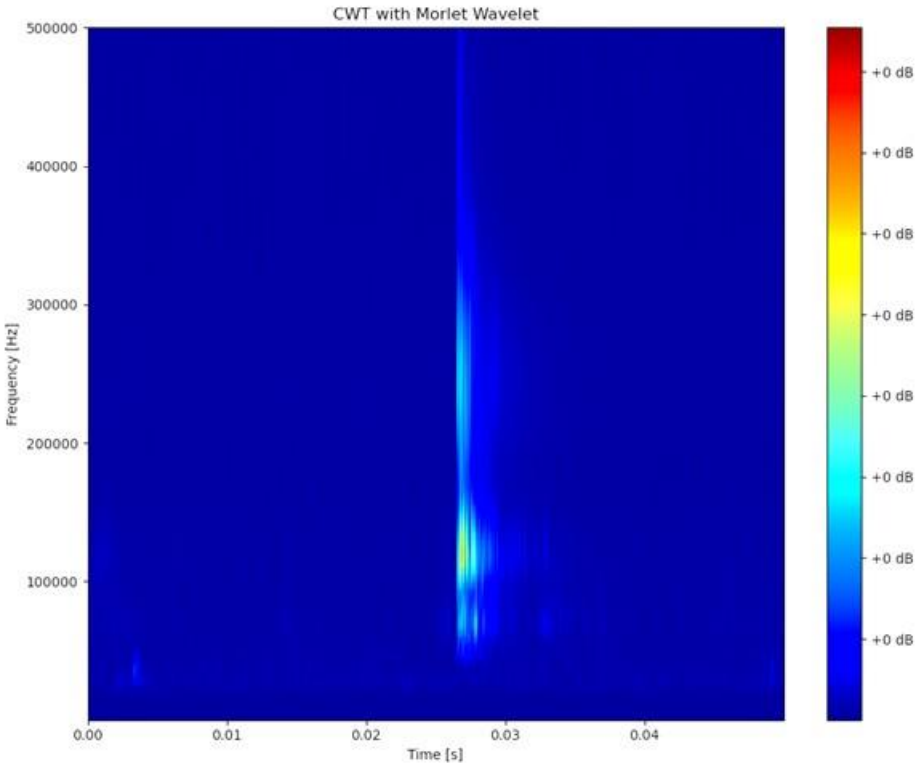

Figure 28 presents the CWT of typical impulse signals from different testing speeds involving complicated frequency distributions. While these signals generally lasted very short, the frequency range was typically distributed from 60 to 500 kHz. Meanwhile, the wave energy was primarily concentrated in the 60-150 kHz range, and a notable amount of energy was observed in the 200-300 kHz range. Similar to the conclusions of the first stage field test in Nevada, such features were observed in all the testing speeds.

In contrast, Figure 29 presents the time-frequency plots of ambient noise across four testing speeds, where the energy was primarily concentrated below 150 kHz—a clear distinction from the defect-induced AE signals. Compared to the impulse signals, it is evident that ambient noises are relatively low-frequency, continuous, and randomized. This observation aligns with findings from the initial stage of the field test in Nevada. Consequently, further analysis was conducted with a narrower time scale to examine the time-frequency characteristics in greater detail, as shown in Figure 30. This figure represents a typical AE pattern for events collected during the test. Notably, the signal did not exhibit significant attenuation during the impulse period. However, given the defect density within this loop, the number of detected events was relatively low. Two factors may have contributed to this: firstly, the testing vehicle was a hi-rail vehicle modified from a pickup truck, resulting in a significantly lower axial load than a commercial hopper. Secondly, all defects in the loop were artificially induced through cutting or drilling, which may have stabilized these defects, preventing further development under low compression conditions.

Based on these findings, it is essential to analyze the data collected from the HTL loop and compare the characteristics of artificial defects with those of natural defects. Additionally, the comparison should extend to the rate of AE events occurring with the commercial hopper.

(a)

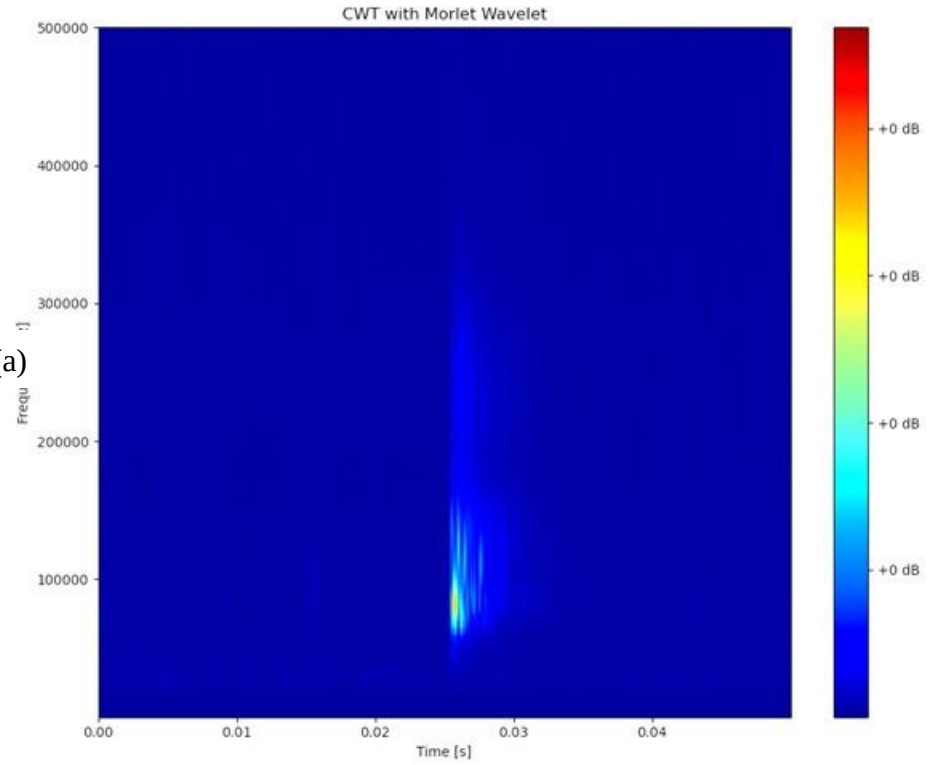
CWT with Morlet Wavelet
500000
400000
300000
200000
100000
Frequ
0.00
0.01
0.02
0.03
0.04
Time [s]
+0 dB
+0 dB
+0 dB
+0 dB

(b)

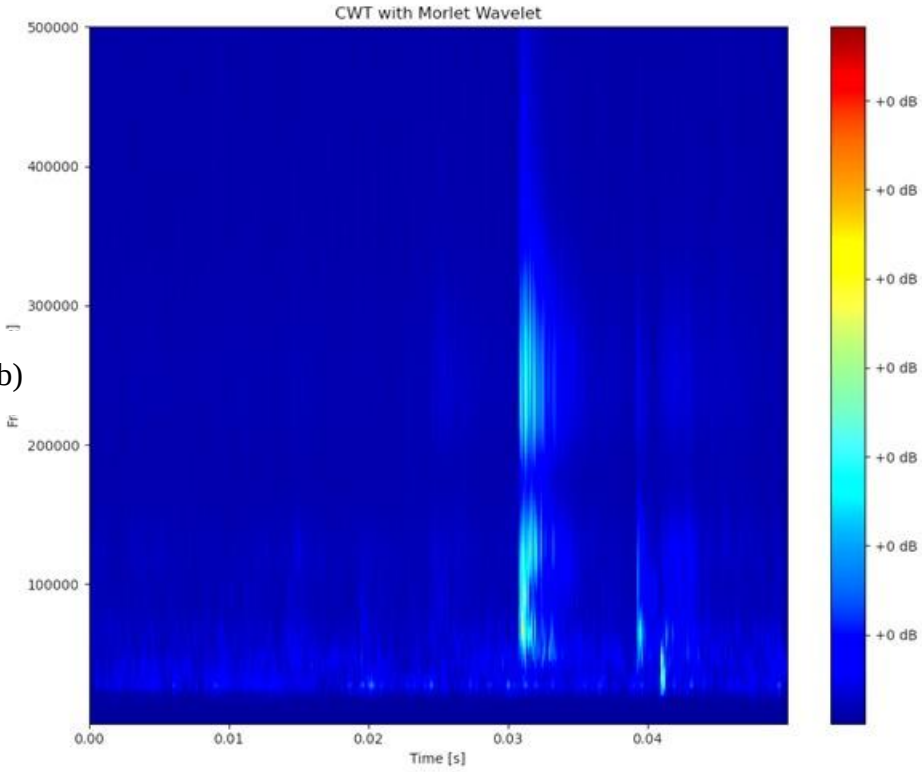
CWT with Morlet Wavelet
500000
400000
300000
200000
100000
Fr
0.00
0.01
0.02
0.03
0.04
Time [s]
+0 dB
+0 dB
+0 dB
+0 dB
+0 dB
+0 dB

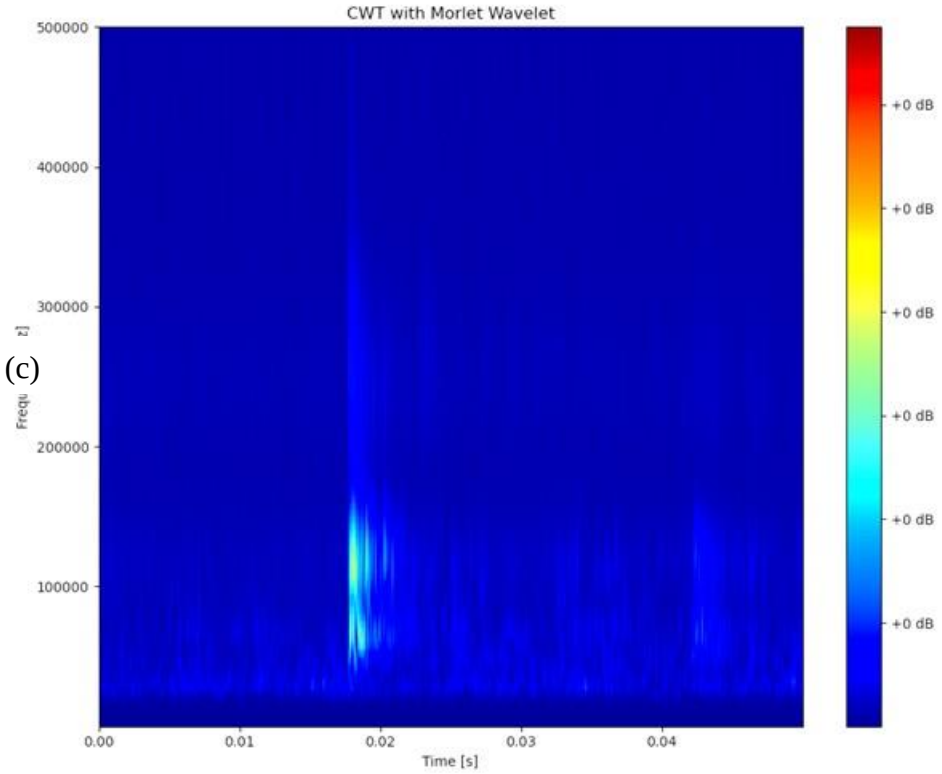

(c)

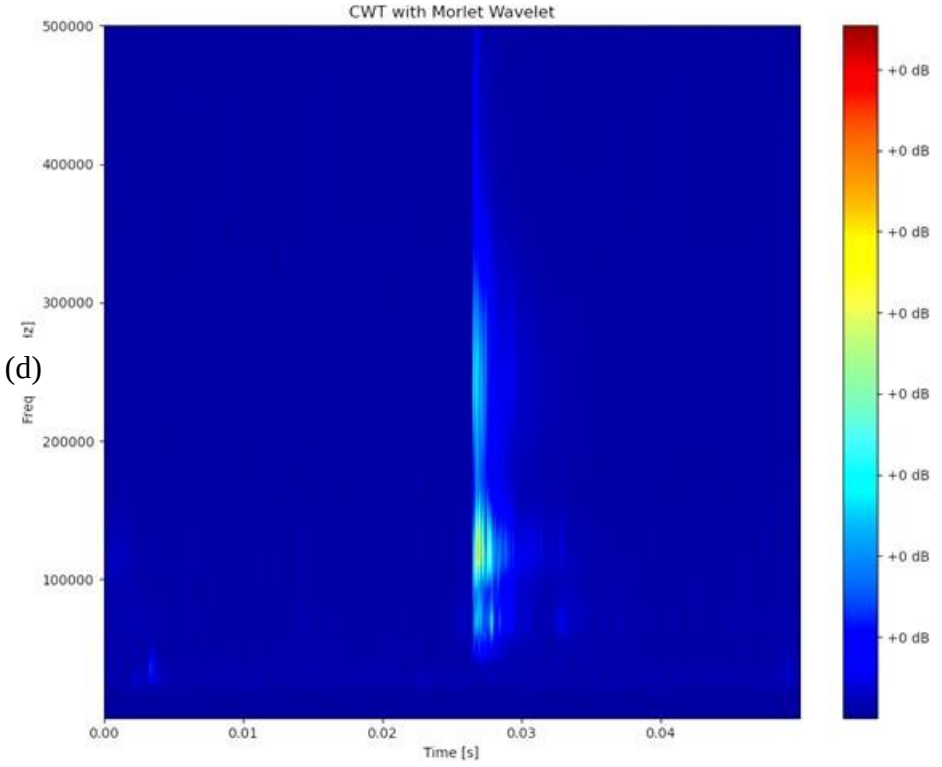

(d)

Figure 28 AE signals in RDTF tests (a) 5 mph (b) 10 mph (c) 15 mph (d) 20 mph

(a)

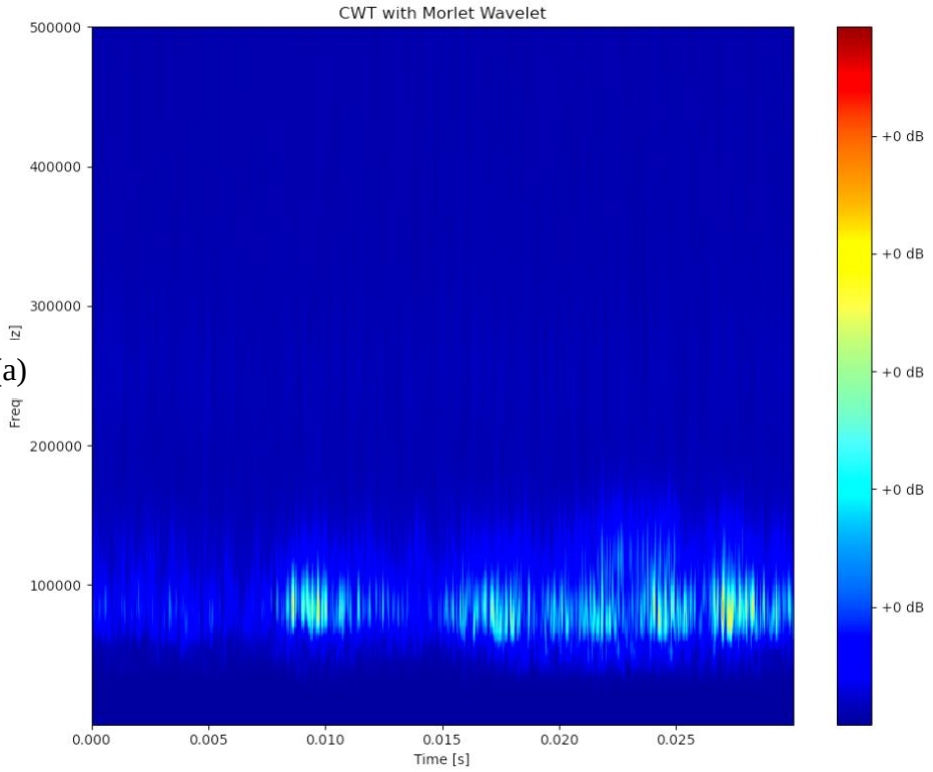
CWT with Morlet Wavelet
500000
400000
300000
200000
100000
Freq [Hz]
0.000
0.005
0.010
0.015
0.020
0.025
Time [s]
+0 dB
+0 dB
+0 dB
+0 dB
+0 dB

(b)

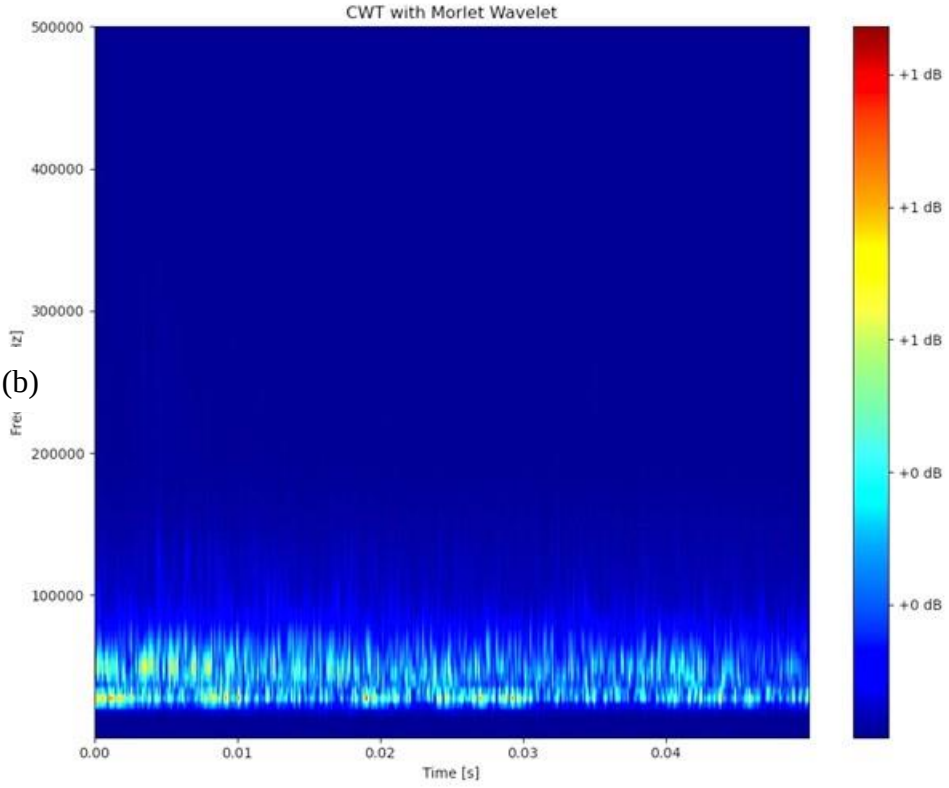
CWT with Morlet Wavelet
500000
400000
300000
200000
100000
Freq [Hz]
0.00
0.01
0.02
0.03
0.04
Time [s]
+1 dB
+1 dB
+1 dB
+0 dB
+0 dB

(c)

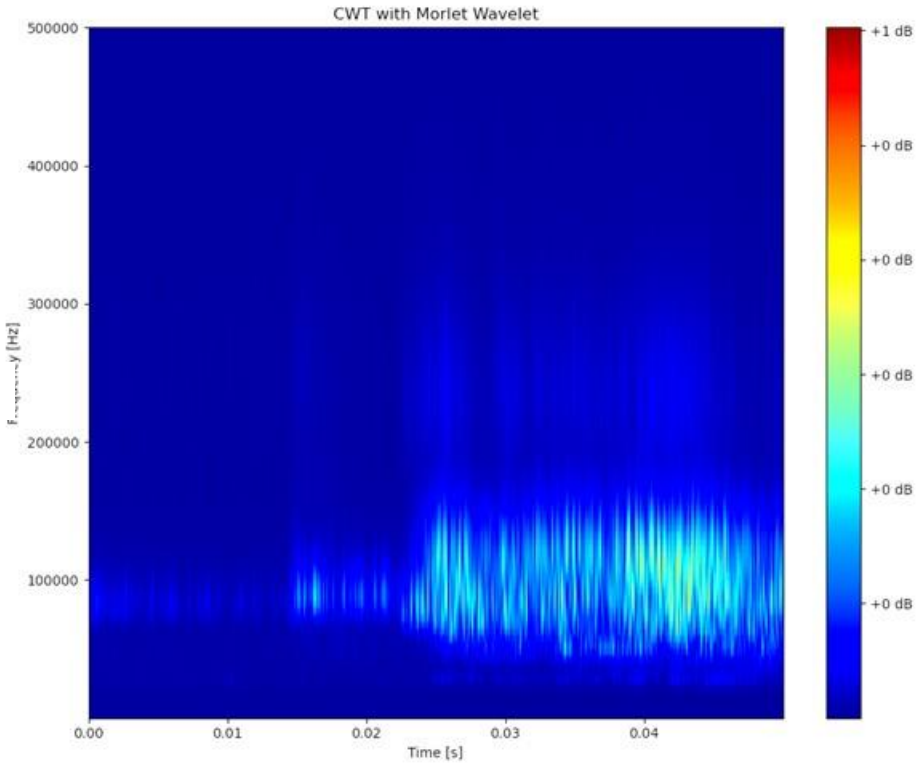

(d)

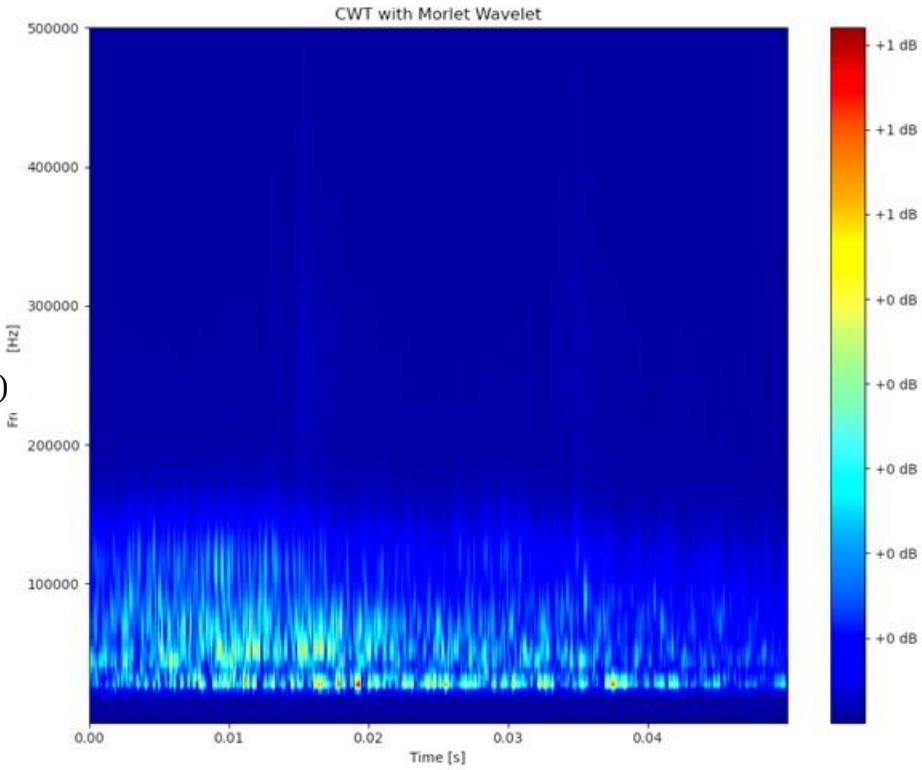

Figure 29 Ambient noise signals in RDTF tests

(a)

(b)

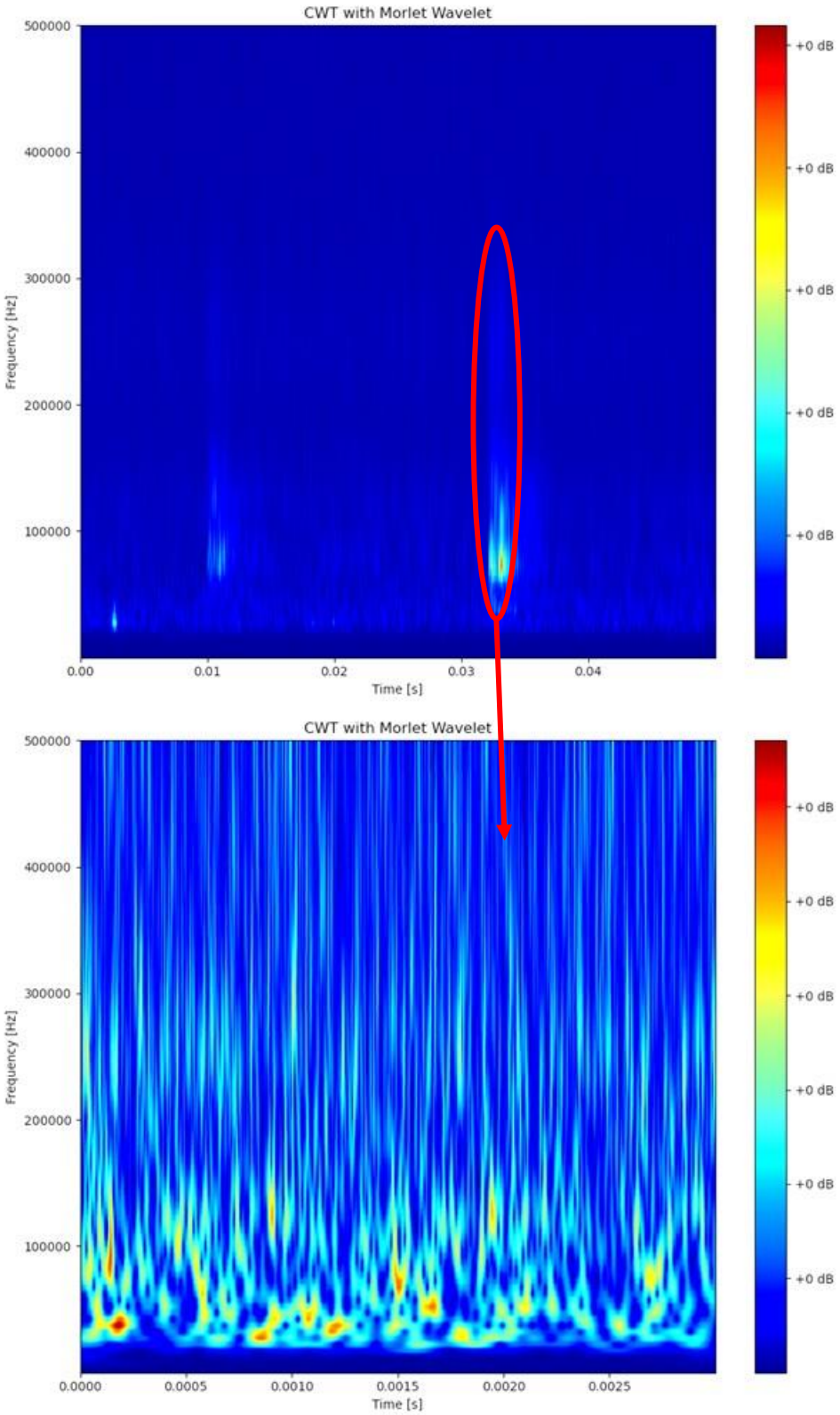

Figure 30 CWT of impulse signals (a) overview (b) narrower time window

3.3.2 Time-Frequency Analysis of HTL Loop

Following the preliminary data processing conducted at the RDTF, a time-frequency analysis was performed to evaluate the AE characteristics of naturally generated defects on HTL. The CWT was employed for the HTL field test data, incorporating a 20 kHz high-pass filter to mitigate the influence of low-frequency noise. The CWT analysis was preliminarily cross validated using the same methods applied to the RDTF data. Specifically, the time window for CWT analysis was set to 0.05 seconds, and GoPro video recordings were validated with the CWT data to identify potential AE events. A total of 31 defects were analyzed from the tests on the HTL Loop.

Unfortunately, the CWT features observed from different defects showed significant variations in certain defect area plots. Some plots clearly identified AE characteristics, as shown in Figure 31, where a distinct AE impulse is visible with a major energy distribution between 20-90 kHz along with a notable high frequency range from 120 kHz to 500 kHz. However, other plots presented more complex patterns. In many defect areas, multiple AE-like impulses were observed throughout the defect regions (Figure 32). These impulses also appeared in non-defect areas, complicating the identification of AE signals. When the analysis was conducted on a narrower time scale, the signals exhibited continuous features, making it challenging to distinguish AE characteristics.

In response to this challenge, this project used machine-learning techniques to study the complexity of identifying AE features in these intricate scenarios. Such advanced analytical tools could enable the automated extraction and classification of AE signals from extensive datasets. The machine-learning models were trained using the data from the HTL field tests, attempting to learn the characteristics of AE signals associated with different defect types and conditions. The application of machine learning in this context represents a significant advancement in the analysis of AE signals contributing to more efficient and reliable rail defect detection methods in future studies.

(a)

(b)

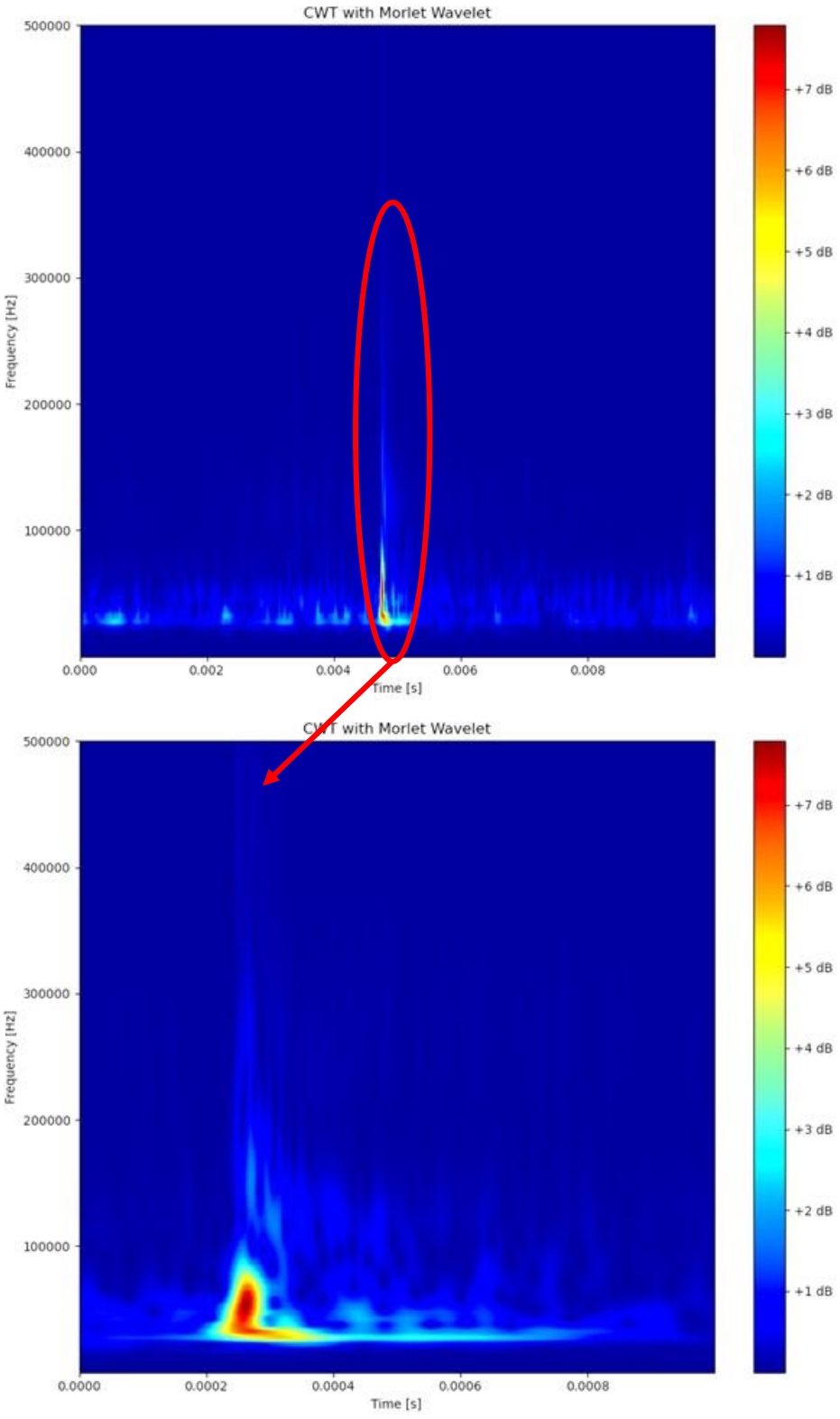

Figure 31 Visible AE signal detected in HTL loop

(a)

(b)

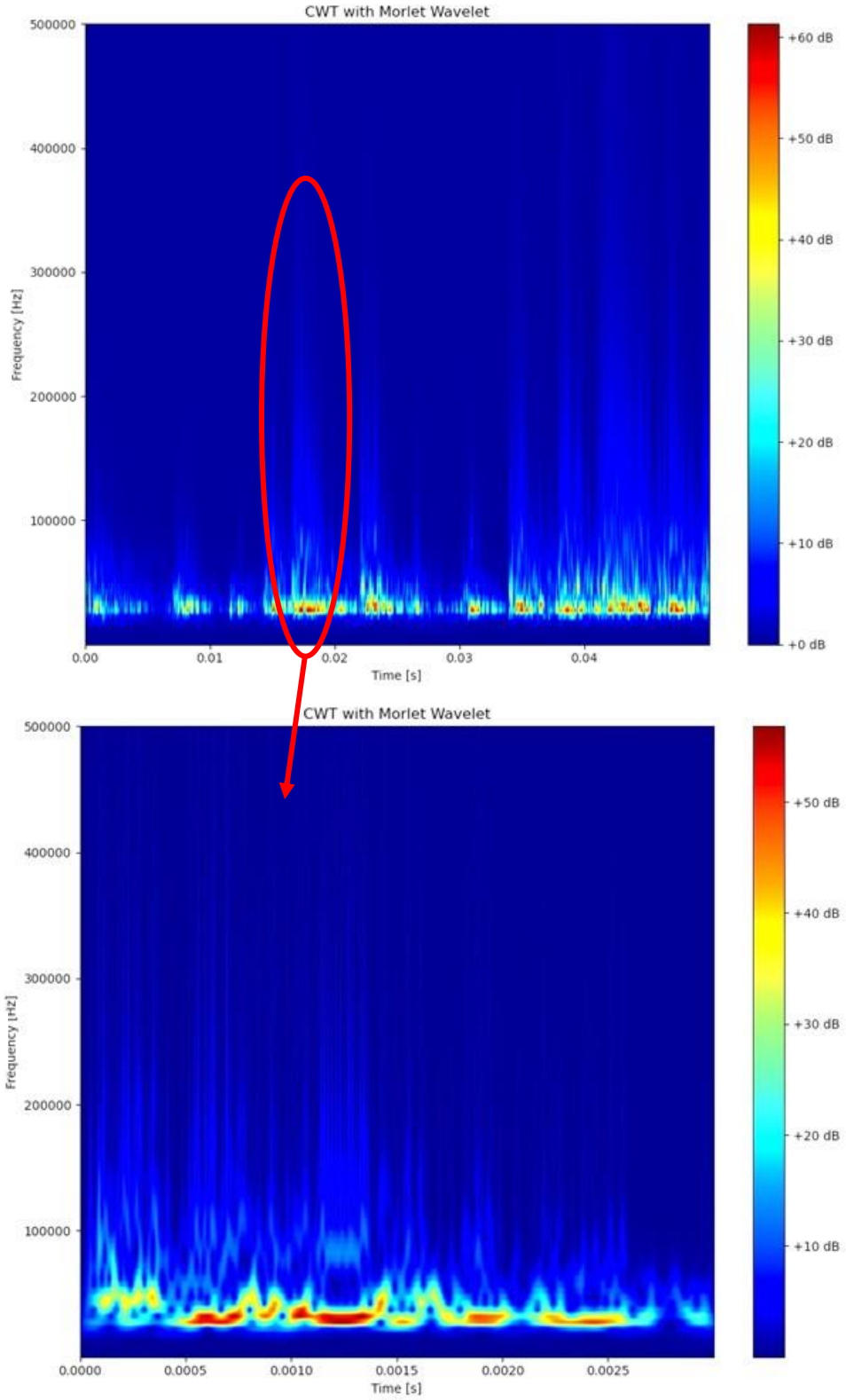

Figure 32 Ambient noise affected signals in HTL loop

3.4 Machine Learning Analysis in Defect Analysis

Considering the challenges of managing large datasets characterized by complicated noise interference in real-world data analysis, traditional methods often fall short in efficiently classifying such complex data. To address this problem, machine-learning algorithms, such as artificial neural networks (ANNs), support vector machines (SVMs), and relevance vector machines (RVMs), have been widely adopted for fault diagnosis and damage detection (de Oliveira & Marques, 2008). In recent years, convolutional neural networks (CNNs) have demonstrated exceptional capabilities in handling intricate, high-dimensional data (D. Li et al., 2021).

CNNs are designed to automatically and adaptively learn the grid-like topology of datasets, such as images or time-series data, through multiple layers of processing. Their architecture, which includes convolutional layers, pooling layers, and fully connected layers, allows them to capture complex patterns while reducing computational costs through parameter sharing and dimensionality reduction. CNNs have proven to be highly successful in a wide range of applications, including image detection, segmentation, and pattern recognition. In the context of structural damage detection, CNNs have been used to analyze visual images, vibration signals, and AE signals with remarkable accuracy. Their ability to process and interpret AE signals' spatial and temporal features makes CNNs especially suited for identifying subtle patterns that may indicate the presence of defects.

In the following chapter, we will utilize CNNs to process two-dimensional representations of time-series data; we aim to improve the robustness and reliability of our fault detection system, ultimately contributing to more efficient and accurate railway maintenance and safety protocols.

3.4.1 CNN Model for AE Classification

The application of CNNs which is traced back as early as 1998 (Lecun et al., 1998) have revolutionized various fields, including activity recognition, sentence classification, text recognition, face recognition, object detection, image characterization, and more. The power of CNNs lies in their unique architecture, which mimics the visual cortex's processing of visual stimulations. This makes CNNs particularly effective for high-dimensional data such as images and videos. A typical CNN architecture consists of several layers, including convolutional layers, pooling layers, and fully connected layers, each playing a crucial role in the network's ability to learn and generalize from data.

The convolutional layer in CNNs is the key element that extracts features from input data through a process known as convolution. The convolution operation involves applying a set of learnable filters (kernels) to the input data. These filters slide across the input's spatial dimensions (height and width), computing the dot product between the filter weights and the corresponding input regions, resulting in a series of activation maps. Each filter in the convolutional layer is responsible for identifying specific patterns or features, such as edges, textures, or more complex structures in the input data. These patterns can be recognized across different spatial locations, making convolutional layers particularly effective for tasks involving spatial data, like images. The output of the feature map in the convolutional layer is computed by the equation:

$$x_j^l = \int \left(\sum_{i \in M_j} x_i^{l-1} * k_{ij}^l \ + b_j^l \right) \tag{5}$$

where x_i^{l-1} represents the ith feature map in the previous layer $l-1$. k_{ij}^l is the weight matrix of the jth filter in the llllth layer. b_j^l is the bias associated with the jth filter. M_j denotes the set of input feature maps contributing to the jth feature map in the layer. The operator $*$ denotes the convolution operation and $f(\cdot)$ is the activation function.

Activation functions are essential in deep learning models like CNNs because they introduce non-linearity, allowing the model to learn complex patterns. Without them, the model would be limited to linear relationships. The Rectified Linear Unit (ReLU) is a commonly used activation function because it effectively mitigates the gradient vanishing problem and promotes faster convergence during training, making it a strong choice for enhancing model performance and generalization.

$$ReLU(x) = \begin{cases} 0, \ if \ x \leq 0 \\ x, \ if \ x > 0 \end{cases} \tag{6}$$

Pooling layers reduce the spatial dimensions of feature maps from convolutional layers, decreasing the number of parameters and computational load. This simplification speeds up training and helps prevent overfitting. Max pooling, the most common pooling method, selects the maximum value from each cluster of neurons. The output x_j^l of the jth feature map in the lth pooling layer is given by:

$$x_j^l = f\left(\beta_j^l \cdot down(\ x_i^{l-1}) \ + b_j^l \right) \tag{7}$$

where $down(\cdot)$ represents the down sampling function, and β_j^l and b_j^l are the multiplicative and additive biases. Pooling layers merge similar features and remove unnecessary details, enhancing the model's robustness and translation invariance.

Fully connected (FC) layers play a crucial role in the final stages of CNNs. These layers take the high-level features extracted by the convolutional and pooling layers and flatten them into a single vector. This vector serves as the input to the FC layers, where each neuron is connected to every neuron in the previous layer. This dense connectivity allows the network to combine and process the extracted features comprehensively. In an FC layer, the activations are computed by performing a matrix multiplication between the input vector and a weight matrix, followed by adding a bias term. The result is then passed through an activation function to introduce non-linearity, enabling the model to capture complex relationships in the data. The output x^l of the lth FC layer is expressed as:

$$x^l = f(\omega^l x^{l-1} + b_j^l) \tag{8}$$

where ω^l represents the weight matrix and b_j^l is the bias vector. The activation function $f(\cdot)$ introduces the necessary non-linearity for capturing complex patterns. FC layers are typically used at the end of CNNs to aggregate the learned features and perform the final classification or

regression tasks, making them essential for tasks like image recognition, object detection, and more.

The loss layer is another essential in guiding the training process of a neural network by quantifying the difference between predicted outputs and actual labels. This feedback mechanism allows the network to adjust its parameters, refining its predictions with each iteration. In the context of deep convolutional neural networks, the SoftMax loss function is particularly suited for single-class prediction tasks where the classes are mutually exclusive. The SoftMax function transforms the raw output scores (logits) from the network into a probability distribution across all classes. This ensures that the sum of all probabilities equals one, effectively normalizing the output and making it interpretable as a probability. The SoftMax function for a class j is defined as:

$$P_j = \frac{e^{z_j}}{\sum_{k=1}^{C} e^{z_k}} \tag{9}$$

where z_j is the logit for class j, and C is the total number of classes. The probability P_j represents the likelihood that the input belongs to class j. The corresponding SoftMax loss, also known as categorical cross-entropy loss, is then computed as:

$$Loss = -\sum_{j=1}^{C} y_j \log(P_j) \tag{10}$$

where y_j is the true label encoded as a one-hot vector, meaning that $y_j = 1$for the correct class and $y_j = 0$ for all other classes. This loss function measures the dissimilarity between the predicted probability distribution and the true distribution (the actual class label), guiding the network to make accurate predictions.

The CNN model employed in this study is custom designed to accommodate various needs, such as dataset variations and CNN dimension modifications. In past research, CWT plots were utilized as data inputs for CNN analysis (D. Li et al., 2021), which converted acoustic datasets into image datasets. However, the resolution and plotting method of the images significantly influenced the outcome of CNN models. In this study, Mel Frequency Cepstral Coefficients (MFCCs) and their deltas were introduced to extract the features of datasets and utilized as input datasets. MFCCs represent the short-term power spectrum of a sound signal commonly used in acoustic processing. They are derived by taking the Fourier transform of a signal, mapping the powers of the spectrum onto the Mel scale, and then applying a logarithm transformation, followed by the inverse Fourier transform. The resulting coefficients provide a compact and perceptually relevant acoustic signal representation. The deltas of MFCCs, also known as delta coefficients, capture temporal dynamics by calculating the difference between consecutive MFCCs. Such delta coefficients provide additional information about how the acoustic features change over time, enhancing the ability to recognize patterns in acoustic signals. MFCCs and their deltas are commonly used as features in machine learning models for tasks like speech recognition and audio classification.

In this study, the model took MFCCs and deltas as input, initially structured into 256 × 98 × 2, where 256 represents the number of Mel bands, 98 is the number of frames, and two channels denote the original MFCCs and their delta values. The architecture comprised multiple convolutional layers with batch normalization and ReLU activation functions to ensure stable and

efficient learning, as shown in Figure 33. The convolutional layers progressively extract features from the input data, with the layers and the subsequent layers using various filter setups, with the consideration of optimizing the classification rate. The kernel size was set to 3 × 3. Max pooling layers with a pool size of 2 × 2 followed each convolutional layer, reducing the spatial dimensions of the feature maps while retaining the most salient information. A global max pooling layer was incorporated to condense the feature maps further, followed by fully connected layers. The first dense layer had 16 units with ReLU activation, and the output layer consisted of 2 units with SoftMax activation, corresponding to the two classes in the classification task. The model was compiled with the Adam optimizer, using a learning rate 1e-4, and trained with the sparse categorical cross-entropy loss function, with accuracy as the primary evaluation metric. To ensure robust performance, the model undergoes K-fold cross-validation, allowing it to be trained and validated on different data splits, providing a comprehensive evaluation of its classification capabilities. However, the data structures were modified to optimize the training performance, including revising the layer numbers, input structure, and layer filter amount.

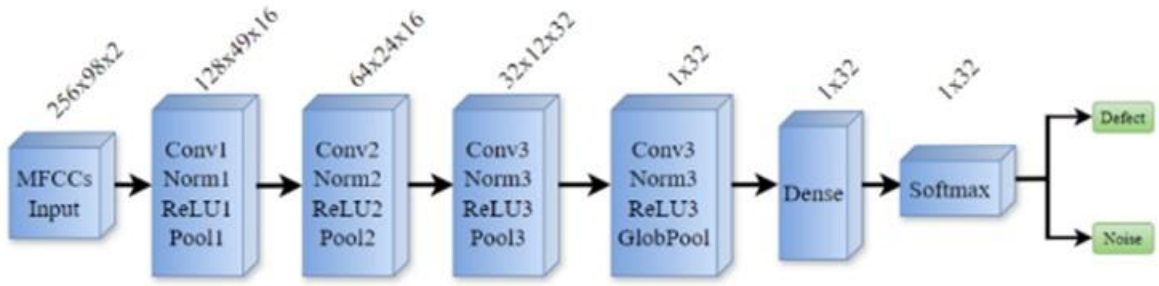

Figure 33 General architecture for defect classification

3.4.2 Training Process and Results

The datasets used in the training consist of potential AE signals extracted from defect locations from the HTL loop tests and non-AE signals, including ambient noise and impulse-like mechanical vibrations, extracted from non-defect areas. Like before, a preliminary time window of 0.05 seconds was initially employed for data processing. However, to accurately label the datasets for the CNN model, it is essential to determine an appropriate time window length that captures AE signal components while excluding unrelated signal components.

Basic setups for the used devices in relation to parameters used in analysis are as follows. The GoPro frame rate was set to 60 Hz at its the highest resolution, with an error margin of ±0.017 seconds. Additionally, the defect zone was set at 15 inches-a value deemed appropriate based on information from TTCI and considering the maximum testing speed of 40 mph, corresponding to a passing time of 0.02 seconds. Consequently, a minimum time window length of 0.054 seconds was determined for the datasets. To ensure that all AE signal components were captured, the time window was finally doubled to 0.11 seconds.

The AE signal datasets were selected through visual inspection, focusing on those exhibiting significant AE characteristics or those combined with ambient noise. As previously mentioned,

data from the three identical sets of sensors were used in the analysis. Consequently, the total number of datasets extracted from defect areas, regardless of whether AE signals were detected, was 31 defects per run ×12 runs × 3 sensor sets = 1,116. Additionally, noise datasets were extracted from noisy areas, resulting in a total of 756×3=2,268 samples. To start with the training, the dataset was set up as explained in the previous chapter; each CNN model utilized K-fold cross-validation (with K= 7) to ensure robustness and minimize overfitting.

In the initial trials, two configurations of convolutional layers and dataset sizes were evaluated: 8×8×16×16 for the first setup and 16×16×32×64 for the second. In both configurations, 1,116 samples were utilized as defect datasets, and 2,268 samples were employed as noise datasets. As shown in Table 3, the 8×8×16×16 setup exhibited consistently low-test accuracy and training accuracy, suggesting that this simpler architecture may not effectively capture the necessary features for the datasets in this analysis. In contrast, the 16×16×32×64 architecture achieved higher training accuracy and lower training loss, indicating better model fitting. However, the test accuracy showed fluctuations, suggesting potential overfitting issues or poor-quality data in the sets. Therefore, as an effort to improve the quality of training data and enhance model's generalization, data lacking significant AE patterns was removed from the training.

In
Table 4, around 25% of the poor-quality data was removed from the defect dataset, and the same portion of the noise data was removed from the noise dataset randomly to maintain the data proportions the same as before. In this follow-up analysis, both configurations (8×8×16×16 and 16×16×32×64) were re-evaluated using datasets that included only potential AE data, as shown in the
Table 4.

Compared with the previous setup, which included all data from defect zones, this refined dataset increased model performance in both configurations. For the 8×8×16×16 configuration, the test accuracy showed a significant increase, particularly reaching 84% one-fold, with the F1 score also improving to a maximum of 0.716, which is promising. This suggests that even simpler architectures can achieve better generalization when data quality is improved by filtering out irrelevant data. Conversely, the 16×16×32×64 configuration showed signs of overfitting, with high training accuracy but less consistent test accuracy, along with fluctuations in performance. Although there were some improvements in the F1 score, reaching up to 0.6, the overfitting suggests that more complex architectures may not necessarily improve precision or generalization. However, while the refinement of data improved performance, the overall test accuracy still remained lower than expected, indicating that further improvements in defect data quality are necessary for achieving higher accuracies. This highlights that simply removing bad data might not be sufficient; enhancing the overall quality and relevance of defect data is crucial for better model performance.

Table 3 Training results with full datasets

Conditions	Defect samples	Noise samples	Layers	Training accuracy	Training loss	Test accuracy	F1 score
	1116	2268	8*8*16*16	0.771	0.486	0.693	0.356

All the data in defect zone				0.791	0.449	0.741	0.42
				0.785	0.453	0.708	0.492
				0.79	0.471	0.703	0.388
				0.822	0.394	0.693	0.519
				0.793	0.448	0.651	0.412
				0.819	0.394	0.571	0.455
All the data in defect zone	1116	2268	16*16*32*64	0.959	0.21	0.73	0.54
				0.97	0.22	0.77	0.53
				0.96	0.2	0.69	0.34
				0.96	0.18	0.82	0.68
				0.94	0.23	0.67	0.55
				0.94	0.2	0.64	0.51
				0.96	0.19	0.56	0.49

Table 4 Training results with potential AE data only

Conditions	Defect samples	Noise samples	Layers	Training accuracy	Training loss	Test accuracy	F1 score
Potential AE data only	831	1671	8*8*16*16	0.865	0.292	0.7	0.475
				0.97	0.15	0.72	0.453
				0.97	0.136	0.49	0.485
				0.965	0.148	0.73	0.417
				0.94	0.21	0.84	0.691
				0.98	0.13	0.78	0.716
				0.99	0.11	0.76	0.725
Potential AE data only	831	1671	16*16*32*64	0.99	0.09	0.73	0.57
				0.99	0.11	0.78	0.6
				0.98	0.17	0.75	0.61
				0.99	0.11	0.73	0.37
				0.98	0.16	0.72	0.51
				0.97	0.16	0.7	0.54
				0.99	0.1	0.58	0.42

In response to the challenge with defect data quality, this project separated the internal defects (transverse defects) and external defects (surface defects) into two distinct datasets. These datasets were then fed into the model separately to determine whether the accuracy results would improve with higher clarity in provided defect data. Out of the 831 defect samples presented in Table 4, 399 data samples were categorized as internal defects and the remaining 432 were designated as external defects.

Initially, the layers were set as 8×8×16×16 to possibly avoid overfitting or underfitting. As shown in Table 5, the results for the internal defects (transverse defects) indicated a range of test accuracies from 0.55 to 0.71, with corresponding F1 scores ranging from 0.09 to 0.36. The training

accuracy varied between 0.73 and 0.78, while the training loss was relatively stable, ranging from 0.47 to 0.53. Despite some improvement in test accuracy, the F1 scores suggest that the model's ability to balance precision and recall was still limited. As to the external defects (surface defects), the results show a similar trend, with test accuracies ranging from 0.57 to 0.66 and F1 scores between 0.03 and 0.24. The training accuracy was slightly higher, reaching 0.82, with training loss decreasing to as low as 0.45. However, the lower F1 scores indicate that while the model was able to achieve better training accuracy, it still failed to properly classify the defects and noises.

Table 5 Training results with internal (a) and external (b) defects only

(a)

Conditions	Defect samples	Noise samples	Layers	Training accuracy	Training loss	Test accuracy	F1 score
Transverse defects only	399	798	8*8*16*16	0.73	0.53	0.67	0.17
				0.74	0.52	0.66	0.19
				0.77	0.5	0.63	0.29
				0.76	0.5	0.71	0.36
				0.74	0.52	0.64	0.14
				0.76	0.5	0.64	0.26
				0.78	0.47	0.55	0.09

(b)

Conditions	Defect samples	Noise samples	Layers	Training accuracy	Training loss	Test accuracy	F1 score
Transverse defects only	432	864	8*8*16*16	0.73	0.54	0.66	0.15
				0.79	0.5	0.65	0.24
				0.76	0.53	0.65	0.03
				0.74	0.53	0.64	0.18
				0.76	0.51	0.64	0.08
				0.82	0.45	0.59	0.21
				0.76	0.5	0.57	0.15

These results suggest that separating the defects into internal and external categories did not lead to significant improvements in the model's overall performance, particularly in terms of the F1 score, which remained low in both cases. After such attempts, no significant improvement of overall performance was observed, the quality of the raw data collected in the field tests was necessary to be validated.

3.5 Additional Tests to Validate Data Quality

The tests that have been conducted so far emphasized the importance of data quality, leading to several critical questions with respect to system capability to collect quality data and adequateness of system deployment, which mounts sensors onto a train frame as a non-contact method. In fundamental investigations into these aspects, additional tests were designed. A series of pencil lead break (PLB) tests were conducted both in the lab and in the field. The PLB test is also known as the Hsu-Nielsen test, is commonly employed to replicate AE signals by breaking the tip of a pencil lead against the material surface. As the pencil lead in a specially designed pencil breaks,

an elastic wave can be generated as a result of the sudden stress release. The ASTM E976-15 (Astm, 2021) recommends using a mechanical pencil with 2H leads of 0.5 mm diameter as the AE source for reliable results. Each lead to be broken was approximately 3 mm in length. The Nielsen shoe is used to position the pencil lead correctly towards the testing materials at a 30° angle (Figure 34). Researchers adopted PLB as a simulation tool to produce AE signals and investigate the acoustic features of AE signals.

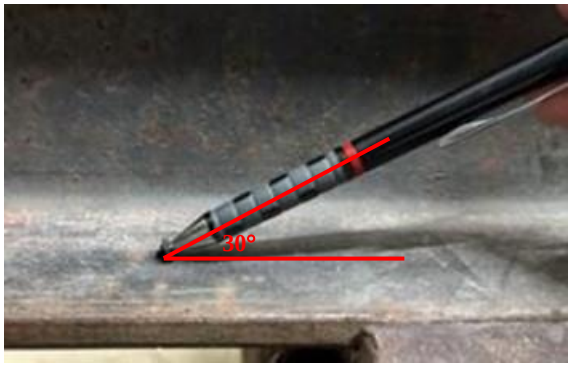

Figure 34 PLB test

The first question focused on whether the detection prototype was properly configured to receive AE signals. To evaluate the system setup and ensure the prototype's ability to capture acoustic signals accurately, a PLB test was made with sensors attached to the surface of a steel plate. The results from this test were positive, with the time-frequency analysis clearly indicating successful detection of the PLB signals (Figure 36).

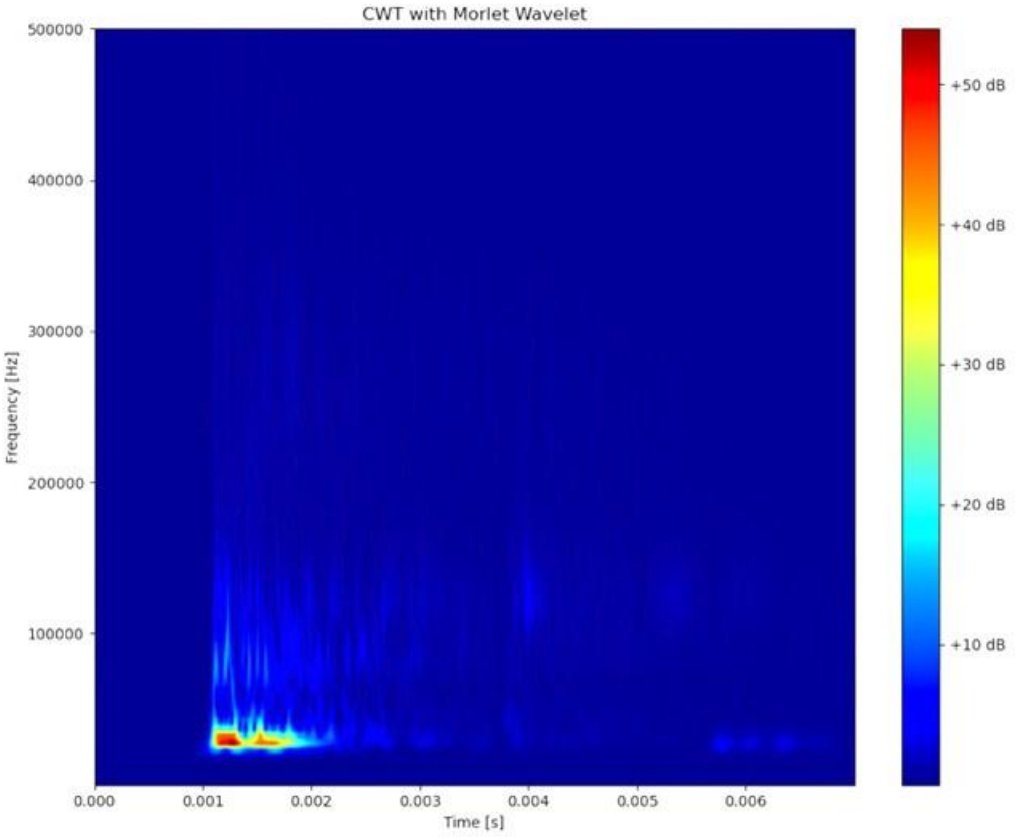

Figure 35 PLB test on steel plate

The second question aimed to determine whether AE signals generated in the rail could be effectively captured by sensors mounted on the train frame. For this evaluation, a field test was conducted at the Nevada Railroad Museum. Sensors were installed at various locations on the wheel and suspension frame, and PLB tests were performed multiple times under the rail head to simulate AE signal generation. These tests were designed to verify if the AE signals could propagate through the rail into the wheel and be detected by the sensors. However, the results from the second test were discouraging with all sensor locations failing to capture the AE signals properly. The tests were repeated multiple times at various sensors to verify the outcome. In all cases, the PLB signals were not properly detected by the sensors, regardless of their installation positions. This consistent failure suggests that the AE signals were unable to propagate through the rail into the wheel without the presence of a coupling medium (e.g., couplant or other lubricant). Based on these findings, it can be concluded that the acoustic signals collected in previous tests at the TTCI and the Nevada Railroad Museum did not originate from the rails but from the train itself. These signals were likely mechanical vibrations that presented similar patterns of AE signals, which explains the consistently low performance of the machine learning model. Given that the bone-conduct sensors cannot capture AE signals when installed on trains, it is necessary to explore alternative methods for collecting acoustic signals that do not suffer from propagation issues. This exploration is critical to improving the capability of AE signal detection in field applications.

CHAPTER 4 RAIL INTERNAL DEFECT DETECTION USING AIR-COUPLED SENSORS

4.1 Introduction

Building on the conclusions from the previous work, it became evident that a new approach was necessary for collecting AE signals when sensors are mounted on vehicles as a non-contact method of railroad inspection. Note that the non-contact method of railroad inspection addresses one of the key limitations of contact-based methods—sensor network issues—positioning itself as a promising and practical approach for effective railroad inspection Per literature and previous investigations, it was found that acoustic sensors must meet specific technical requirements: (1) they should have a wide and flat frequency response range, typically between 20-500 kHz as required in this study, and (2) they must provide high signal gains through amplification, given that the energy of AE leaky waves in the air is significantly lower than in the rails.

Air-coupled piezoelectric sensors are widely used in non-contact ultrasonic inspection due to their effectiveness in detecting AE signals, although they have yet to be fully tested and validated as an promising solution in challenging railroad inspection. These sensors typically operate at a fixed frequency because they are paired with an ultrasonic generator operating at the same frequency. Their frequency response of such sensors is generally limited to ±10% of the designated working frequency. This requires the use of multiple sensors at different frequencies to cover a broader frequency range. This can potentially lead to frequency response fluctuations and challenges in data integration.

In addition to traditional piezoelectric sensors, optical microphones have gained attention for their innovative technology and superior performance in non-contact ultrasonic detection. The nature of air-coupled AE waves makes it feasible to develop non-contact sensors for detecting rail defects using this technology. As illustrated in Figure 36, when a monochromatic laser beam propagates through a medium in the presence of a sound field, it experiences slight modulation in its optical wavelength, which is proportional to the local density and, consequently, the sound pressure. The core component of the optical microphone is a miniaturized Fabry-Perot cavity, consisting of two semi-reflective mirrors. The intensity of the laser light reflected from this cavity is determined by the product of the input intensity and a transfer function. The round-trip phase shift depends on the laser wavelength and the distance between the mirrors. Therefore, any change in the laser wavelength induced by the sound field alters the light intensity, which is reflected by the cavity and can be detected by a photodiode.

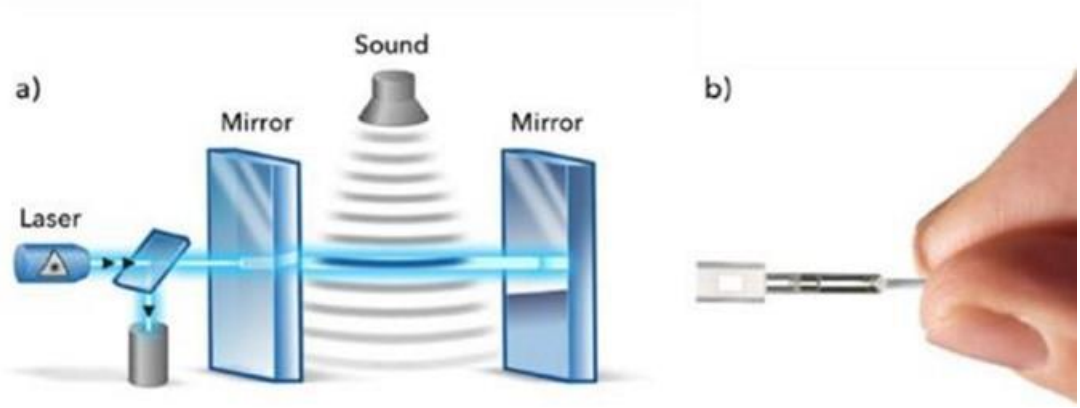

Figure 36 The optical microphone: a) mechanism. b) sensor head

Unlike bone-conduct sensors utilized in the previous field tests, this non-contact approach utilizes air-couple sensors to record AE signals. As mentioned previously, traditional piezoelectric ultrasonic sensors generally work within a limited frequency bandwidth (±10% of the resonate frequency). The optical microphone is introduced in this approach to address this limitation. This advanced technology has been extensively studied and has demonstrated exceptional performance, making it a promising candidate for non-contact AE detection. It is proposed to detect defects in steel plates where a laser is used to activate the AE wave (Fischer, 2016; Rohringer et al., 2018). The thickness of the steel plate is below one inch, which is much thinner than that of the rail used in the railroad as shown in Figure 37. The key question is whether the optical microphone sensor can detect internal and external defects located far from the sensor.

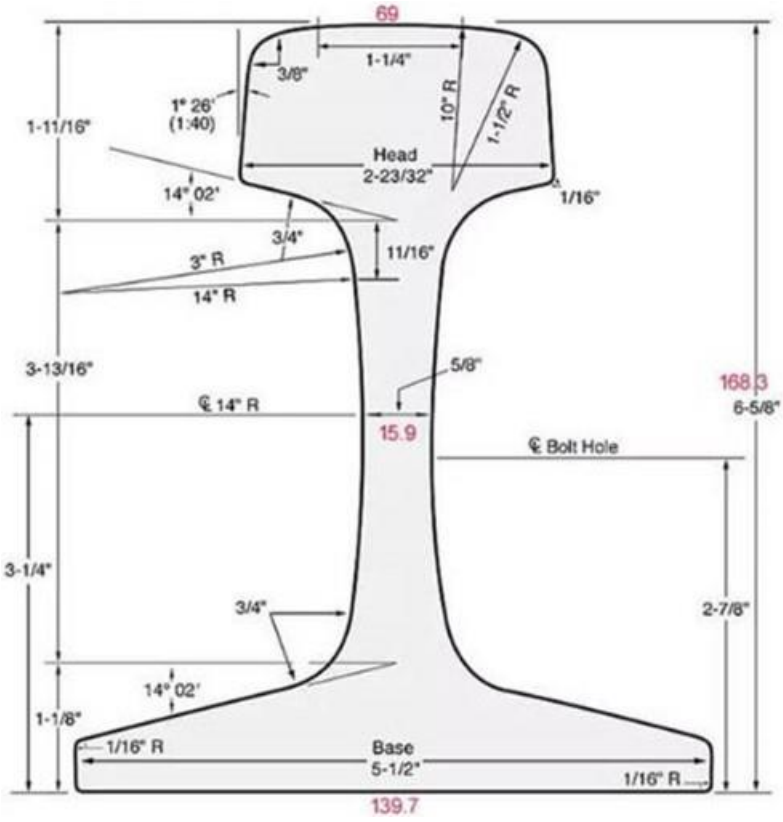

Figure 37 Rail size of 115 Re Rail

It is important to note that the mirror distance in Figure 36 is completely fixed; no mechanical movement or deformation takes part in the detection process, which would limit the detection bandwidth, and no inert mass limits the impulse response or causes ringing. Light is coupled to the sensor via a fiber-optical cable connected to a remote unit containing the laser, control, and detection electronics. Therefore, the sensor head is a passive optical element immune to electromagnetic interference on both the sensor head and cable.

4.2 Propagation and Attenuation of AE waves

The complexity of AE signals is influenced by two main factors: the source characteristics and the propagation path. The features related to the source depend on the type and material of the defect, while the propagation path is predominantly determined by the geometry of the structure. In AE applications, sensors are typically deployed to identify potential defects in structures over distances ranging from several to tens of meters. Thus, it is crucial for this study to explore the propagation characteristics of AE waves in the rail head, including aspects such as energy attenuation and wave dispersion.

4.2.1 AE Energy Attenuation

The energy of AE waves attenuates as they propagate due to four mechanisms: geometrical propagation, internal friction, scattering, and diffraction (Nivesrangsan, 2004). Geometrical

spreading causes attenuation as waves initialing from a point source spread over a larger wavefront. The amplitude of the wave A diminishes inversely with distance d in three-dimensional solids $A \propto 1/d$, and inversely with the square root of distance in two-dimensional solids $A \propto 1/\sqrt{d}$. Internal friction is a process where mechanical energy is converted to thermal energy as waves propagate through non-conservative media, contributing to amplitude reduction. This material-dependent effect causes amplitude to decay exponentially with distance $A \propto e^{-kd}$, where k is an attenuation factor (Finlayson et al., 2003), waves encountering complex boundaries or discontinuities such as holes, slots, inclusions, or cracks undergo scattering and diffraction. Scattering occurs when waves interact with finite voids or inclusions, while diffraction happens at sharp edges like cracks. Both phenomena contribute to reduced wave amplitude with increasing distance.

In general, significant attenuation initials in the near field of the AE source are mainly caused by geometry spreading. While in the far field, internal friction dominates, resulting in an exponential attenuation relationship with distance, whereas dispersion plays a limited role in this context (Pollock, 1986). The AE signal attenuation in real-world scenarios is generally investigated by conditions-controlled tests, such as collecting AE signals by placing sensors at different locations.

4.2.2 Wave Modes of AE Signals

AE wave modes are influenced by different boundaries, including body waves, surface waves, plate waves, guided waves, and others (Ensminger & Bond, 2011). The body waves generally propagate in infinite media, including longitudinal and transverse waves. In longitudinal waves (or compression waves), particle displacement is parallel to the wave's direction of travel, resulting in the highest velocities among wave types. Transverse waves (or shear waves) feature perpendicular displacement relative to the propagation direction.

Another wave mode is the surface waves, such as Rayleigh waves, which travel along the surfaces of semi-infinite media or thick solids, penetrating approximately one wavelength into the material. Combining longitudinal and transverse motion, these waves travel at speeds slightly below shear waves, influenced by material elasticity.

Plate waves, primarily Lamb waves, are confined to thin structures like plates and feature multiple modes. They are categorized into symmetric (extensional) and anti-symmetric (flexural) modes, with particle motion varying between in-plane and out-of-plane. These characteristics, however, may not hold consistently at higher frequencies. Guided waves propagate along elongated structures, such as plates, pipes, and rails, constrained by boundaries (Rizzo, 2009). Although terms like "guided Rayleigh waves" and "guided Lamb waves" better describe the practical conditions, these modes allow long-distance wave travel with minimal energy loss, making them suitable for long-range ultrasonics in rail condition monitoring.

4.3 Pencil Lead Break Tests

As demonstrated in past research, PLB, also known as the Hsu-Nielsen test, was a commonly utilized method to simulate AE signals (Dare de Almeida et al., 2015; Lopes et al., 2018). In this chapter, this project evaluates the attenuation characteristics of AE signals under various

conditions and explores the installation method for mounting the sensor onto the train in the vehicle-mounted test.

In this test, two distinct tests scenarios were designed to assess the attenuation characteristics of AE signals, both within the rail and in the surrounding air. The first test scenario is shown in Figure 38 (a) and (b). Figure 38 (a) focused on evaluating the attenuation of AE signals as they propagate through the rail. In this setup, the optical microphone was positioned near the rail surface to capture AE signals generated by PLB events. The sensor was placed at the top of the rail head. The pencil tip was carefully positioned at the cross-section of the rail head, with a Nielsen shoe used to ensure consistent angles during each pencil lead break, thereby maintaining identical signal sources. The sensor was then moved longitudinally along the rail surface, with PLB tests conducted at varying distances from the PLB point to the sensor, ranging from 0 to 3 inches in 0.5-inch increments. This setup allowed for a thorough investigation of AE signal attenuation within the rail material.

The second test as shown in Figure 38 (b) presents the test conducted to assess the attenuation characteristics of AE signals as they propagate through the air. In this configuration, the sensor head was positioned at the side of the rail head, and the AE signals were evaluated at different distances from the source. This test evaluated how AE signals attenuate as the distance between the sensor and the signal source increases in the air. Since the sensor is intended to be installed without contact with the train, understanding the distance-attenuation relationship is crucial for determining the optimal sensor placement. The testing rail segment and PLB sources used in this scenario were identical to those in the first setup, ensuring consistency in testing conditions. The sensor head was installed at various distances above the rail surface, ranging from 0 to 3 inches in 0.5-inch increments.

By comparing the results from these two scenarios, the study provides valuable insights into the propagation characteristics of AE signals in different environments, which is essential for developing an effective non-contact rail health monitoring system. The testing prototype was the same as introduced in the previous chapters, which is shown in Figure 39.

(a)

(b)

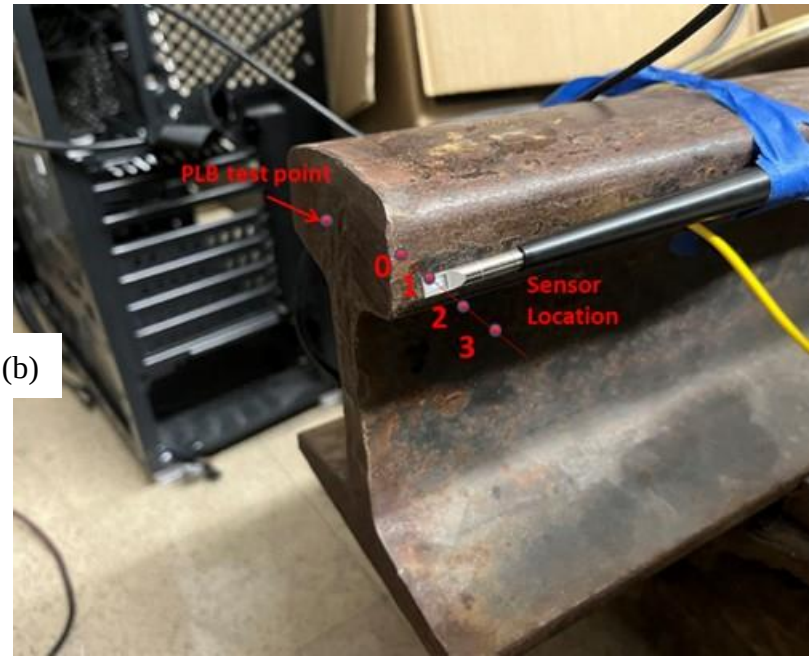

Figure 38 Attenuation Test for AE Propagation (a) in the rail (b) in the air

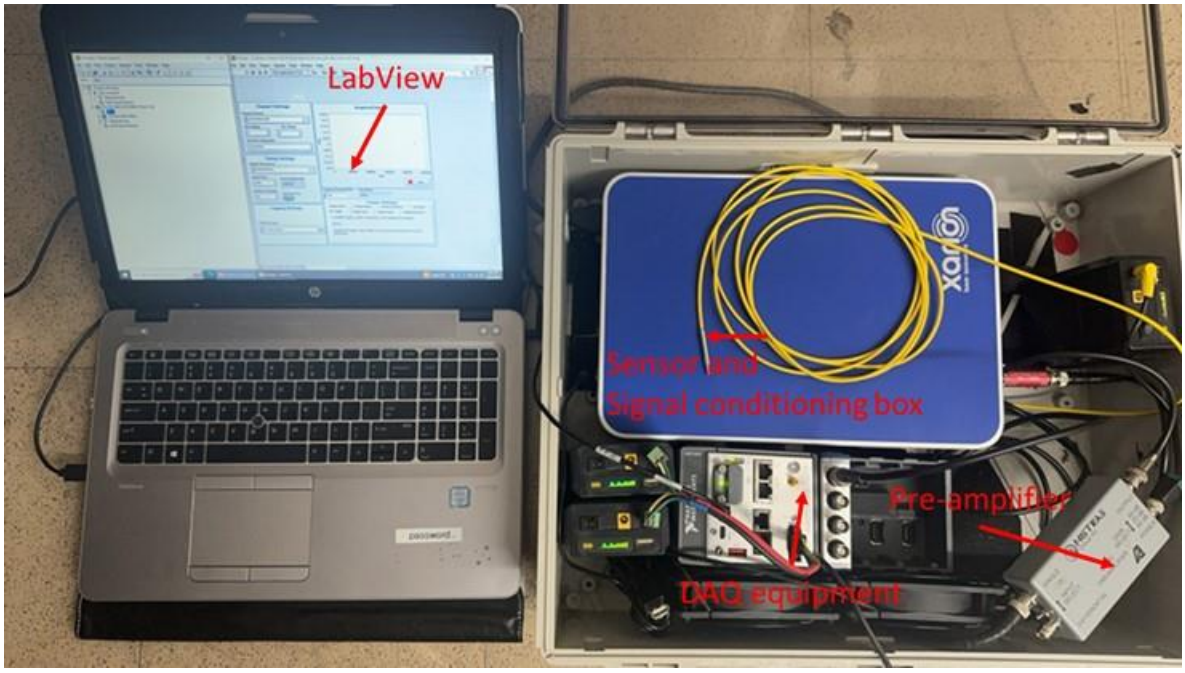

Figure 39 DAQ system schematic

4.4 Rail Internal Defect Detection in Nevada

It is important that we evaluate system detection performance for internal and external defects individually because the distinction between the two defect types is critical for accurate assessment of the detection methods. This studyevaluated rail internal defect detection by testing the air-coupled AE technique in three settings: rail-mounted real-world field tests, and vehicle-mounted field tests. The rail-mounted testing evaluated the performance of the approach in various aspects which are presented later. In the vehicle-mounted testing scenario, the sensors, directly installed on the mounting frame of the train, record the acoustic signals during operation for the same evaluation.

By analyzing the AE signal and noise attributes in the collected data, valuable insights were gained in defect classification and extraction. This initiative effort on the air-coupled sensor system was crucial as they could serve as an important scientific resource and reference for developing an automated, reliable monitoring system as well as for non-contact AE monitoring techniques in the future. The insights obtained from these vehicle-mounted field tests are expected to significantly enhance the understanding of AE characteristics.

4.4.1 Rail-Mounted Field Test

The rail-mounted field test was conducted on a pre-damaged track at the Nevada Railroad Museum. Two internal welding defects were used in this field test, as presented in
Figure 40. The details of the welding defects are shown in Figure 41; the size and location were obtained using the Olympus Epoch 1000i ultrasonic inspector. The sensor head was mounted onto a fixture attached to the rail surface by placing it below the rail head.

Similar to the PLB test setup, this rail-mounted field test evaluated AE attenuation in the air and rail separately. Accordingly, the rail-mounted field test involved two different test setups as shown in Figure 42: 1) the sensor was moved vertically away from the railhead and 2) the sensor was moved horizontally down from the railhead. In the first case, the sensor was adjusted to three different locations as shown in Figure 42 (a), with each subsequent test moving the sensor one inch perpendicularly away from the surface into the air. The second case adjusted the sensor placement in three different locations as shown in Figure 42 (b) by moving it left along the rail web by two inches in the subsequent test.

For the field test, an unloaded hopper car with an axle load of approximately 70,000 lb. was employed, as shown in Figure 43, capable of moving at speeds up to 5 miles/h. A GoPro camera was installed near these defect sites to record the time when the wheel passed over the defects. A hammer hit was used to synchronize the timeline between the video and the signals, allowing precise synchronization of video and AE signal timestamps and ensuring a smooth downstream analysis.

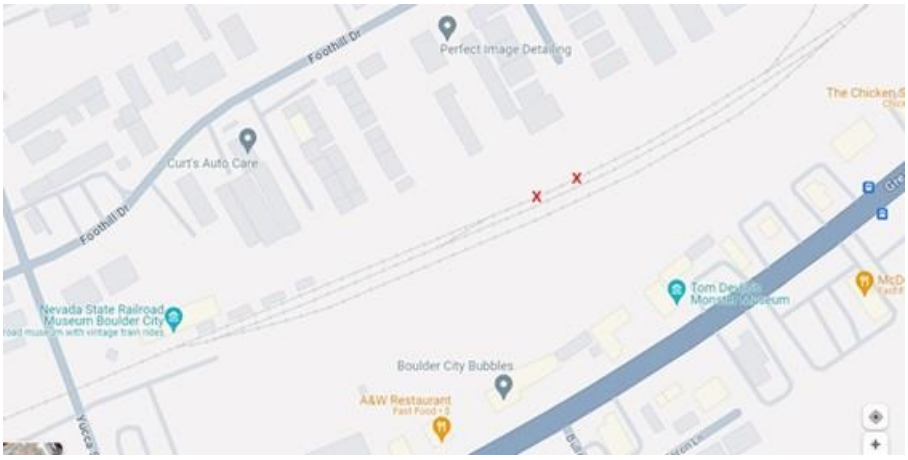

Figure 40 Location of two Internal defects in the Nevada Railroad Museum

Welding defect: 0.3 in * 0.3 in. Location: 1.9 inches below the surface

Welding defect: 0.2 in * 0.3 in. Location: 2.5 inches below the surface

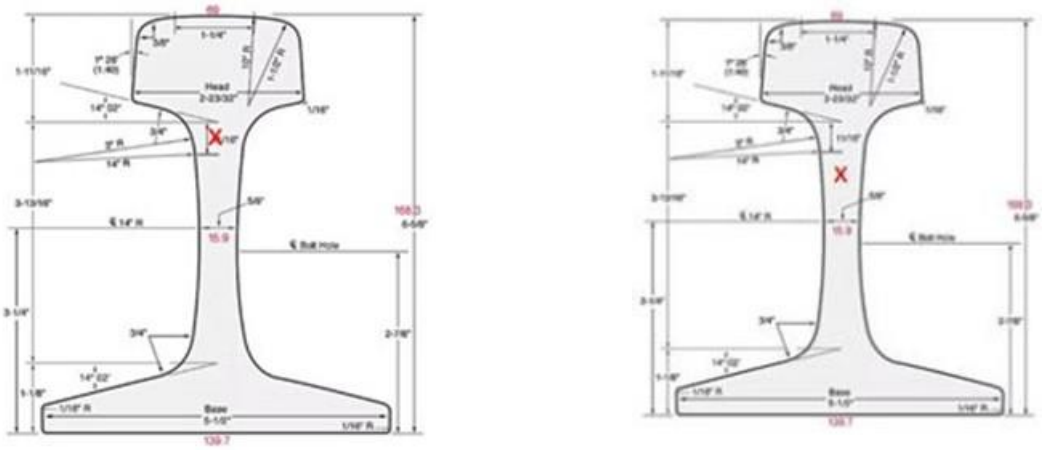

Figure 41 Internal defect location and size

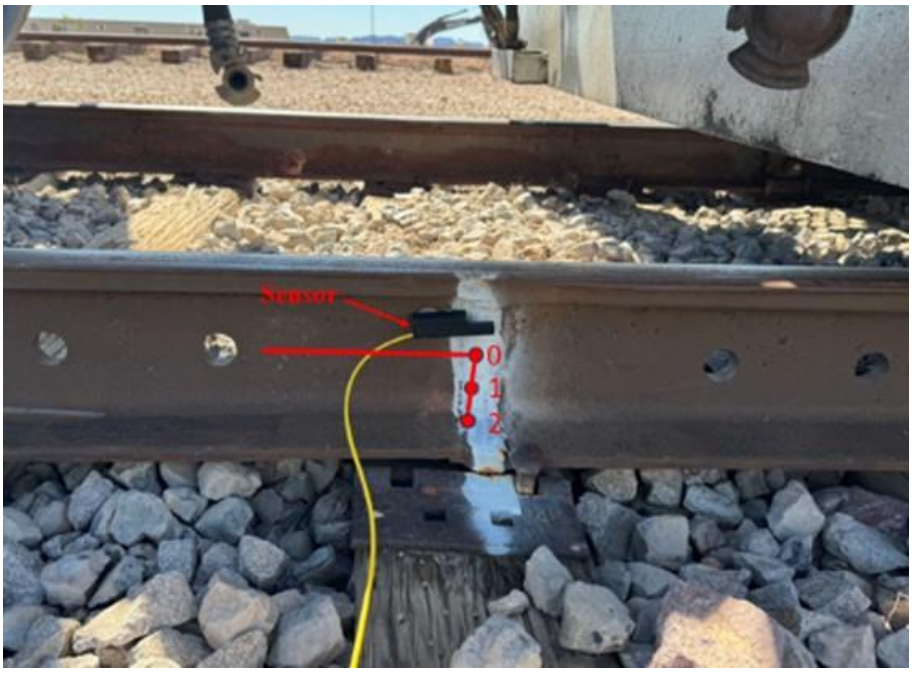

a)

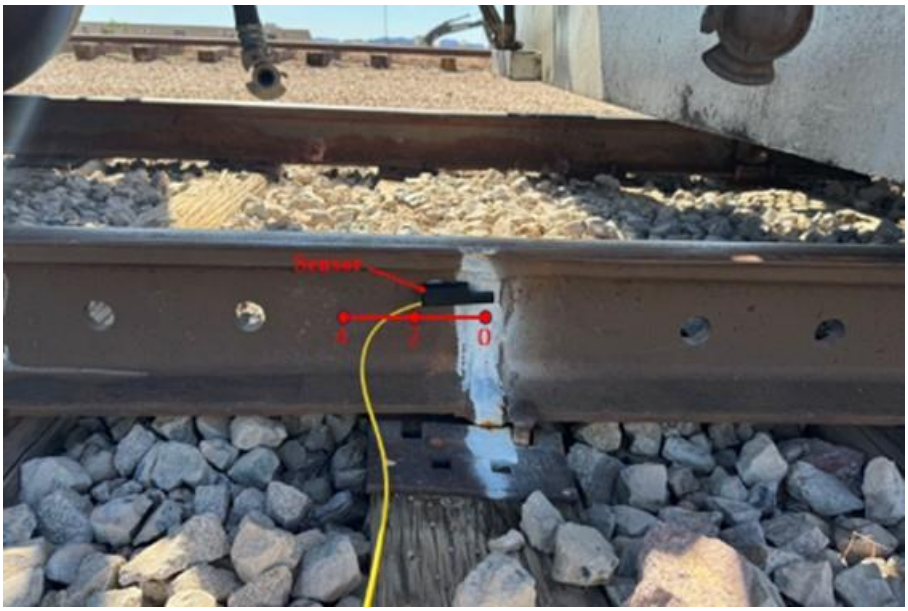

b)

Figure 42 Attenuation evaluation a) vertically in the air; b) longitudinally in the rail

Figure 43 Field test train and hooper

4.4.2 Vehicle-Mounted Field Tests

The vehicle-mounted test was conducted in the same configuration and setup as in the rail-mounted tests, except for the sensor installation location. In this test, the sensor was installed on the mounting frame of the train as shown in

Figure 44. To ensure sensor safety (e.g., not colliding with the rail during the test operation), the sensor was placed 1.5 inches away from the rail head side. Like the rail-mounted test, the sensor location was adjusted from the initial location (Figure 45) by moving it to the far side of the rail by two inches for the subsequent test. A hammer hit was used to synchronize the timeline between the video and the signals, allowing precise synchronization of video and AE signal timestamps and ensuring a detailed downstream analysis.

Figure 44 Mounting frame (front and side views)

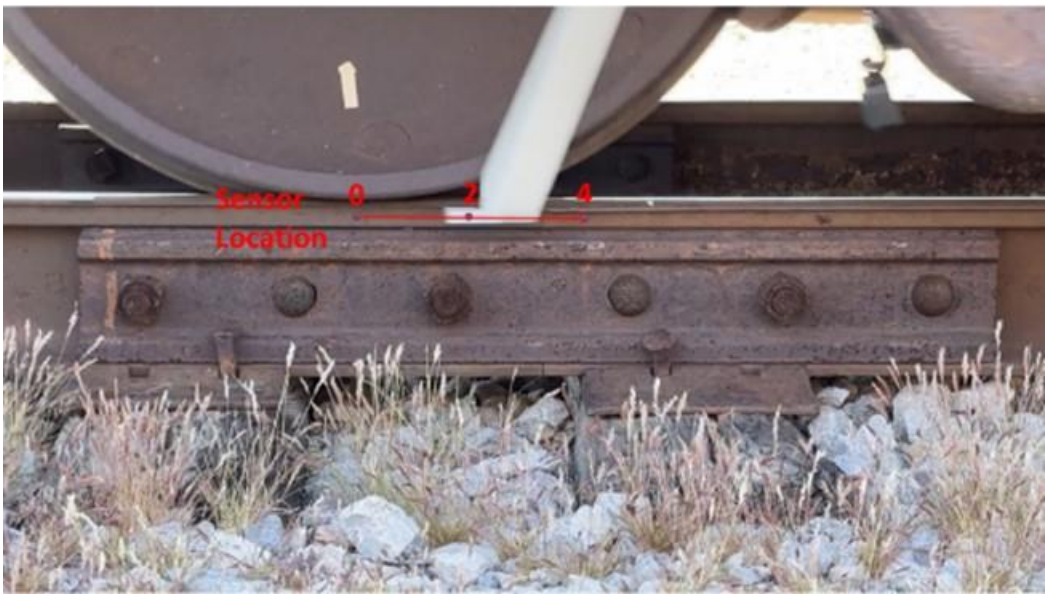

Figure 45 Attenuation evaluation in the rail (longitudinally)

4.5 Rail Internal Defect Detection in MxVRail

The tests at the Nevada Railroad Museum involving two internal defects were critical as a preliminary investigation; however, several challenges were identified after data collection and analysis, leading to the necessity of further evaluation in a more controlled and professional testing environment. The challenges were associated with the site setup with joint bars configuration in the rail which caused significant joint bar impact and thus obscured AE events.

While this project still analyzed and presents the results from the tests at the Nevada Railroad Museum, additional field tests were conducted at MxVRail, rebranded from TTCI. The FAST loop at MxVRail, designed to generate defects naturally through the repeated passage of commercial hoppers, was selected for these tests. The tests at MxVRail also include two test scenarios like before: 1) rail mount and 2) vehicle mount.

4.5.1 Rail-Mounted Field Test

The rail-mounted field test used two naturally generated internal defects shown in Figure 46. Their detailed information as to the defect size and location were provided by MxVRail. The larger defect measured 0.8 inches by 0.6 inches and was situated 0.7 inches below the top surface, indicating that it was in the late stage of development. In contrast, the smaller defect, measuring 0.3 inches by 0.3 inches and located 0.6 inches below the top surface, was still in the early stage of development.

Welding defect 1: 0.8 in x 0.6 in. Location: 0.7 inches below the surface

Welding defect 2: 0.3 in x 0.3 in. Location: 0.6 inches below the surface

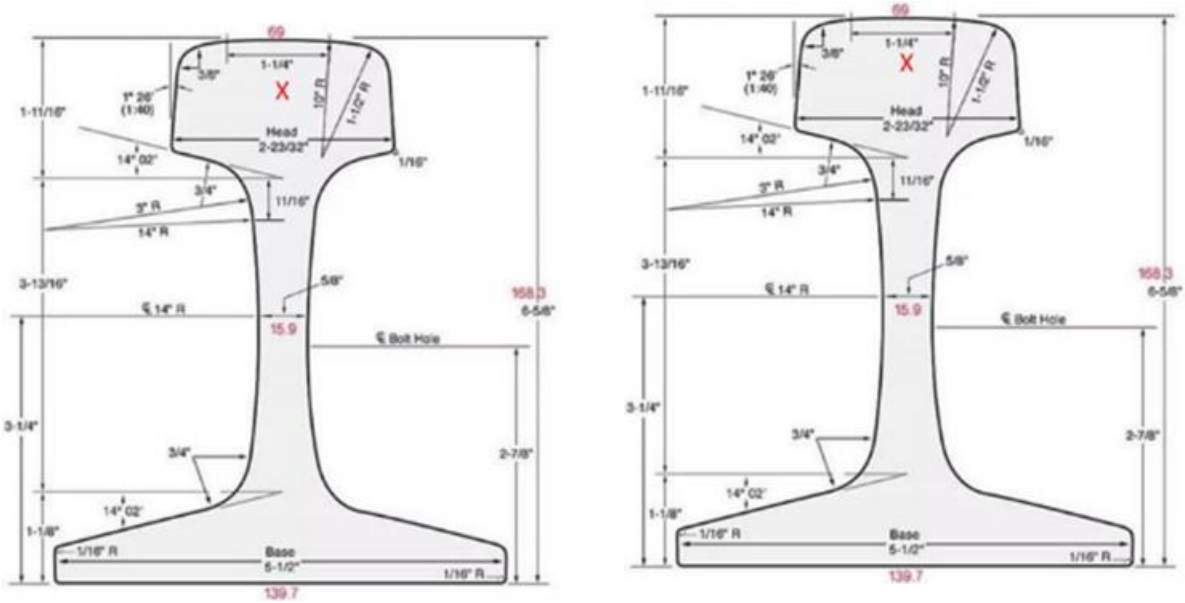

Figure 46 The internal defects

In this test, the sensor head was mounted onto the rail surface. Although the setups were similar to previous field tests, some modifications (i.e., reduced configurations in tests) were necessary due to the site limitation at the time of test at MxVRail. As shown in Figure 47 (a), the sensor was placed under the rail head at the defect location, with distances of 0, 1, and 2 inches from the defect. In Figure 47 (b), the sensor was placed at the same location but then moved laterally to the left by 0, 2, and 4 inches.

Six unloaded hopper cars, each with an axle load of approximately 70,000 pounds, and a locomotive weighing approximately 432,000 pounds were used. Each test conducted 10 repeat runs, with the testing speed set to 5 mph except one test case with 40 mph. The tests resulted in 28 rail-wheel impacts per back-and-forth test run, each capable of generating AE events. A GoPro camera was installed near the defect sites to record the exact moments when the wheels passed over the defects. A hammer strike was used to synchronize the timeline between the video footage

and AE signal data, ensuring precise alignment of video and signal timestamps for detailed downstream analysis.

Unfortunately, the on-rail test for the small internal defect could only be completed partially due to unforeseen damage to the sensor head during the field tests. Despite this setback, the comprehensive approach allowed for a thorough evaluation of the sensor's ability to detect AE signals only from the larger internal defect under varying conditions.

(a)

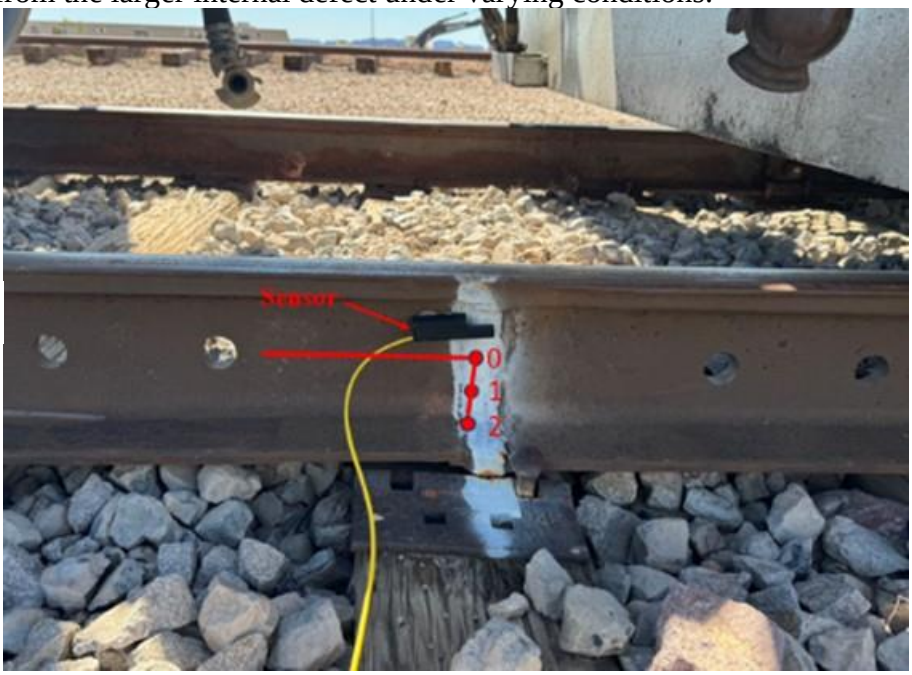

(b)

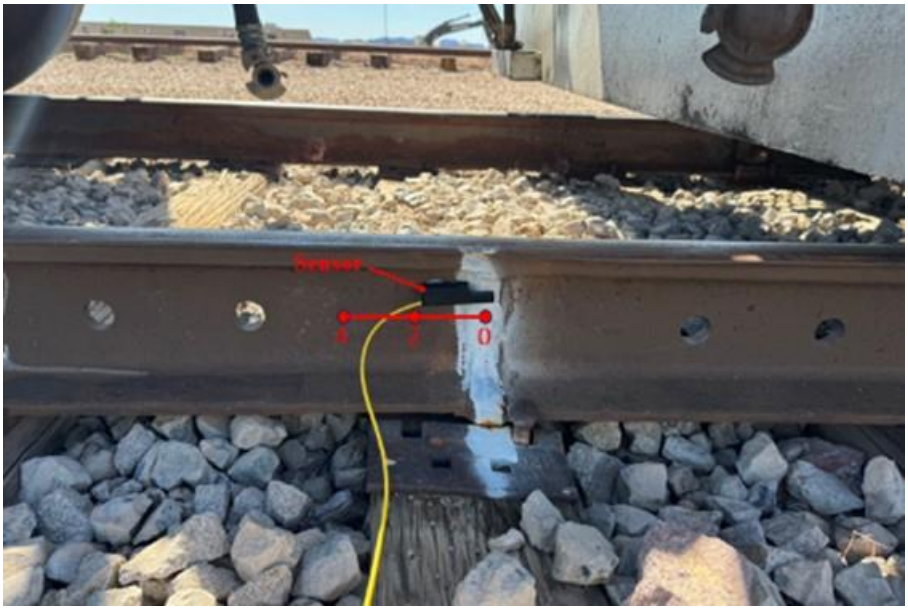

Figure 47 Attenuation evaluation a) vertically in the air; b) longitudinally in the rail

4.5.2 Vehicle-Mounted Field Test

In this testing scenario, the sensor was installed the same way as in the museum test. It was installed on the train's mounting frame, and the acoustic signals were recorded when the train was running over defects (Figure 48). The sensor was designated to be safely placed 1.5 inches away from the rail head side. As in previous tests, the sensor was relocated from its original position to the far side of the defect by moving it from 0 to 4 inches at two inches increment (Figure 49).

Figure 48 Mounting frame (front and side views)

Figure 49 Attenuation evaluation in the rail

4.6 Results and Discussion

The results of three tests (i.e., PLB, Nevada Railroad Museum, and MxVRail) conducted to evaluate the attenuation characteristics and AE signal propagation under various conditions are discussed in this section. The results specifically focus on internal defects in rail structures (Table 6). To quickly recap the tests, the test environments are briefly discussed below prior to discussing them in detail.

The first test involved controlled lab tests utilizing PLB as a consistent AE source to simulate and assess AE signal attenuation within the rail material and surrounding air. In this setup, the sensor was positioned at the top, side, and bottom of the rail head, with offsets of 0, 1, 2, and 3 inches from the defect, and each condition was repeated 10 times to ensure reliable data collection. The second test consisted of field tests conducted at the Nevada Railroad Museum, focusing on the initial evaluation of AE signal characteristics in a real-world environment. The sensor was tested in rail-mounted and vehicle-mounted configurations, with offsets of 0, 2, and 4 inches for rail-based measurements and 0, 1, and 2 inches for air-based measurements, each repeated 10 times. The final testing test occurred at the MxVRail facility, where further evaluation of AE signal characteristics was performed, based on the findings from the Nevada tests. Similar sensor configurations, with the same offsets and repeat counts, provided a thorough assessment of AE signal behavior in different testing environments. These stages collectively contributed valuable insights into optimizing sensor placement and data collection strategies for non-contact rail health monitoring systems.

Table 6 Summary of Internal Defect Tests

Test Location	Sensor Location	Attenuation Evaluated	Test Speed (mph)	Offset From Defect	Number of Repeats	Goal
PLB Test	Top Head side Web	Rail	N/A	0, 1, 2, 3	10 for each	Evaluate AE attenuations
		Air		0, 1, 2, 3	10 for each	
Nevada	Rail-mounted	Rail	5	0, 2, 4	10 for each	Initial evaluation of AE characteristics
		Air	5	0, 1, 2	10 for each	
	Vehicle-mounted	Rail	5	0, 2, 4	10 for each	
MxVRail	Rail-mounted	Rail	5	0, 2, 4	10 for each	Further evaluation of AE characteristics
		Air	5	0, 1, 2	10 for each	

	Vehicle-mounted	Rail	5	0, 2, 4	10 for each	

4.6.1 Time-Frequency Representation of AE Waves

The time-frequency characteristics of AE signals generated by PLB tests and real-world field tests were analyzed using CWT. Figure 50 to Figure 52 display the CWT results of AE signals from different sources. The analysis presents that the wave energy is predominantly concentrated in the low-frequency range of 20-40 kHz, with a notable portion also present in the high-frequency range of 80-130 kHz. Therefore, to enhance the identification of high-frequency features specific to PLB-induced signals and rail defect-induced AE signals, a 100 kHz high-pass filter was applied. As shown in Figure 50 (c) through Figure 52 (c), it shows that the energy is primarily concentrated in the 120-170 kHz range for PLB signals and 110-140 kHz for rail defect signals.

Moreover, distinctive pulse sequences were observed at two-time scales, particularly in Figure 52 (c), where the signal attenuation is gradual, and each pulse indicates a pattern of energy concentration in the center. Figure 53 provides a detailed view of these burst patterns across the two-time scales. It is important to note that these repetitive patterns were not observed across all AE sources; they were not observed in PLB signals and were significantly less frequent in AE signals from the small rail defect than the large defect observed in MxV Rail tests.

(a)

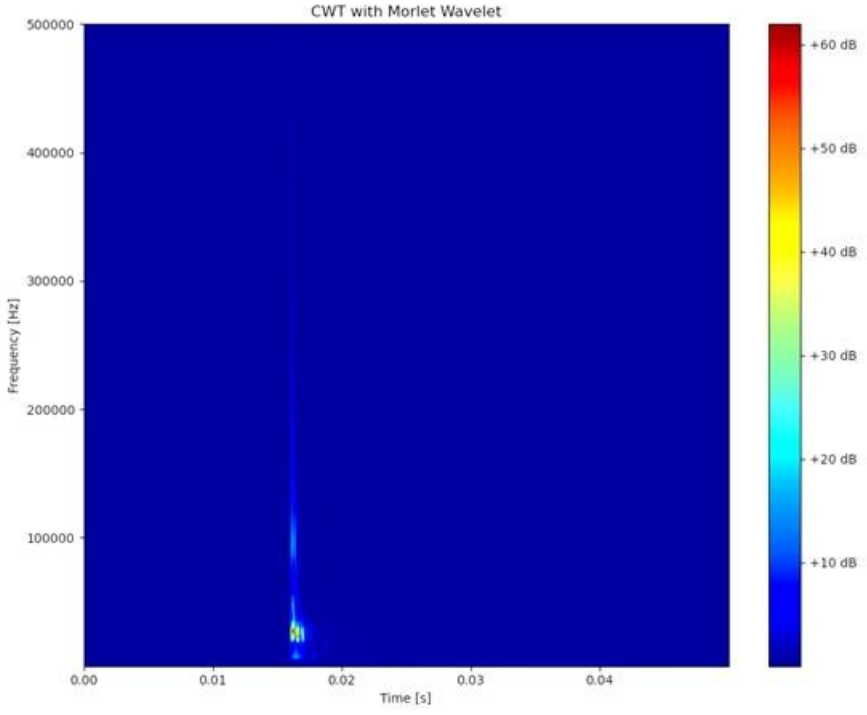

(b)

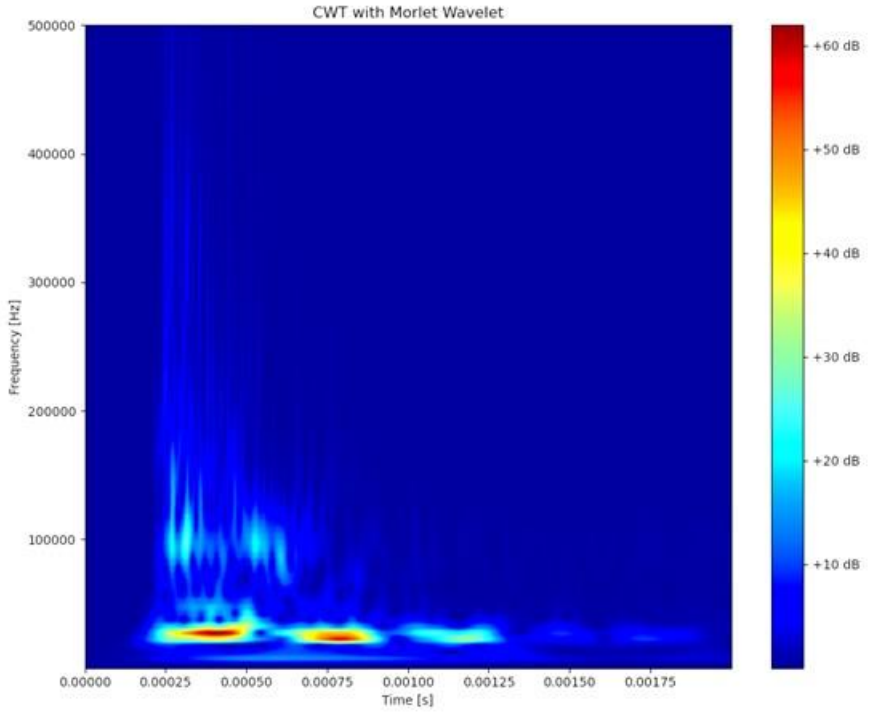

(c)

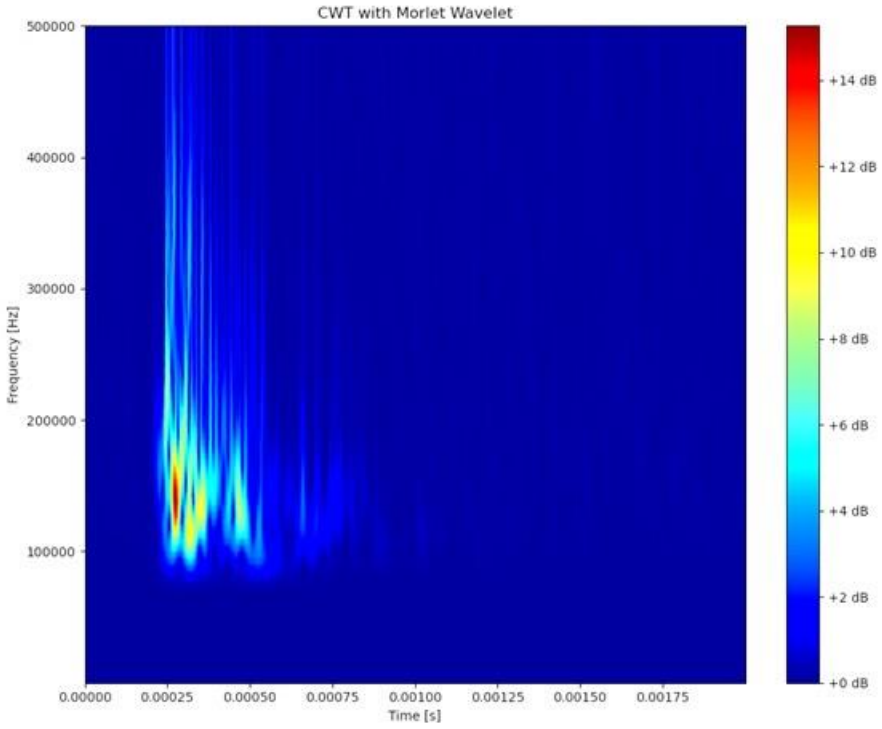

Figure 50 CWT of PLB signal (a) overview (b) 20 kHz filter (c) 100 kHz filter

(a)

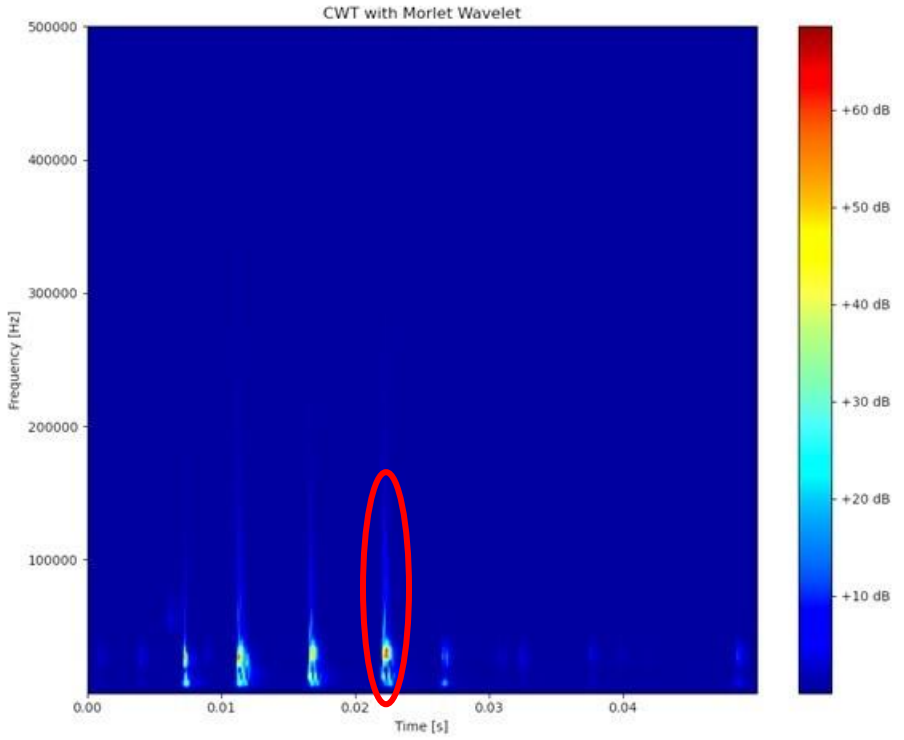
CWT with Morlet Wavelet
500000
400000
300000
200000
100000
Frequency [Hz]
0.00
0.01
0.02
0.03
0.04
Time [s]
+60 dB
+50 dB
+40 dB
+30 dB
+20 dB
+10 dB

(b)

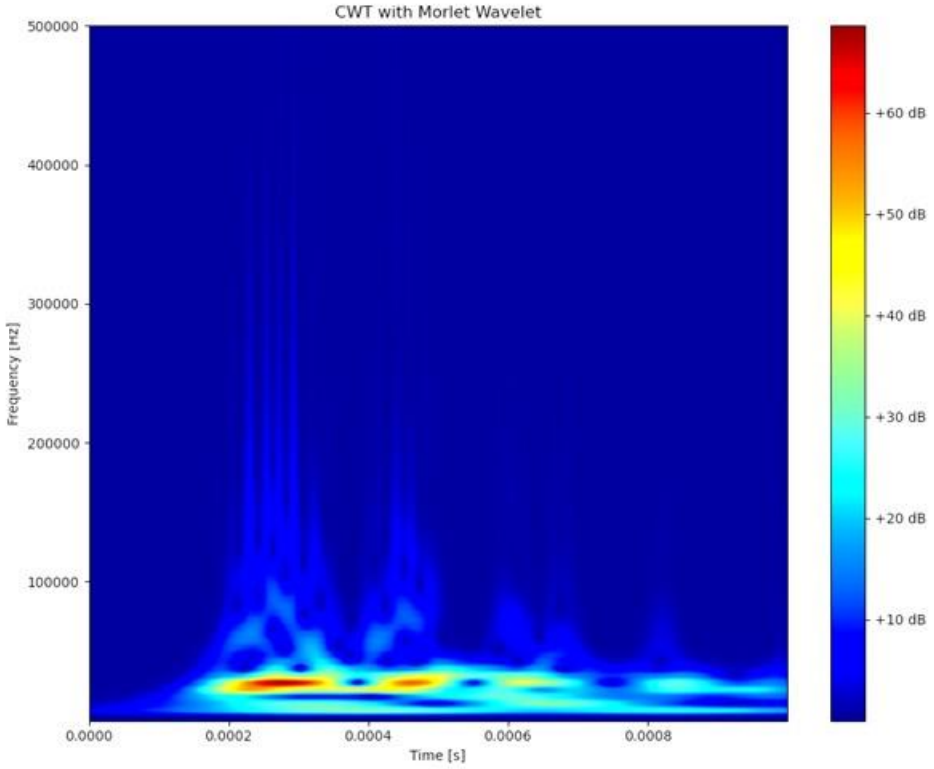
CWT with Morlet Wavelet
500000
400000
300000
200000
100000
Frequency [Hz]
0.0000
0.0002
0.0004
0.0006
0.0008
Time [s]
+60 dB
+50 dB
+40 dB
+30 dB
+20 dB
+10 dB

(c)

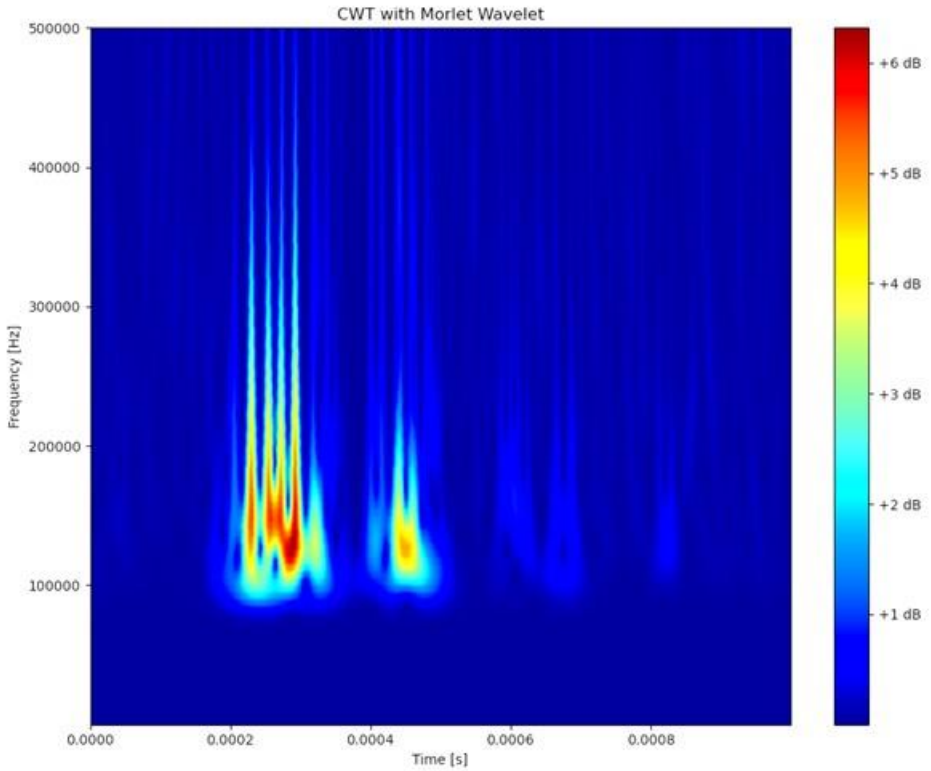

Figure 51 CWT of AE in Nevada (a) overview (b) 20 kHz filter (c) 100 kHz filter

(a)

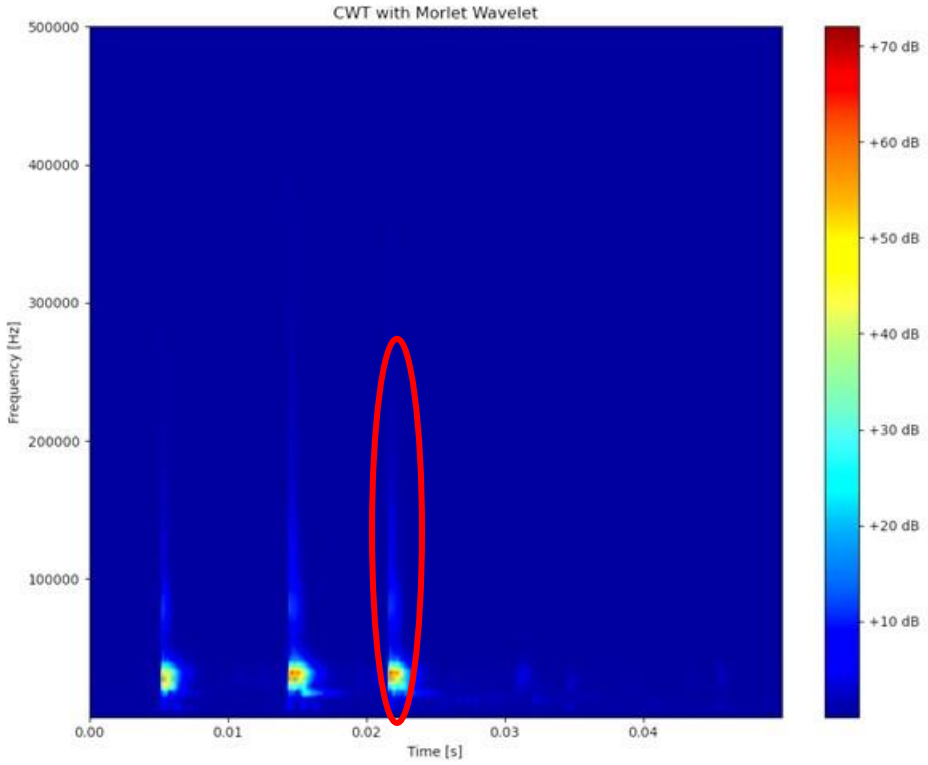

(b)

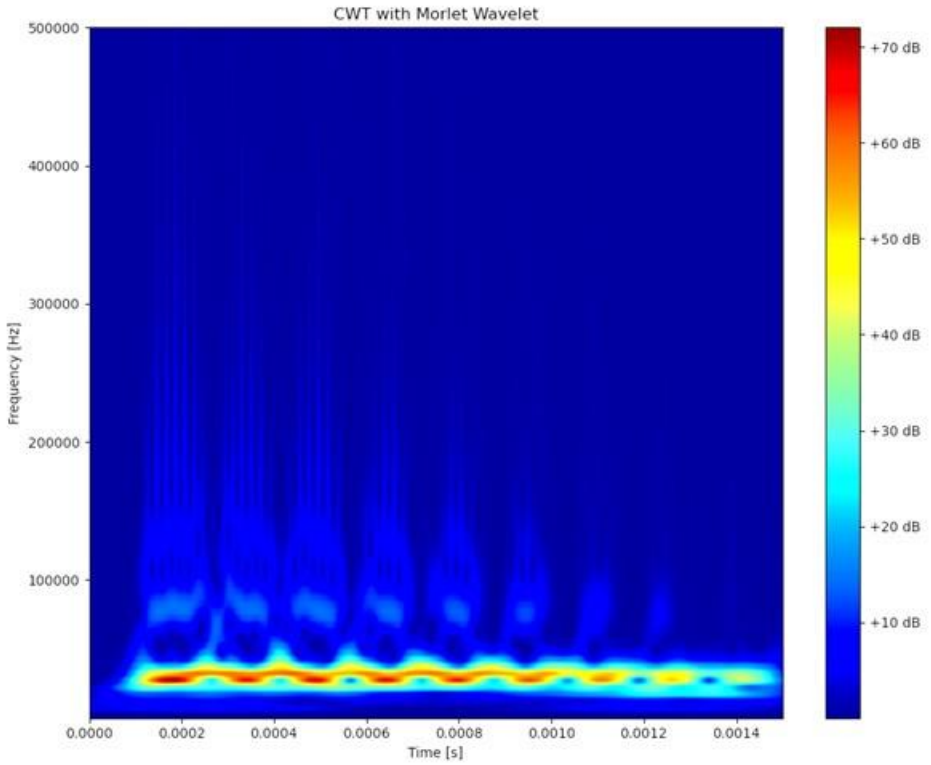

(c)

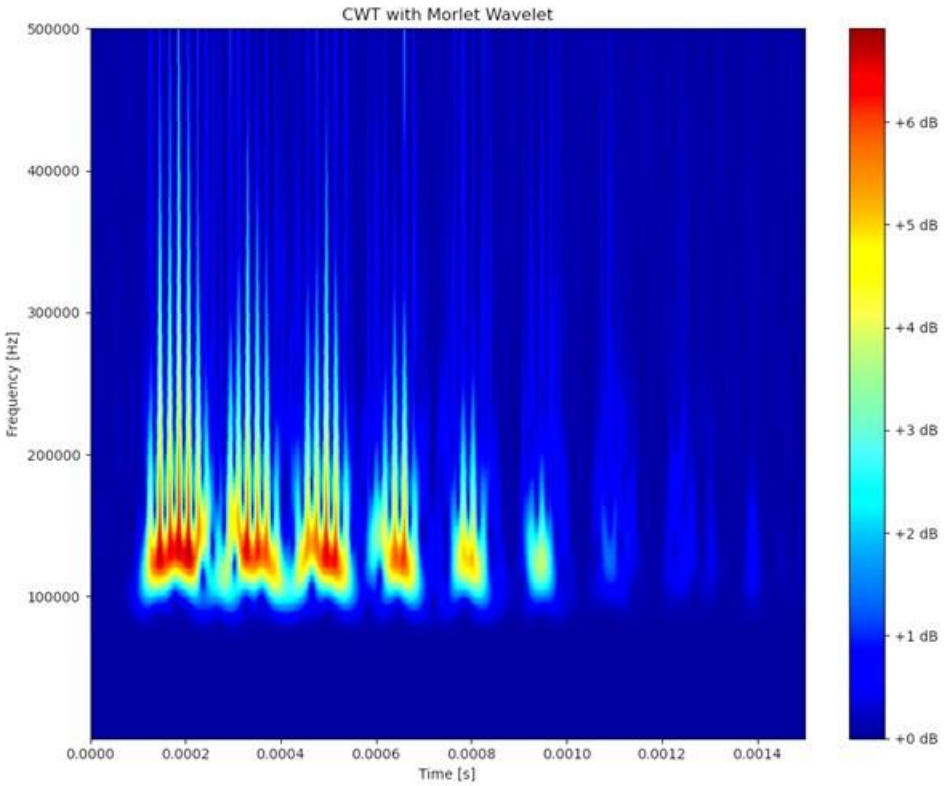

Figure 52 CWT of AE in MxV Rail (a) overview (b) 20 kHz filter (c) 100 kHz filter

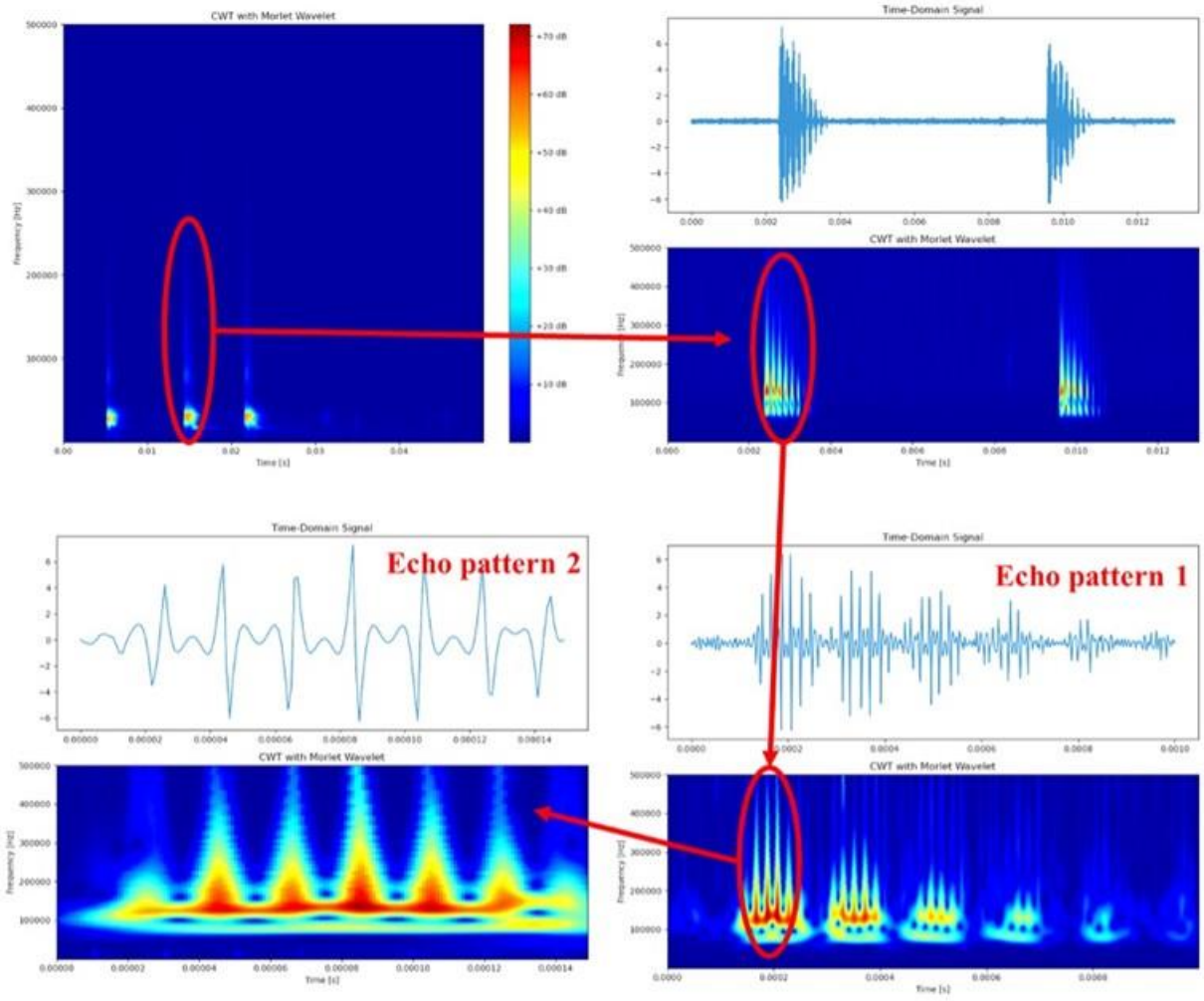

Figure 53 Echo patterns in two time scales

Further investigation is required to fully understand the mechanisms behind these repetitive patterns and their correlation with defect size and the energy release process during defect growth. One hypothesis suggests that the first observed pattern (pattern 1) may result from multiple energy releases associated with incremental crack growth. However, it is more likely that these patterns are related to AE signals within the rail structure. No specific boundaries or discontinuities have been identified that would align with the calculated distances based on the sound velocity in steel rails and the observed time intervals (approximately 2×10^{-4} seconds).

The second pattern (pattern 2) may be attributed to internal reflections within the rail head, leading to constructive interference and superposition of reflected waves. These initial hypotheses provide a basis for future research to clarify the relationship between these repetitive patterns and the physical characteristics of defects, including their size and progression in rail systems.

4.6.2 Propagation Characteristics of AE Waves

The lab and field tests were conducted at various distances between the sensor and the rail surface in two scenarios, each with a distinct research objective. The first setup aimed at evaluating the AE signal attenuation characteristics in the steel rail at different propagation distances, while the second section focused on evaluating the AE signal attenuation after propagating into the air.
Based on the plot in Figure 54 (a), the amplitude attenuation of PLB signals in the rail for the first testing scenario is analyzed, as shown in Figure 54 (b). This figure illustrates the signal attenuation in the rail with low and high-frequency filters. The blue bars represent the amplitudes of the PLB signals filtered with the original 20 kHz high-pass filter, while the green bars show the signals filtered with a 100 kHz high-pass filter. The black I-shaped markers denote the maximum and minimum amplitude ranges. The amplitude of the 20 kHz filter ranges from 4.17V to 1.46V, while the amplitude of the 100 kHz filter ranges from 3.43V to 0.41V. The data highlights that the amplitude attenuation behavior differs significantly between the two filtering scenarios. Specifically, the amplitude of signals with the 20 kHz filter starts to decline markedly from 2.5 inches. In contrast, the signals with the 100 kHz filter indicate a more rapid attenuation starting at 2 inches because the higher-frequency energy attenuates faster than low-frequency energy. Furthermore, the signals show greater relative fluctuation in amplitude beyond the 2-inch propagation distance. This variability indicates that PLB signals had difficulty maintaining a stable attenuation over long distances. These fluctuations could be due to environmental factors such as rail internal irregularities and signal scattering that significantly affect PLB signals.

(a)

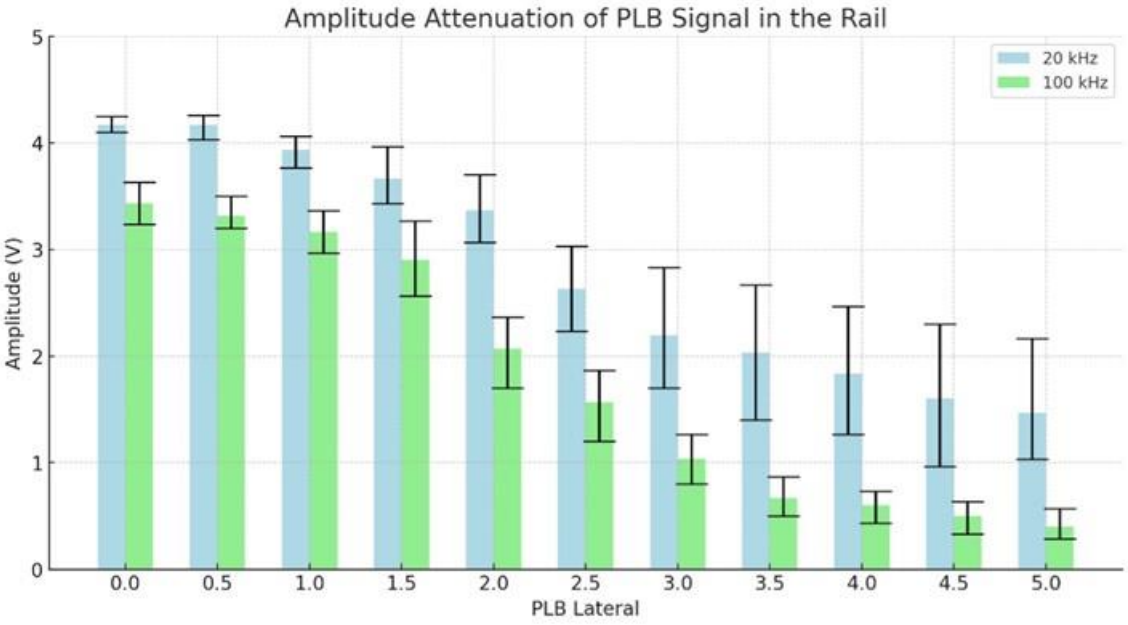

(b)

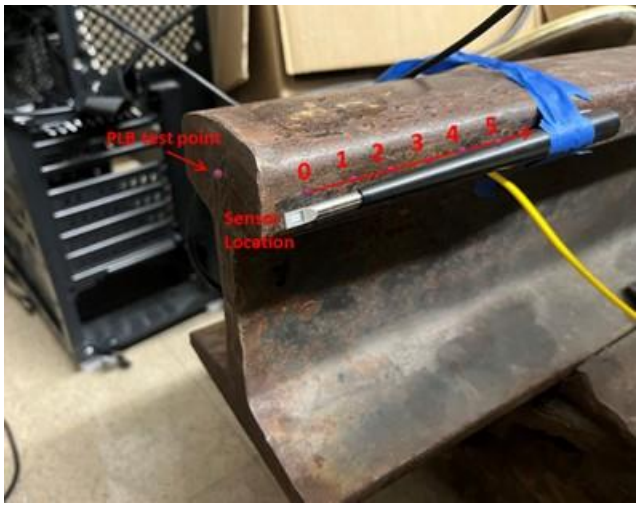

Figure 54 (a) Amplitude attenuation of PLB signal in the rail (b) Test setup

As to the attenuation characteristics in the air, which is shown in Figure 55 (a). It presents the signal attenuation in the air with low and high-frequency filters. The data shows that the amplitude of the 20 kHz filter decreases from 4.25V to 2.88V, whereas the amplitude of the 100 kHz filter drops more dramatically from 3.43V to 0.87V as the distance increases from 0 to 3 inches. This indicates that the higher frequency components (100 kHz) experience more rapid attenuation than the lower frequency components (20 kHz), supporting the previous conclusion. For the 20 kHz filter, a marked decline in amplitude is noted starting around 2.5 inches, suggesting that this filter retains more of the lower frequency energy over shorter distances before attenuating more noticeably. In contrast, the 100 kHz filter shows a rapid decrease in amplitude beginning at 2 inches, highlighting how the higher frequency signals are more susceptible to attenuation in the air. Additionally, both filters have more significant relative amplitude fluctuation beyond the 2-inch distance. This variability suggests that PLB signals struggle to maintain stable attenuation over longer distances in the air.

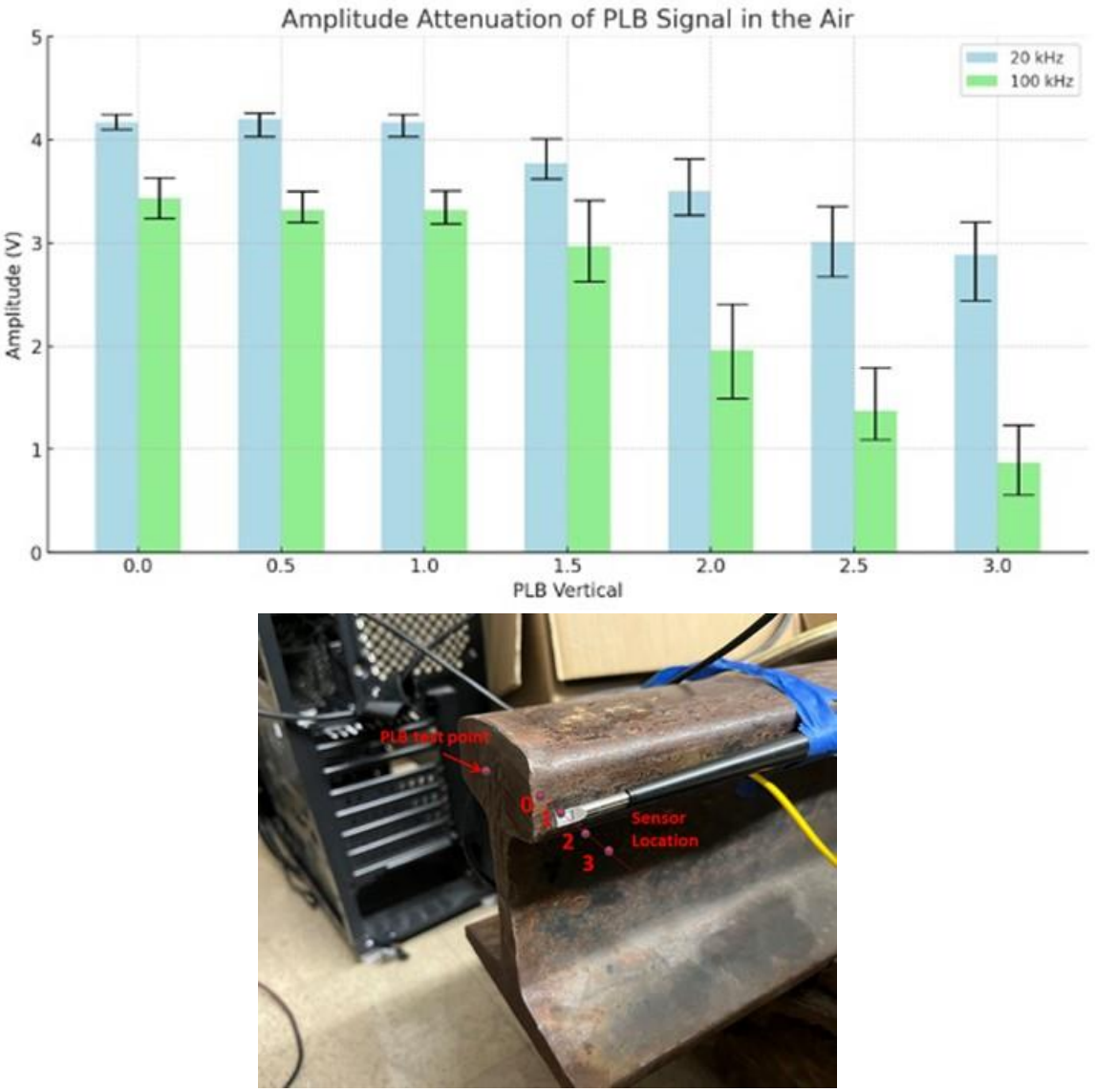

Figure 55 (a) Amplitude attenuation of PLB signal in the air (b) Test setup

The analysis of amplitude attenuation in both the rail and air provides valuable insights into the propagation characteristics of PLB signals, which are critical for optimizing sensor installation in on-vehicle testing scenarios. The findings suggest that to effectively capture high-frequency AE signals effectively, the propagation distance within the rail should stay within 2 inches, and the sensor's proximity to the rail surface should also be maintained within 2 inches. This configuration ensures that the sensor is positioned optimally to detect the high-frequency components of the AE signals, minimizing the impact of attenuation.

Furthermore, the significant attenuation observed with the 100 kHz filter reduces the possibility of mistakenly identifying AE signals from defects located further away on the far side of the rail, which are induced by other wheel-rail impacts. It also enhances the accuracy of defect

identification by ensuring that only signals from sensor-located wheel-rail impacts can be well captured, thereby reducing the likelihood of misidentification.

As to the real-world on-rail test, the amplitude attenuation of AE signals in both the air and the rail indicate the challenges of capturing only useful AE signal data in real-world scenarios compared to controlled laboratory PLB tests (Figure 56 and Figure 57). As stated above, the PLB tests typically demonstrate a clear attenuation of signal amplitude as the distance increases, reflecting a predictable decrease in energy due to propagation losses. However, in real-world field tests, this pattern is not as evident. In the attenuation plot in the rail scenario, it indicates that there is no obvious attenuation of the AE signals, with the amplitudes remaining relatively stable or even slightly increasing. This was caused by the complicated and noisy environment of real-world conditions, where numerous factors such as strong wheel-rail impact noise contribute to signal variability.

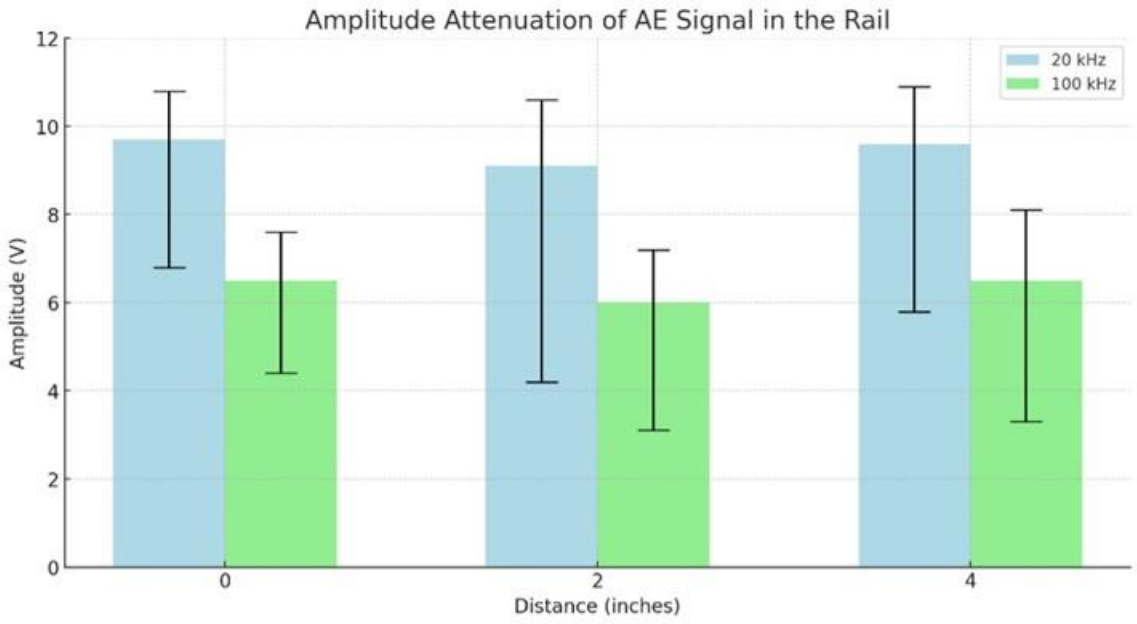

Figure 56 Amplitude Attenuation of AE Signal in the Rail

In the attenuation plot in the air scenario (Figure 57), an abnormal phenomenon is observed where the amplitude of the AE signals increases as the distance from the source increases. This unusual result is likely due to the increased gap between the sensor and the rail surface, which allows the sensor to pick up more mechanical vibrations from the train itself rather than just the intended AE signals. These vibrations, being of high energy and broader in frequency, can lead to unexpected increases in measured amplitude. In some cases, this even caused overflow in the data collected.
The data from both scenarios exhibit significant randomness and fail to present the consistent decreasing pattern of signal attenuation observed in PLB tests. This indicates the impact of ambient noise and mechanical vibrations on the measurements, due to the complexity of real-world field tests. To address these issues in future field tests, it is necessary to properly evaluate the ambient noise level to properly configure the pre-amplifiers and ensure appropriate sensor mounting to

reduce the collection of unrelated ambient noise. This will help reduce the effects of overflow and reduce interference from ambient noise and mechanical vibrations.

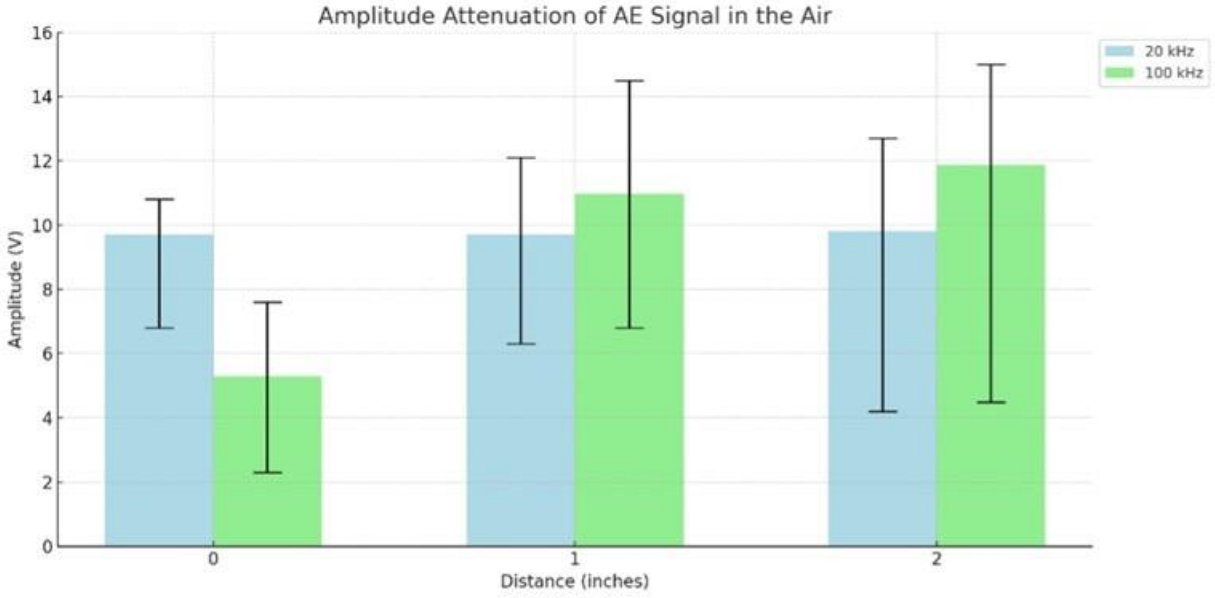

Figure 57 Amplitude Attenuation of AE Signal in the Air

4.6.3 Wavelet Packet Power-based AE Identification

Wavelet Power is a method used to analyze the energy distribution of signals across different frequency bands by decomposing the signal into components at various scales (Dehghan Niri & Salamone, 2012). The wavelet transform provides a time-frequency representation of a signal, allowing detailed analysis of transient and non-stationary phenomena. However, a limitation of the standard wavelet transform is its unequal frequency resolution: it offers good time resolution and poor frequency resolution at high frequencies, and good frequency resolution with poor time resolution at low frequencies. This characteristic is due to the nature of the wavelet transform's multiresolution approach, where only approximation coefficients (lower frequency components) are further decomposed at each level. In general, for a signal $x(t)$, the wavelet coefficients at scale j and position k are given by:

$$W(j,k) = \int x(t)\,\psi_{j,k}(t)dt \tag{11}$$

where $\psi_{j,k}$is the wavelet function scaled by j and translated by k. The wavelet power at each scale can be represented as:

$$P_j = |W(j)|^2 \tag{12}$$

However, this traditional approach does not maintain consistent resolution across all frequency bands. To overcome the limitations of the wavelet transform, the Wavelet Packet Transform (WPT) was developed. Unlike the traditional wavelet transform, WPT decomposes both approximation

and detail coefficients at each level, resulting in a more uniform resolution across all frequency scales. This means that WPT provides enhanced frequency resolution even at higher frequencies, making it more suitable for analyzing signals with complex frequency content, such as AE waves. In WPT, the decomposition is performed on both the approximation and detail coefficients using recursive filtering and down sampling, defined as:

$$wp(i+1,2j) = \sum_n h[n] \cdot wp(i,j)[2n] \tag{13}$$

$$wp(i+1,2j+1) = \sum_n g[n] \cdot wp(i,j)[2n] \tag{14}$$

where $h[n]$ and $g[n]$ are the low-pass and high-pass filter coefficients, respectively. This process results in a full binary tree structure, where each node represents a frequency band, and the nodes at each level correspond to different scales with consistent resolution. The Wavelet Packet Power (WPP) for each frequency scale i can then be calculated as the squared magnitude of the wavelet packet coefficients:

$$P_{i,j} = | wp(i,j) |^2 \tag{15}$$

To summarize the energy distribution across scales, the maximum WPP for each scale i is expressed as:

$$WPP_i = max\{| wp(i,j) |^2\}, j = 1,2,\dots,M \tag{16}$$

In this chapter, WPT-based power analysis will be utilized to exploit the advantage of uniform frequency resolution across all scales, which is particularly beneficial for accurately capturing and analyzing AE signals. This approach allows for a detailed examination of energy distribution across frequency bands, aiding in the identification and characterization of AE sources with improved precision.

To ensure the data quality in presenting the AE characteristics, all the WPP calculations were performed using the signals collected at 0 inch for all the scenarios. A high-pass filter with a cutoff frequency of 100 kHz was applied to the data to better evaluate the AE characteristics in high-frequency range. As shown in Figure 58, the WPP spectrum and maxima present the typical energy distribution of signals collected from PLB tests. The power spectra indicate that the energy is primarily concentrated within the 100 kHz to 300 kHz frequency range, with three distinct energy peaks around 100-140 kHz, 200 kHz, and 270 kHz. These frequency peaks are consistent across different plots, suggesting common features likely related to the AE characteristics of the PLB signal under the tested lab conditions.

In contrast, the WPP spectra and maxima of the rail defect AE signals present distinct differences in energy distribution and peak ranges. The rail defect AE signals predominantly display energy peaks within the 100 kHz to 160 kHz ranges. Unlike the broader energy distribution in the PLB signals, the rail defect spectra show highly concentrated peaks, reflecting stronger signal components likely associated with the severity of structural defects in the rail. Particularly, the rail defect signals demonstrate significantly higher power levels in the maxima plots, with peaks reaching up to 400, indicating more intense acoustic emissions compared to the PLB tests.

While both PLB and rail defect signals present a common presence of lower frequency components, the rail defect AE signals are characterized by more evident and localized peaks, suggesting more severe energy releases. This difference features the importance of detailed frequency analysis in the 50-150 kHz range for distinguishing between AE sources. The increased power levels and distinct peak patterns in rail defect signals emphasize the potential of using these AE characteristics for effective defect monitoring and diagnosis in rail systems.

(a)

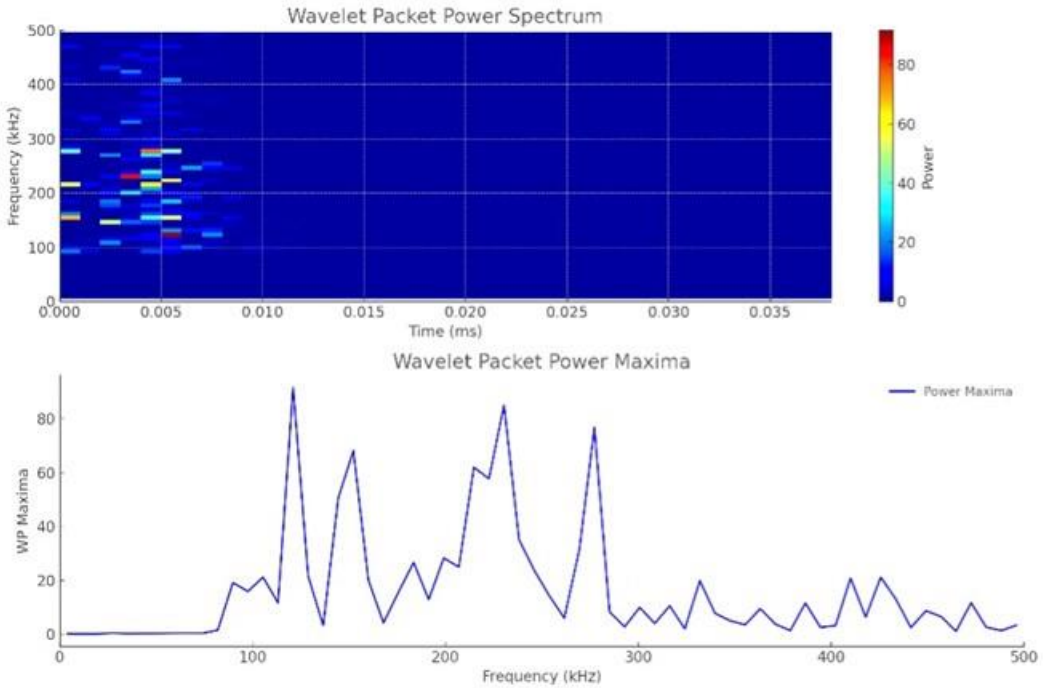

(b)

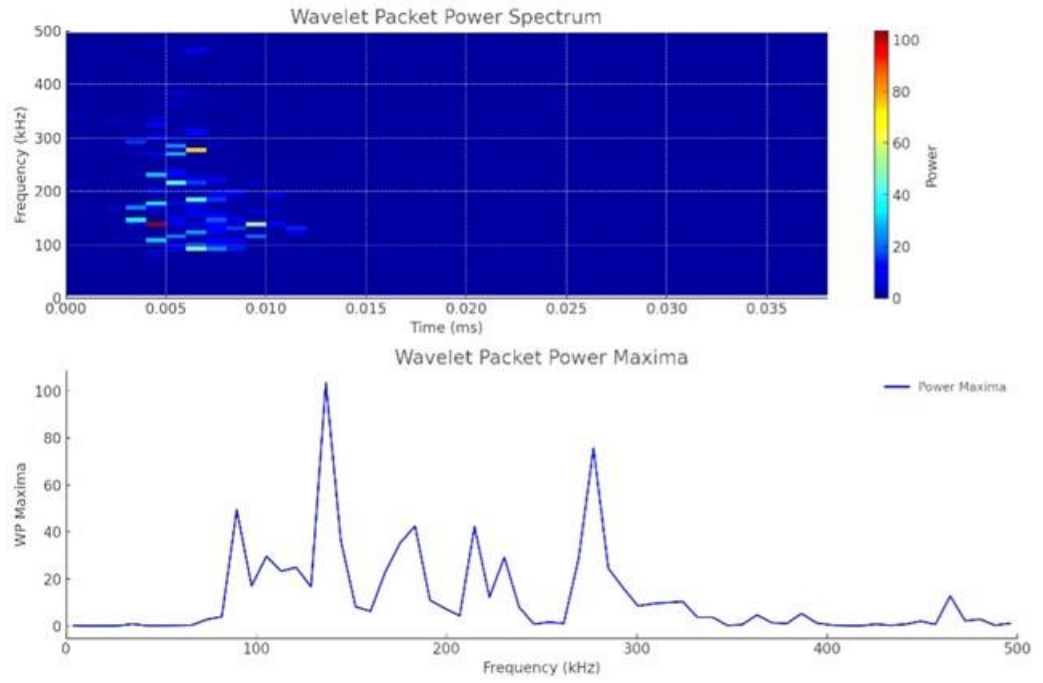

(c)

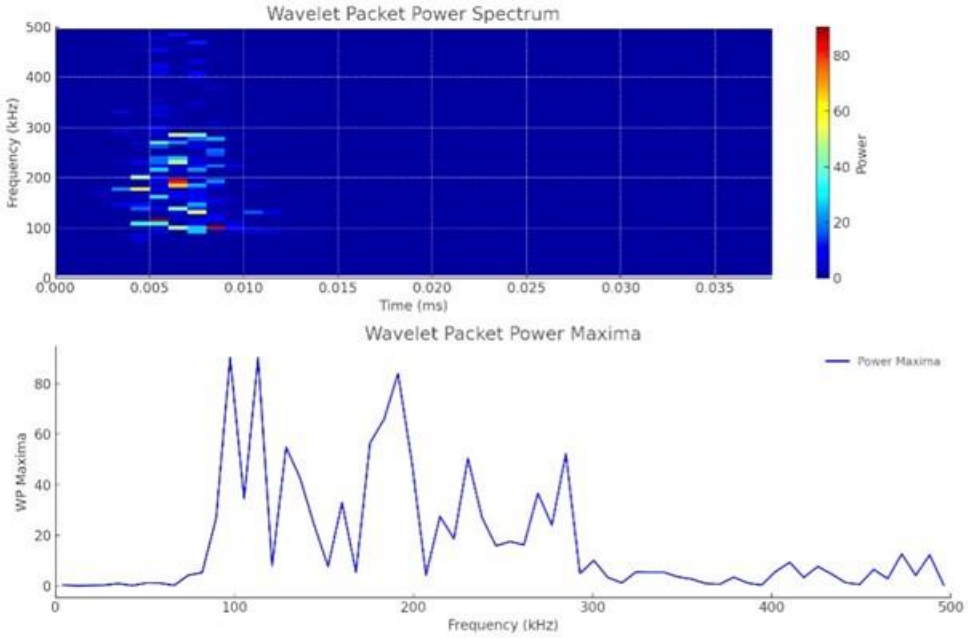

Figure 58 WPP spectrum and maxima of PLB signals

(a)

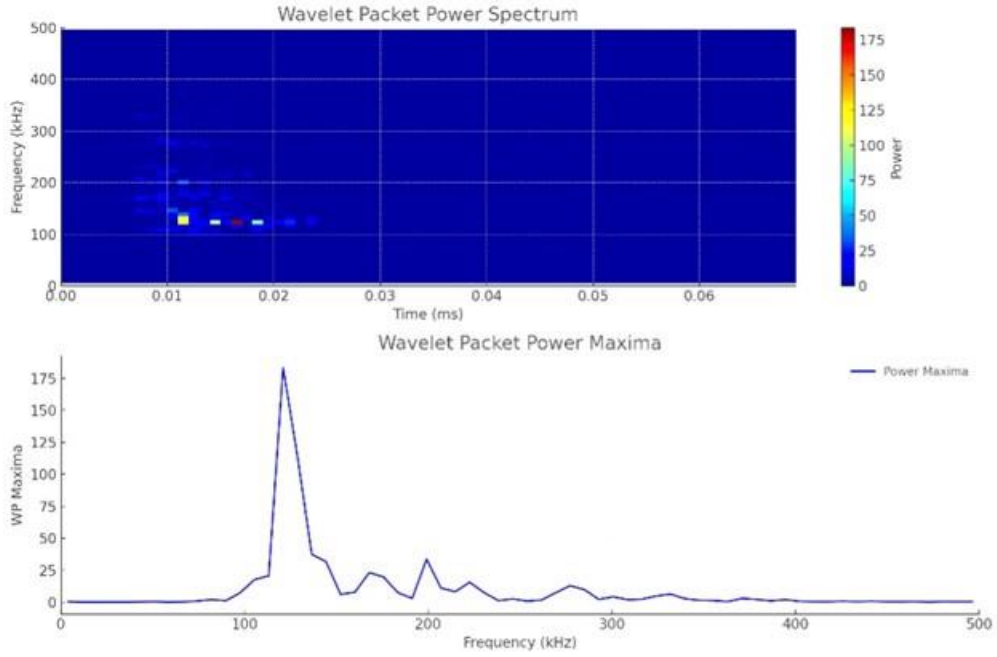

(b)

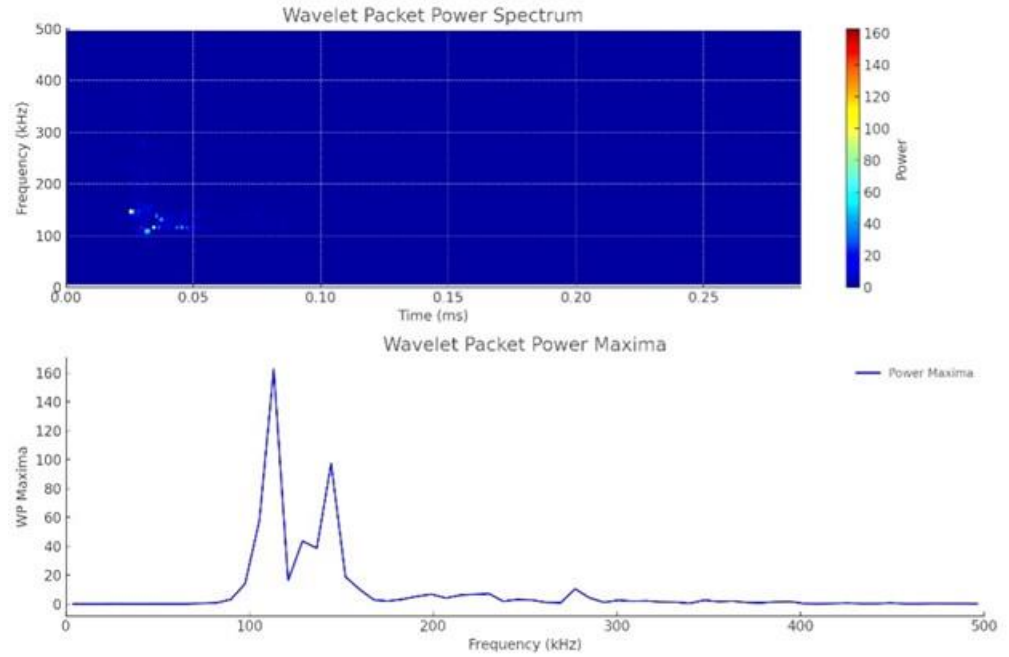

(c)

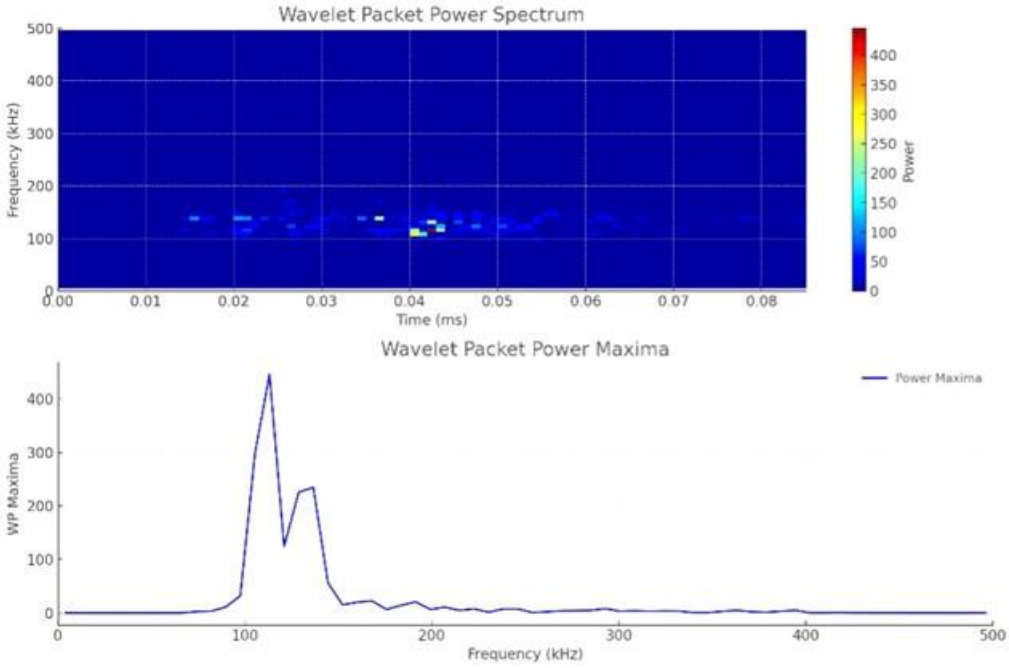

Figure 59 WPP spectrum and maxima of defect-induced AE signals

4.6 Conclusion

This chapter focuses on AE signal detection induced by internal defects. To identify the AE signals and evaluate the propagation characteristics, three techniques are utilized: the time-frequency analysis by CWT, signal amplitude analysis, and WPP analysis, several key conclusions can be drawn regarding the AE characteristics under various test conditions:

Time-frequency representation: The time-frequency analysis indicates that both PLB and rail defect signals present frequency components in the high-frequency range. Particularly, the real-world rail defect signals display significant echo patterns at two distinct time scales, which are not observed in the PLB tests and are less prevalent in the Nevada field tests. Preliminary assumptions suggest that these patterns may be induced by the superposition of internal reflections and multiple energy releases. Therefore, future investigations could focus on understanding the causes of these echo patterns and their potential relationships with crack size and crack growth severity. Evaluating the mechanisms behind these patterns could provide valuable insights and serve as a promising indicator of rail health conditions, aiding in the development of more effective monitoring and diagnostic techniques for rail infrastructure.

AE attenuation characteristics: The analysis of AE attenuation reveals that higher frequency components consistently experience more significant attenuation in PLB tests. The attenuation effect of PLB signals is more pronounced, with rapid decay in amplitude beyond the primary frequency peaks. This suggests that high-frequency AE components are highly susceptible to energy loss over distance and through material barriers. However, due to the complex and noisy environment of real-world scenarios, increased mechanical vibrations and environmental noise, reduced and even diminished such patterns observed in controlled tests. Understanding these attenuation characteristics is critical for accurately evaluating AE signals in field applications. This features the importance of proper pre-amplifier settings and sensor mounting to mitigate overflow and reduce interference, thereby ensuring reliable detection and analysis of AE signals.

Wavelet Packet Power Analysis: The WPP analysis effectively captures the detailed energy distribution of AE signals, emphasizing the dominant frequency components and their relative power levels. The PLB signals show a more distributed energy spectrum with moderate power across a wider frequency range, aligning with their typical AE characteristics under test conditions. Conversely, rail defect signals exhibit significantly higher power concentrations, particularly in the lower frequency bands, with maxima reaching values far exceeding those of PLB tests. Such sensitive power level in rail defect AE signals underscores the increased severity and intensity of acoustic emissions associated with structural flaws, highlighting the diagnostic potential of WPP analysis in detecting and evaluating defect severity.

Implications for AE Monitoring and Diagnostics: The combined analyses demonstrate that AE signals from different sources, such as PLB tests and rail defects, can be effectively distinguished based on their frequency content, attenuation behavior, and power distribution. The significant differences in AE characteristics between the two scenarios suggest that monitoring systems can be optimized to focus on specific frequency bands and attenuation status to enhance defect detection capabilities. The findings also emphasize the importance of high-frequency range analysis, facilitated by high-pass filtering, to capture critical AE details that are indicative of defect presence and severity.

Overall, the integration of time-frequency analysis, AE attenuation evaluation, and WPP analysis provides a robust framework for characterizing AE signals and enhancing the understanding of their underlying sources. These insights are valuable for improving AE-based monitoring and diagnostic strategies in structural health assessments, particularly in applications involving critical infrastructure such as rail systems.

CHAPTER 5 RAIL EXTERNAL DEFECT DETECTION USING AIR-COUPLED SENSORS

The propagation of AE signals from defects within rail structures is generally affected by the defect type (internal or external) and the associated wave modes generated (M. Li et al., 2021). External defects, such as surface cracks, primarily generate surface waves, including Rayleigh waves, which travel along the surface of the rail. These surface waves directly leak into the air and are detected by air-coupled sensors near the rail surface. However, internal defects such as those within the rail's bulk material typically generate longitudinal waves. As these waves propagate towards the surface, they transform into surface waves, such as leaky Rayleigh waves, when they reach the rail-air interface. This conversion process allows the energy from internal defects to eventually leak into the air, where the sensor can capture it. Transforming from longitudinal to surface waves and then into the air adds complexity to the detection process, often resulting in signal attenuation and altered wave characteristics compared to signals originating from external defects. Understanding these distinct propagation mechanisms is not just essential but key to optimizing sensor placement and improving the detection of AE signals from both internal and external defects. Investigating the effects of sensor setup on signal detection will enhance the accuracy and reliability of AE-based rail defect detection systems.

5.1 Rail External Defect Detection in Nevada

5.1.1 Rail-Mounted Field Test

Two external defects were utilized in this test, and the locations were as presented in Figure 60. The details of the defects were measured by visual inspection, as presented in
Figure 61. The sensor head was mounted near the rail head. Two testing scenarios were evaluated in this test, which were the same as previous chapter: 1) the sensor was moved vertically away from the railhead and 2) the sensor was moved horizontally down from the railhead. The first case adjusted the sensor placement in three different locations as shown in
Figure 62 (a) by moving it away from the defect by one inch in the subsequent test. The second case adjusted the sensor placement in three different locations as shown in
Figure 62 (b) by moving it left by two inches in the subsequent test.

The field test configuration was the same as in Chapter 4.4.1; an unloaded hopper car with an axle load of approximately 70,000 lb. was employed. The tests were conducted at 5 mph. A GoPro camera was installed near these defect sites to record when the wheel passed over the defects. A hammer hit was used to synchronize the timeline between the video and the signals, allowing accurate synchronization of video and AE signal timestamps and ensuring a detailed analysis of AE events and associated noises.

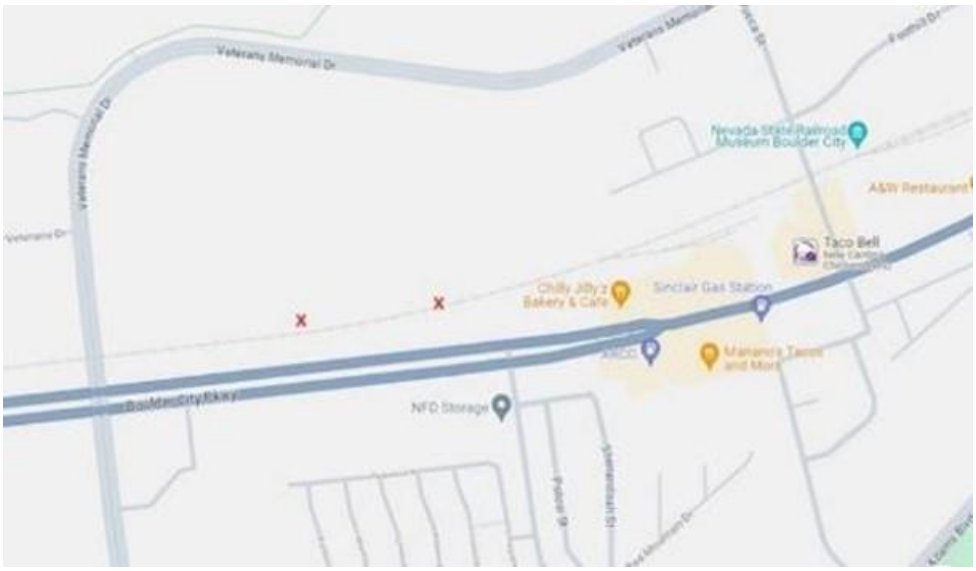

Figure 60 Location of two external defects in the Nevada Railroad Museum

Surface defect: 1.3 in * 0.7 in

Surface defect: 1.2 in * 0.5 in

Figure 61 External defect location and size

(a)

(b)

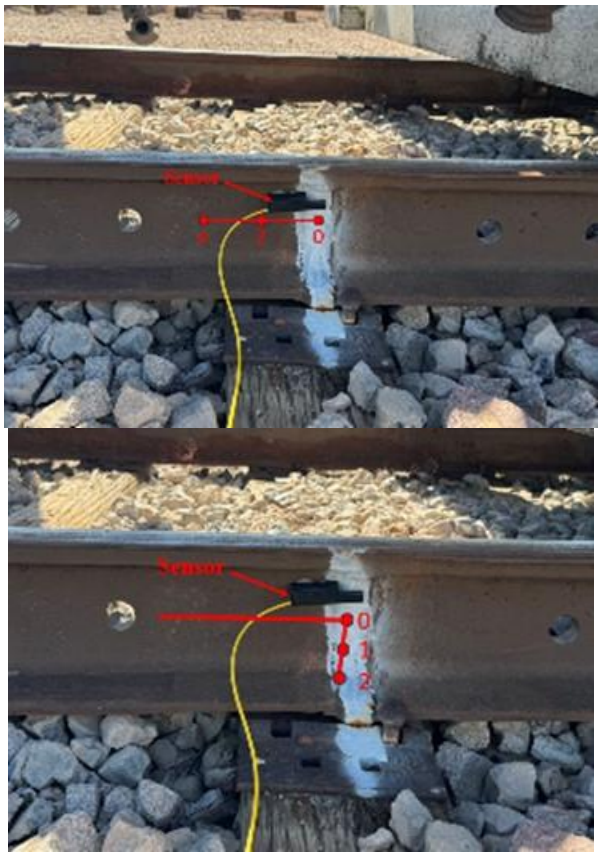

Figure 62 Attenuation evaluation a) vertically in the air b) longitudinally in the rail

5.1.2 Vehicle-Mounted Field Test

In this testing scenario, the sensor was installed the same way as previous on-vehicle tests. It was installed on the train's mounting frame, and the acoustic signals were recorded when the train was running over defects (Figure 63). The sensor was designated to be safely placed 1.5 inches away from the rail head side. As in previous tests, the sensor was relocated from its original position to the far side of the defect by moving it from 0 to 4 inches at two inches increment (Figure 64Figure 49).

Figure 63 Mounting frame (front and side views)

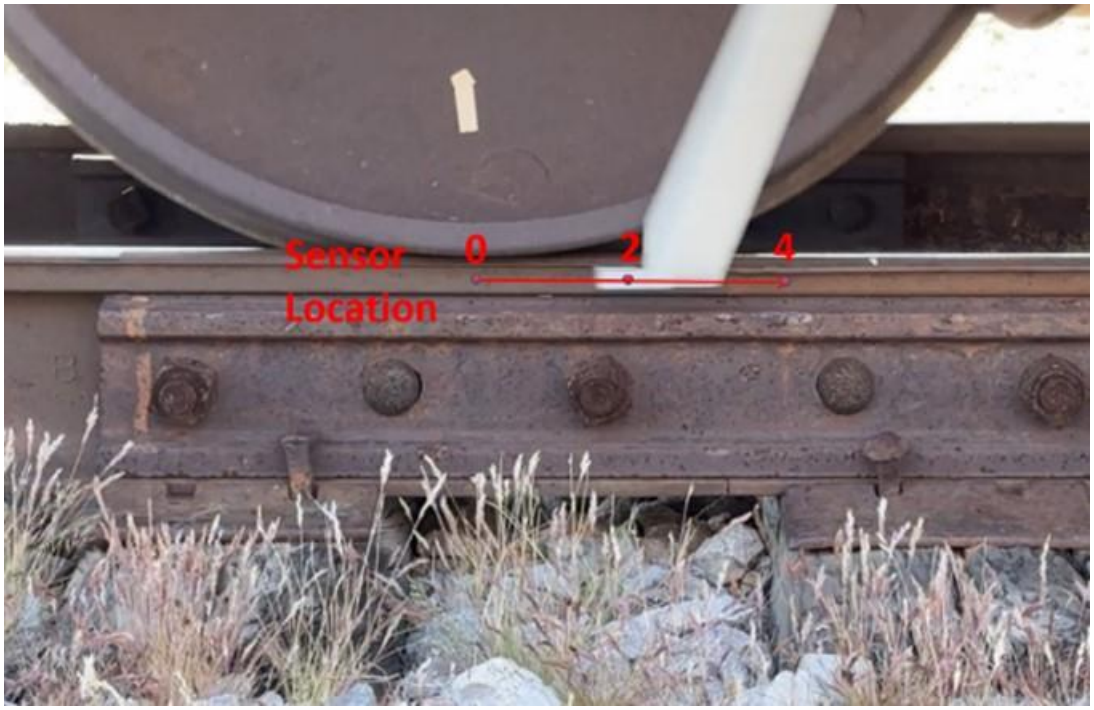

Figure 64 Attenuation evaluation in the rail (longitudinally)

5.2 Rail External Defect Detection in MxVRail

The tests conducted above provided valuable preliminary investigation on external defect detection. However, it was still necessary to conduct further evaluation in MxVRail for external defect detection, since the external defects in the museum were identified by vision only, no professional evaluation was provided by the museum. While this project conducted the tests at the museum, additional field tests were conducted at MxVRail. The tests also include two test scenarios like before: 1) rail mount and 2) vehicle mount.

As stated in the previous chapter, the sensor head had unforeseen damage during the field tests, and the on-rail test for the external defect was canceled. Therefore, only vehicle-mounted tests were conducted.

5.2.1 Vehicle-Mounted Field Test

In this testing scenario, the sensor was installed the same way as the above museum test. It was installed on the train's mounting frame, and the acoustic signals were recorded when the train was running over defects (Figure 65). The sensor was designated to be safely placed 1.5 inches away from the rail head side. As in previous tests, the sensor was relocated from its original position to the far side of the defect by moving it from 0 to 4 inches at two inches increment (Figure 66).

Figure 65 Mounting frame (front and side views)

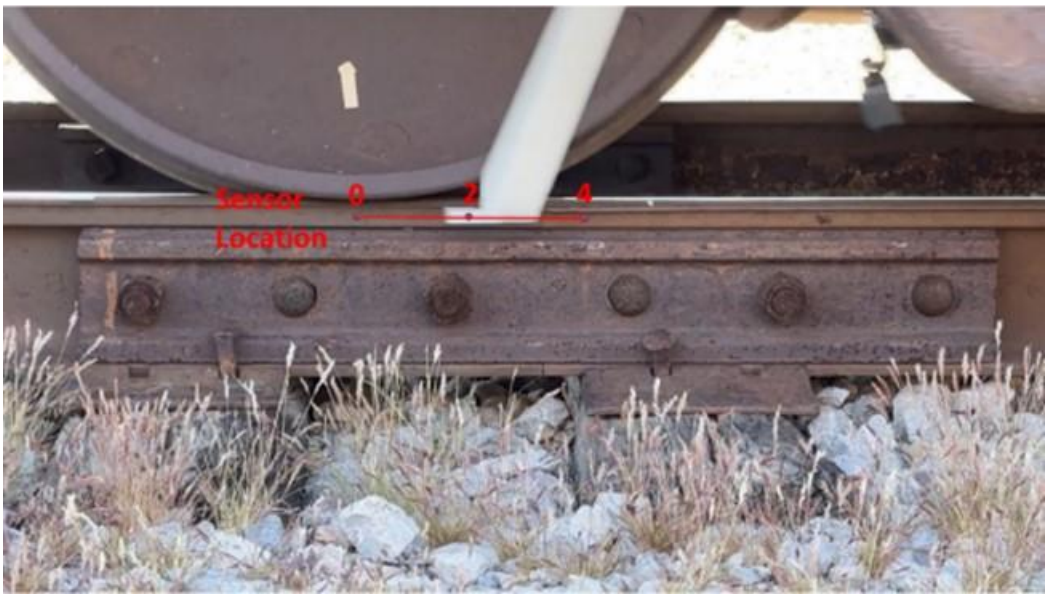

Figure 66 Attenuation evaluation in the rail (longitudinally)

5.3 Results and Discussion

In summary, two different stages of tests were conducted to evaluate the attenuation characteristics and AE signal propagation under various conditions, specifically targeting internal defects in rail structures (Table 7). The first stage involved field tests conducted at the Nevada Railroad Museum, focusing on the initial evaluation of AE signal characteristics in a real-world environment. The sensor was tested in rail-mounted and vehicle-mounted configurations, with offsets of 0, 2, and 4 inches for rail-based measurements and 0, 1, and 2 inches for air-based measurements, each repeated 10 times. The second stage occurred at the MxVRail facility, where further evaluation of AE signal characteristics was performed, based on the findings from the Nevada tests. Similar sensor configurations, with the same offsets and repeat counts, provided a thorough assessment of AE signal behavior in different testing environments. Although all the rail-mounted tests were canceled due to the sensor damage which was explained in the previous chapter, these stages collectively contributed valuable insights into optimizing sensor placement and data collection strategies for non-contact rail health monitoring systems.

Table 7 Summary of External Defect Tests

Test Location	Sensor Location	Attenuation Evaluated	Test Speed (mph)	Offset From Defect	Number of Repeats	Goal
Nevada	Rail-mounted	Rail	5	0, 2, 4	10 for each	Initial evaluation of AE signals
		Air	5	0, 1, 2	10 for each	
	Vehicle-mounted	Rail	5	0, 2, 4	10 for each	

MxVRail	Rail-mounted	Rail	5	0, 2, 4	Canceled	Further evaluation of AE signals
		Air	5	0, 1, 2		
	Vehicle-mounted	Rail	5	0, 2, 4	10 for each	

5.3.1 Time-Frequency Representation of Defect Signals

The AE signals collected from defect areas during real-world field tests were analyzed using CWT. Unfortunately, the CWT analysis of the Nevada field test data did not indicate the presence of AE signals. As shown in Figure 67, the tests predominantly captured low-frequency mechanical vibrations throughout the entire testing period. In the MxVRail field test, only two AE events were detected by the sensor during the examination of external defects, as illustrated in Figure 68 and Figure 69. The observed pattern was consistent with previous observations, with low-frequency components dominating the energy spectrum and a notable energy peak concentrated in the 120-150 kHz range. Several factors could account for these observations. One possibility is that the external defects in Nevada were in stable conditions, making it challenging to detect AE signals associated with active crack growth. Another possibility is that the defect in the MxVRail test was in its very early stages, which hardly producing AE signals. However, additional field tests are necessary to further assess the feasibility of detecting external defects under real-world conditions and to validate the effectiveness of AE signal analysis in these environments.

(a)

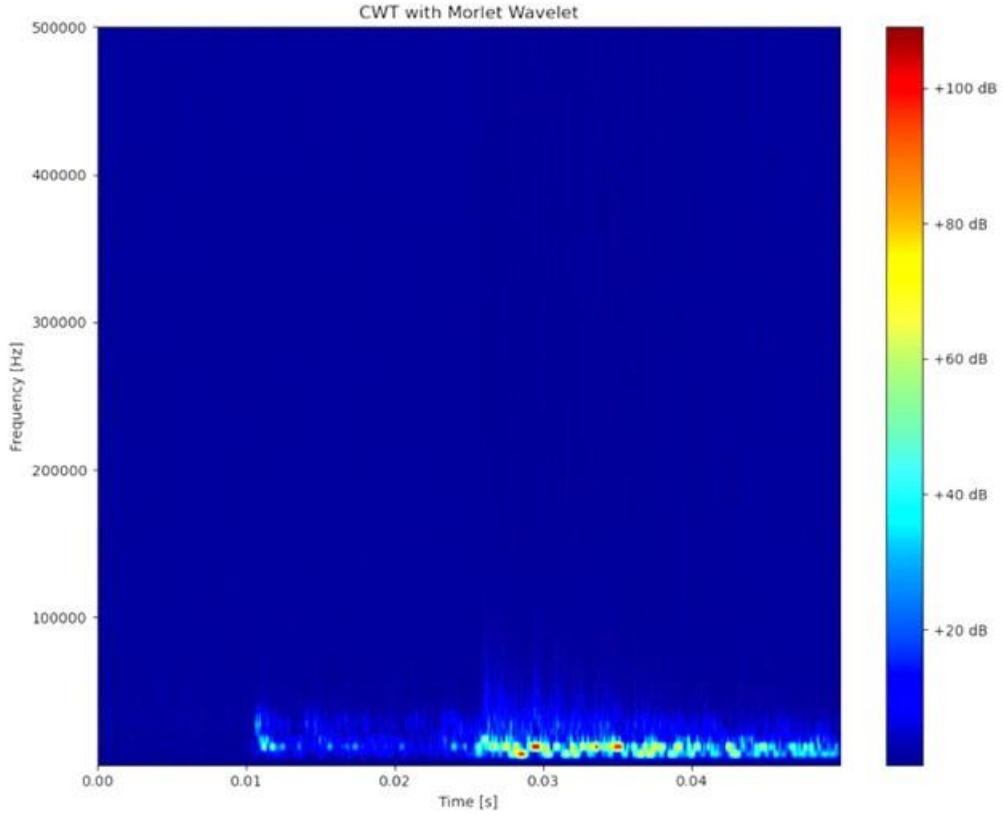

(b)

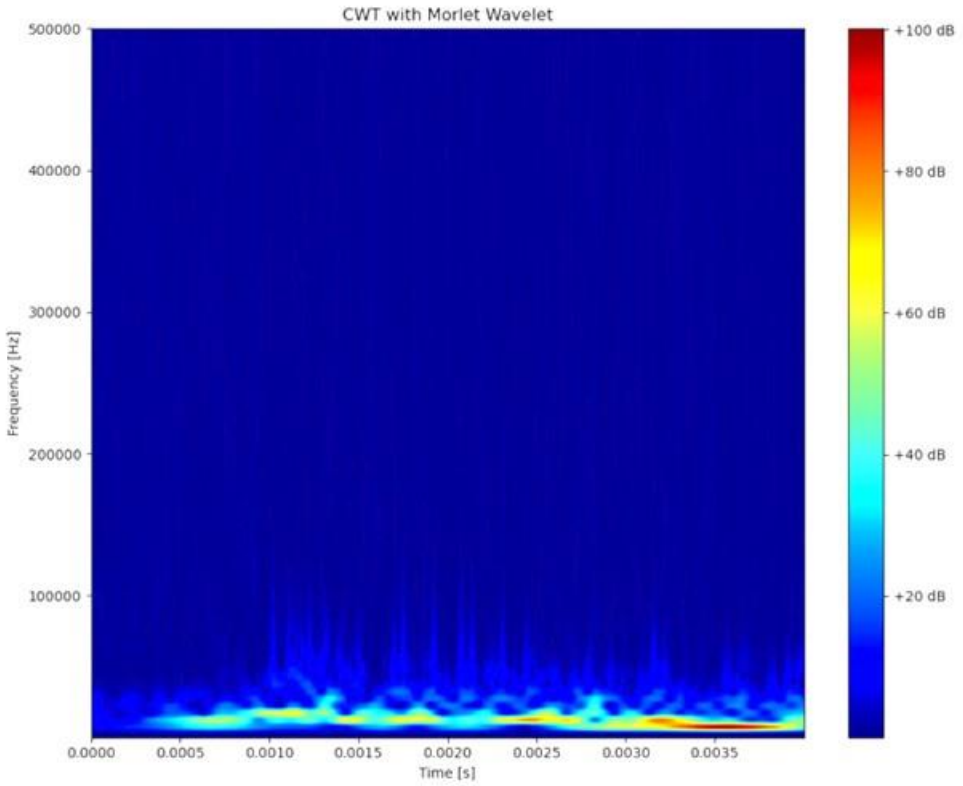

(c)

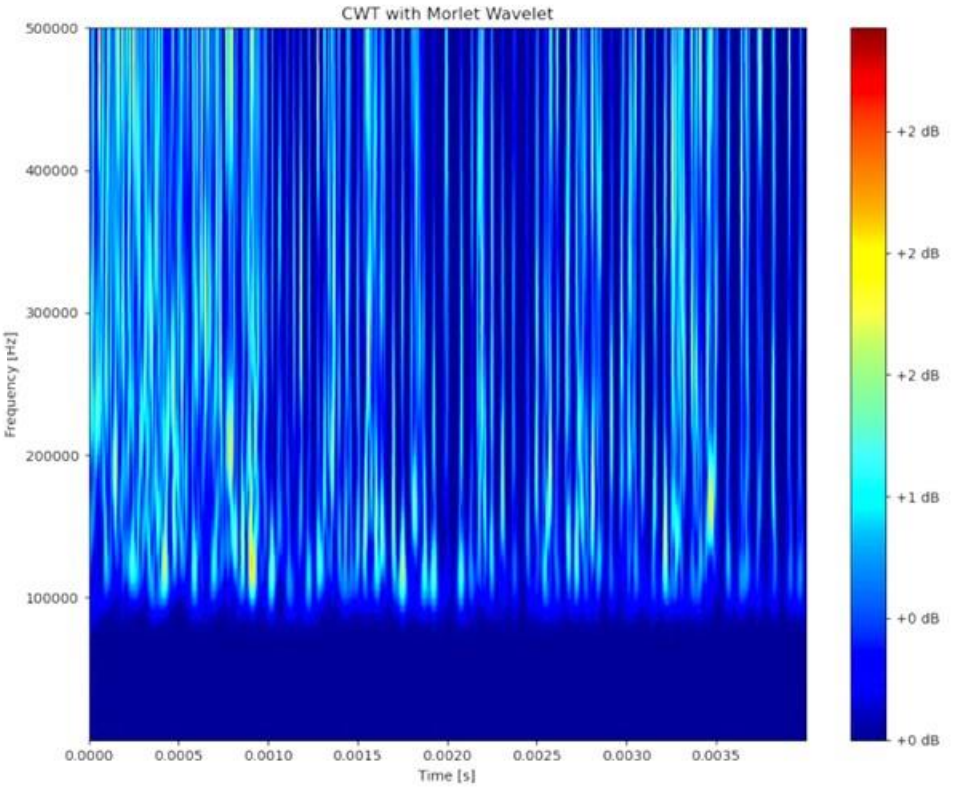

Figure 67 CWT of AE in Nevada (a) overview (b) 20 kHz filter (c) 100 kHz filter

(a)

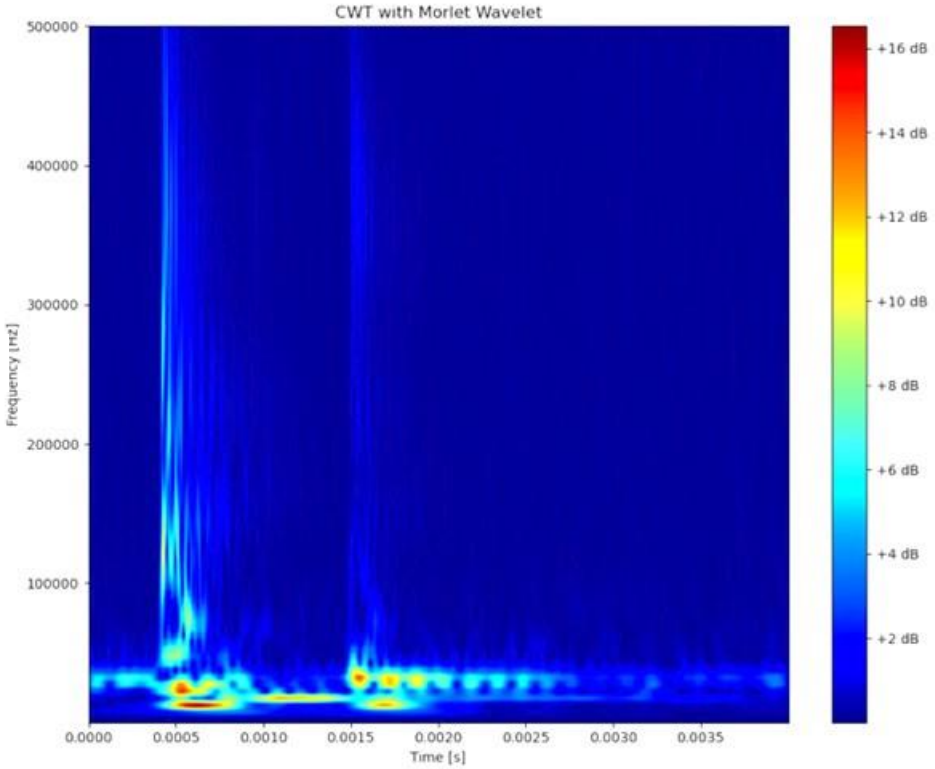
CWT with Morlet Wavelet
Frequency [Hz]
500000
400000
300000
200000
100000
0.0000
0.0005
0.0010
0.0015
0.0020
0.0025
0.0030
0.0035
Time [s]
+16 dB
+14 dB
+12 dB
+10 dB
+8 dB
+6 dB
+4 dB
+2 dB

(b)

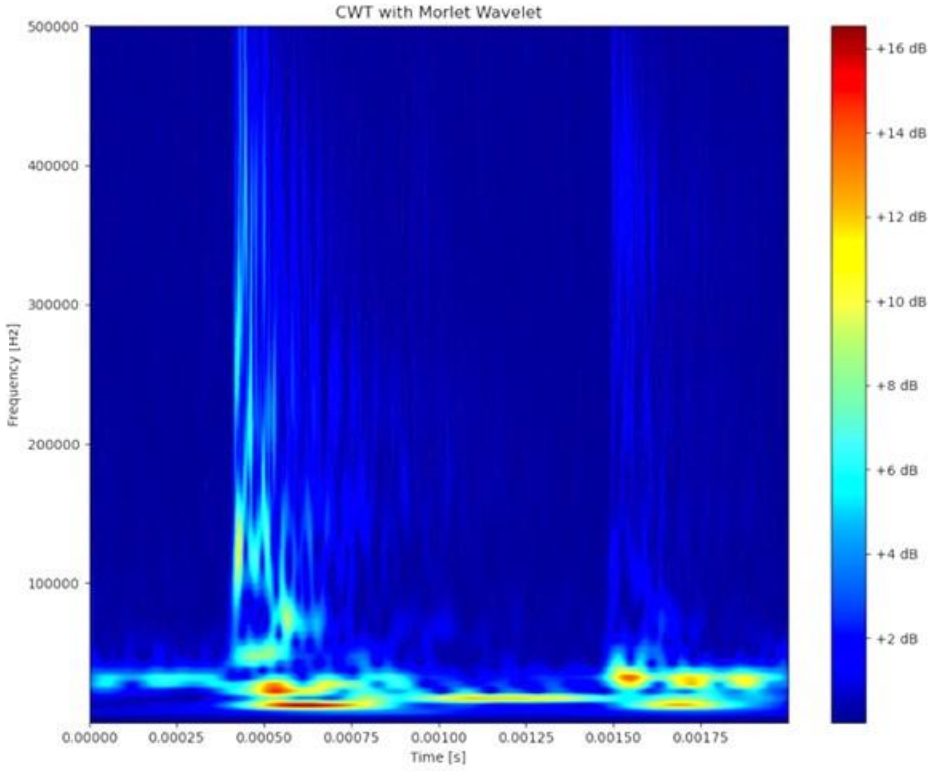
CWT with Morlet Wavelet
Frequency [Hz]
500000
400000
300000
200000
100000
0.00000
0.00025
0.00050
0.00075
0.00100
0.00125
0.00150
0.00175
Time [s]
+16 dB
+14 dB
+12 dB
+10 dB
+8 dB
+6 dB
+4 dB
+2 dB

(c)

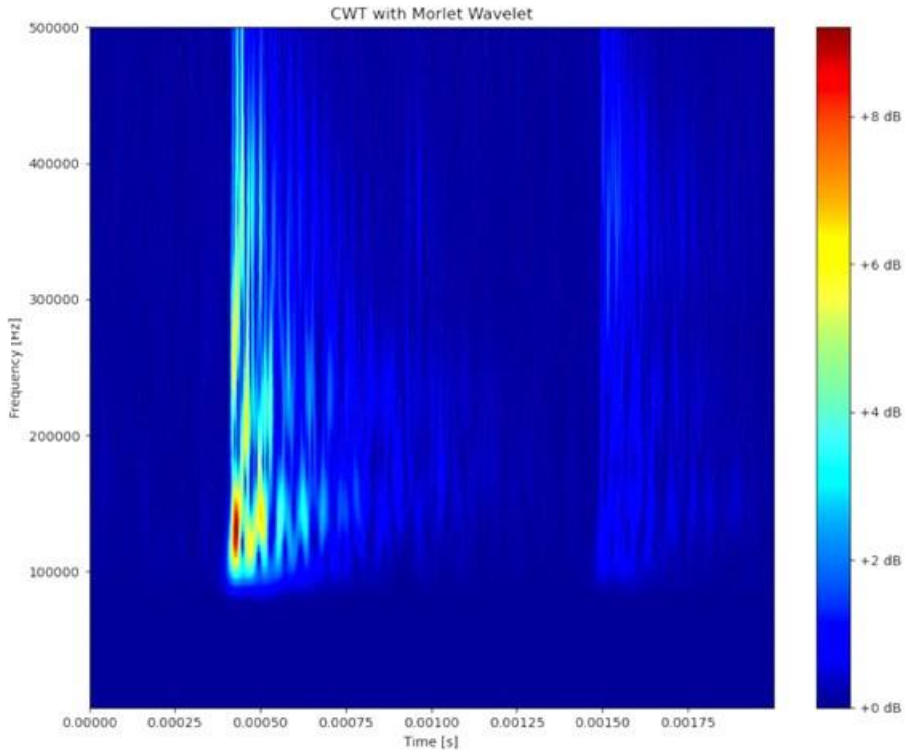

Figure 68 CWT of AE(1) in MxVRail (a) overview (b) 20 kHz filter (c) 100 kHz filter

(a)

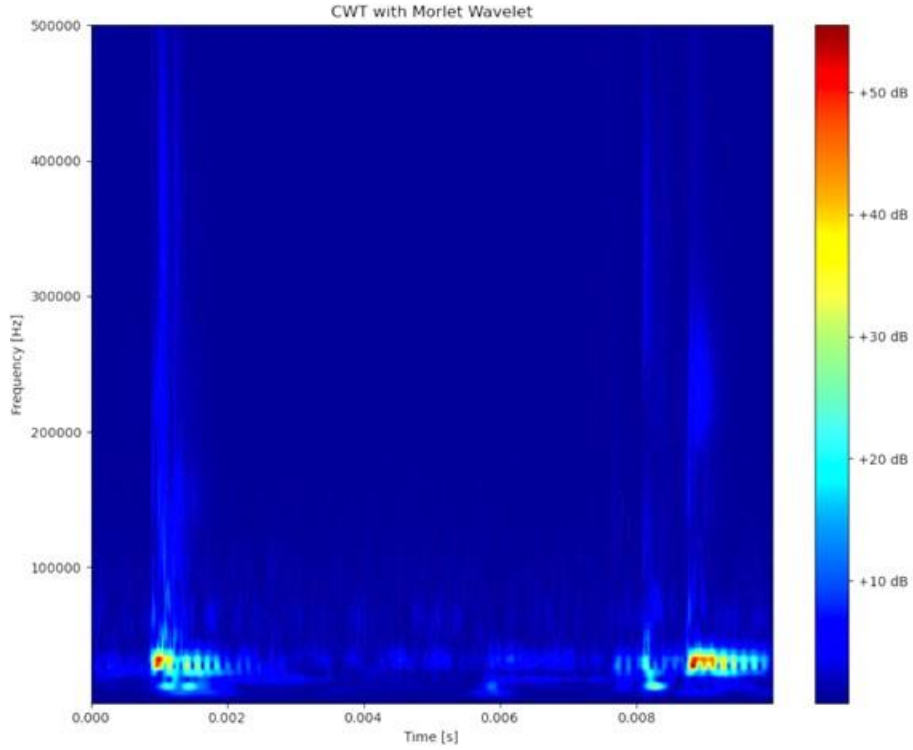

(b)

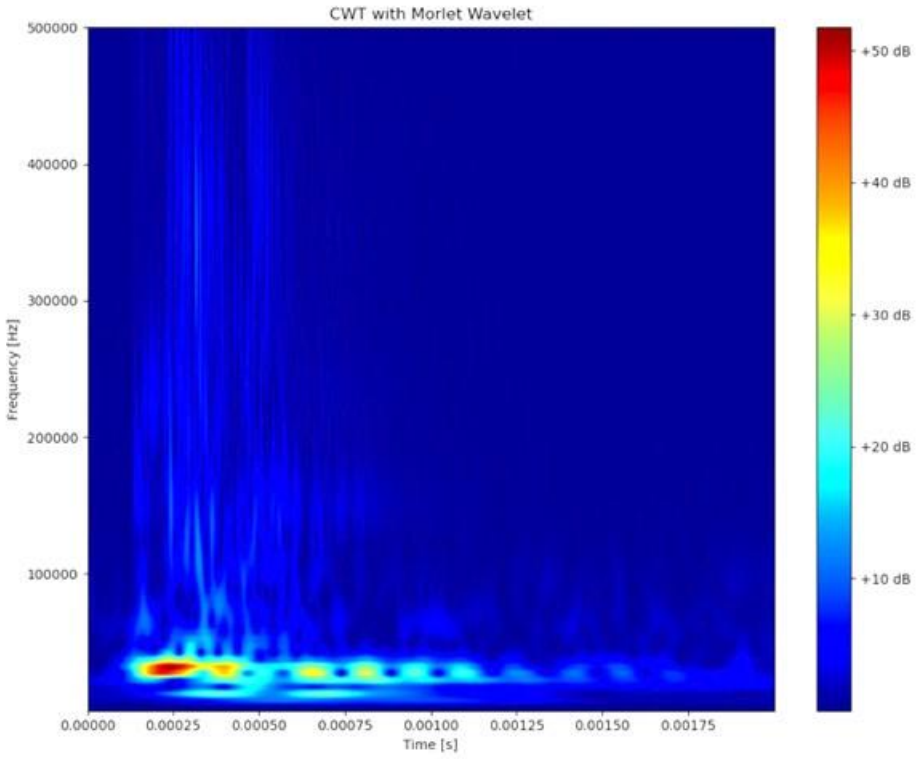

(c)

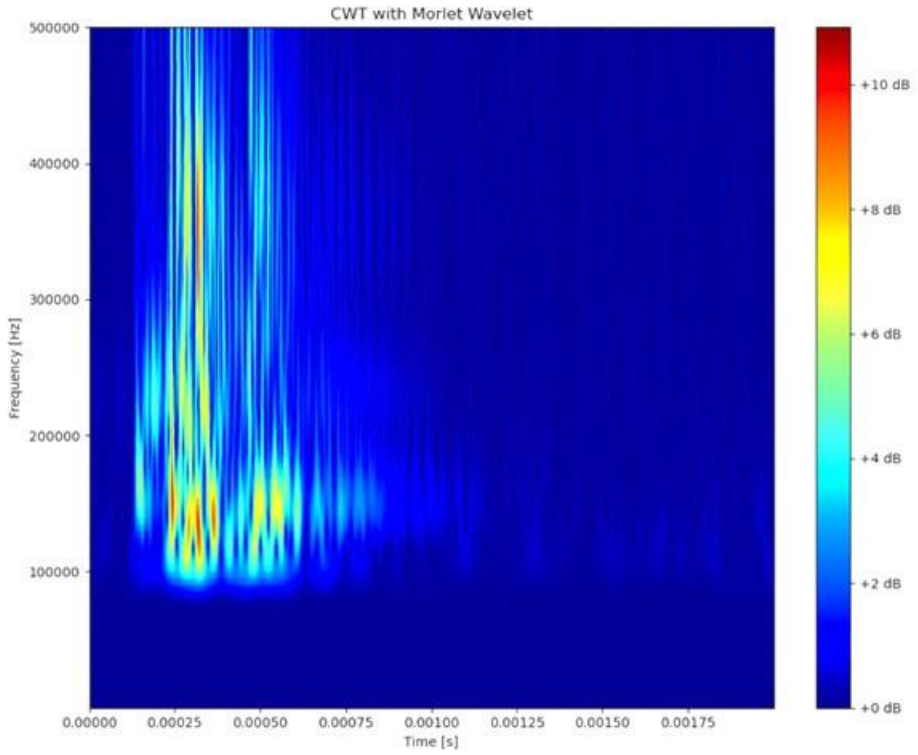

Figure 69 CWT of AE(2) in MxVRail (a) overview (b) 20 kHz filter (c) 100 kHz filter

5.3.2 Wavelet Packet Power-based AE Identification

Although the field tests in this chapter did not detect significant amount of AE signals as previous chapter. It is still necessary to investigate the AE events captured in MxVRail. Based on the introduction of WPT-based power analysis from chapter 4.6.3, the WPP calculations used the two signals collected at 0 inch for the MxVRail surface defects. A high-pass filter with a cutoff frequency of 100 kHz was applied to all the data to better evaluate the AE characteristics in high-frequency range. As shown in Figure 70, the WPP spectrum and maxima present the typical energy distribution of signals collected from field tests. The power spectra indicate that the energy is concentrated within the 100 kHz to 400 kHz frequency range, typically three energy peaks around 100-140 kHz, 200 kHz, 280 kHz, and 360 kHz. These frequency peaks are observed in both plots, suggesting common features likely related to the AE characteristics of the external rail defects.

(a)

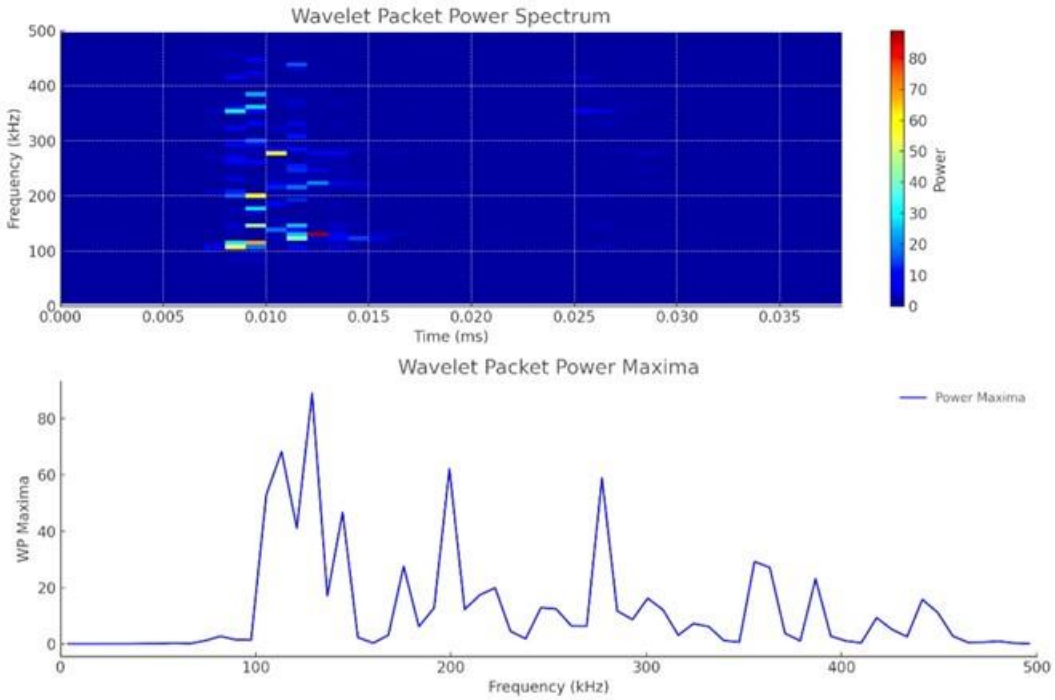

(b)

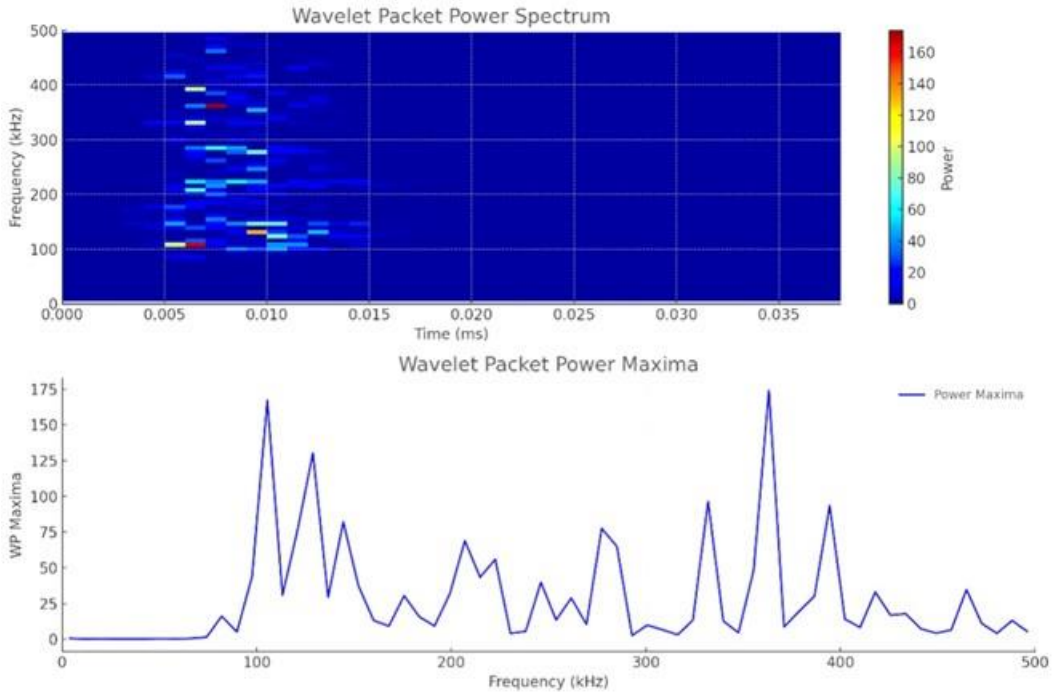

Figure 70 WPP spectrum and maxima of defect-induced AE signals

5.4 Conclusion

This chapter focuses on the detection of AE signals induced by external defects. Due to the limited number of AE events detected, the AE signals and their propagation characteristics were preliminarily assessed using CWT and WPP analysis. Based on the findings, several recommendations for future research are outlined.

External defects typically originate through mechanisms distinct from those of internal cracks, such as wear and fatigue resulting from prolonged service. These defects may not develop in the same manner as internal cracks but are often triggered by specific incidents like severe friction during braking or starting. Furthermore, surface defects tend to be distributed along extensive surface areas rather than being concentrated at a single point, as is common with internal defects. This distribution can complicate defect identification, as AE signals induced by these defects can originate from anywhere within the fatigue and wear zones. This emphasizes the need for advanced algorithms capable of isolating AE events from ambient noise. The insights gained in this chapter are valuable for refining future testing setups and enhancing defect identification algorithms.

CHAPTER 6 RESEARCH SUMMARY

This report aimed to develop an on-vehicle-mounted AE approach for rail health monitoring during operations, investigated the potential of bone-conduct sensor and air-coupled optical microphone for AE signal collection and defect identification. The study focused on three main objectives: 1) exploring on-vehicle AE data collection techniques; 2) evaluating AE signal characteristics in laboratory settings and assessing analysis algorithms for rail defect identification; and 3) assessing the performance of this approach for identifying rail defects in real-world field tests.

Conclusions:

(1) Non-Contact AE Detection:
The research highlights the potential of using air-coupled optical microphones to capture AE signals without direct contact, thereby addressing limitations of traditional bone-conduct sensors which were investigated in the first stage. This non-contact approach is intended to facilitate early-stage rail defect monitoring without disrupting regular train operations.

(2) Lab and Field Evaluations:
AE signal characteristics were evaluated through both controlled lab tests and real-world field tests. The results demonstrated the capability of the proposed method to detect internal defects, although with some limitations due to environmental noise and signal attenuation. However, external defects still need further investigation to validate the detection capability. Additionally, external defects, such as wear and fatigue presented distinct challenges due to their different propagation mechanisms compared to internal defects, necessitating advanced algorithms for noise isolation and defect identification.

(3) CWT and WPP Analyses:
Preliminary evaluations of AE signals using CWT and WPP analysis present that AE signal propagation characteristics vary significantly with defect type and conditions. These methods helped identify typical energy distributions and frequency peaks related to external defects, which are crucial for refining defect detection algorithms.

(4) Challenges and Future Recommendations:
The study encounter challenges in detecting external-induced AE signals due to insufficient events and significant ambient noise. It is recommended that future research focus on enhancing defect identification algorithms and testing setups, particularly for isolating AE events from noise. The study also suggests that defects originating from external sources, such as wear and fatigue, may not follow the same development patterns as internal cracks and may require targeted detection strategies.

(5) Insights for Rail Safety and Maintenance:
This research is expected to contribute significantly to the safety assessment of rail infrastructure, ultimately enhancing rail maintenance efficiency. By advancing non-contact AE technology for real-time rail health monitoring, the study provides valuable insights and lays the groundwork for future developments in automated AE monitoring systems for railway infrastructure

REFERENCES

1. A Teolis, J. B. (2017). Computational Signal Processing with Wavelets. https://doi.org/10.1007/978-3-319-65747-9
2. Astm, E. (2021). 976, Standard Guide for Determining the Reproducibility of Acoustic Emission Sensor Response. ASTM Book of Standards (1993): 03-03. https://doi.org/10.1520/E0976-15R21
3. Bojarczak, P. (2013). Visual algorithms for automatic detection of squat flaws in railway rails. Insight - Non-Destructive Testing and Condition Monitoring, 55(7), 353-359. https://doi.org/10.1784/insi.2012.55.7.353
4. Bruzelius, K., & Mba, D. (2004). An initial investigation on the potential applicability of Acoustic Emission to rail track fault detection. NDT & E International, 37(7), 507-516. https://doi.org/10.1016/j.ndteint.2004.02.001
5. Coccia, S., Bartoli, I., Marzani, A., di Scalea, F. L., Salamone, S., & Fateh, M. (2011). Numerical and experimental study of guided waves for detection of defects in the rail head. NDT & E International, 44(1), 93-100. https://doi.org/10.1016/j.ndteint.2010.09.011
6. Coccia, S., Phillips, R., Nucera, C., Bartoli, I., Salamone, S., di Scalea, F. L., Fateh, M., & Carr, G. (2011). UCSD/FRA Non-contact Ultrasonic Guided-Wave System for Rail Inspection: An Update. Sensors and Smart Structures Technologies for Civil, Mechanical, and Aerospace Systems 2011, 7981. https://doi.org/10.1117/12.880238
7. Dare de Almeida, V. A., Guimaraes Baptista, F., & de Aguiar, P. R. (2015). Piezoelectric Transducers Assessed by the Pencil Lead Break for Impedance-Based Structural Health Monitoring. IEEE Sensors Journal, 15(2), 693-702. https://doi.org/10.1109/jsen.2014.2352171
8. de Oliveira, R., & Marques, A. T. (2008). Health monitoring of FRP using acoustic emission and artificial neural networks. Computers & Structures, 86(3-5), 367-373. https://doi.org/10.1016/j.compstruc.2007.02.015
9. Dehghan Niri, E., & Salamone, S. (2012). A probabilistic framework for acoustic emission source localization in plate-like structures. Smart Materials and Structures, 21(3). https://doi.org/10.1088/0964-1726/21/3/035009
10. Deutschl, E., Gasser, C., Niel, A., & Werschonig, J. (2004). Defect detection on rail surfaces by a vision based system. 2004 Ieee Intelligent Vehicles Symposium, 507-511. https://doi.org/10.1109/IVS.2004.1336435
11. Elements, E. (2019). The Wheels of Old Train on the Railway Track Passing By Camera. Close Up Shot. https://elements.envato.com/the-wheels-of-old-train-on-the-railway-track-passi-WDJX9ZB
12. Ensminger, D., & Bond, L. J. (2011). Ultrasonics (3rd Edition ed.). https://doi.org/10.1201/b11173
13. Fischer, B. (2016). Optical microphone hears ultrasound. Nature Photonics, 10(6), 356-358. https://doi.org/10.1038/nphoton.2016.95
14. Hamstad, M. A. (2007). Acoustic Emission Signals Generated by Monopole (Pencillead Break) Versus Dipole Sources: Finite Element Modeling and Experiments. Journal of Acoustic Emission (Journal-AE), 25.
15. He, Z., Wang, Y., Yin, F., & Liu, J. (2016). Surface defect detection for high-speed rails using an inverse P-M diffusion model. Sensor Review, 36(1), 86-97. https://doi.org/10.1108/sr-03-2015-0039

16. Huang, M., Jiang, L., Liaw, P., & Brooks, C. (1998). Using acoustic emission in fatigue and fracture materials research. 50, 1-12. http://www.tms.org/pubs/journals/jom/9811/huang/
17. Lanza di Scalea, F., Rizzo, P., Coccia, S., Bartoli, I., Fateh, M., Viola, E., & Pascale, G. (2005). Non-contact ultrasonic inspection of rails and signal processing for automatic defect detection and classification. Insight - Non-Destructive Testing and Condition Monitoring, 47(6), 346-353. https://doi.org/10.1784/insi.47.6.346.66449
18. Lanza di Scalea, F., Zhu, X., Capriotti, M., Liang, A. Y., Mariani, S., & Sternini, S. (2018). Passive Extraction of Dynamic Transfer Function From Arbitrary Ambient Excitations: Application to High-Speed Rail Inspection From Wheel-Generated Waves. Journal of Nondestructive Evaluation, Diagnostics and Prognostics of Engineering Systems, 1(1), 011005. https://doi.org/10.1115/1.4037517
19. Lecun, Y., Bottou, L., Bengio, Y., & Haffner, P. (1998). Gradient-based learning applied to document recognition. Proceedings of the IEEE, 86(11), 2278-2324. https://doi.org/10.1109/5.726791
20. Li, D. (2018). Rail Crack Monitoring Using Acoustic Emission Technique Springer Singapore. https://doi.org/10.1007/978-981-10-8348-8
21. Li, D., Wang, Y., Yan, W., & Ren, W. (2021). Acoustic emission wave classification for rail crack monitoring based on synchrosqueezed wavelet transform and multi-branch convolutional neural network. Structural Health Monitoring-an International Journal, 20(4), 1563-1582. https://doi.org/10.1177/1475921720922797
22. Li, M., Wang, M., Ding, R., Deng, T., Fang, S., Lai, F., & Luoi, R. (2021). Study of acoustic emission propagation characteristics and energy attenuation of surface transverse wave and internal longitudinal wave of wood. Wood Science and Technology, 55(6), 1619-1637. https://doi.org/10.1007/s00226-021-01329-y
23. Li, Q., & Ren, S. (2012). A Real-Time Visual Inspection System for Discrete Surface Defects of Rail Heads. Ieee Transactions on Instrumentation and Measurement, 61(8), 2189-2199. https://doi.org/10.1109/tim.2012.2184959
24. Liu, Z., Li, W., Xue, F. Q., Xiafang, J. Y., Bu, B., & Yi, Z. (2015). Electromagnetic Tomography Rail Defect Inspection. Ieee Transactions on Magnetics, 51(10). https://doi.org/10.1109/TMAG.2015.2430283
25. Lopes, B. G., Alexandre, F. A., Lopes, W. N., Aguiar, P. R. d., Bianchi, E. C., & Viera, M. A. A. (2018). Study on the effect of the temperature in Acoustic Emission Sensor by the Pencil Lead Break Test 2018 13th IEEE International Conference on Industry Applications (INDUSCON),
26. Mariani, S., Nguyen, T., Zhu, X., & Lanza di Scalea, F. (2016). Field Test Performance of Noncontact Ultrasonic Rail Inspection System. 143, 040170071-0401700714. https://doi.org/10.1061/JTEPBS.0000026.
27. Nivesrangsan, P. (2004). Multi-source, multi-sensor approaches to diesel engine monitoring using acoustic emission Heriot-Watt University].
28. Nivesrangsan, P., Steel, J. A., & Reuben, R. L. (2007). Source location of acoustic emission in diesel engines. Mechanical Systems and Signal Processing, 21(2), 1103-1114. https://doi.org/10.1016/j.ymssp.2005.12.010
29. Office of Railroad Policy and Development. (2011). Rolling contact fatigue: A comprehensive review.

https://railroads.dot.gov/sites/fra.dot.gov/files/fra_net/89/TR_Rolling_Contact_Fatigue_Comprehensive_Review_final.pdf
30. Office of Railroad Safety. (2015). Track Inspector Rail Defect Reference Manual. 1-82. www.fra.dot.gov/Elib/Document/15669
31. Papaelias, M. P., Roberts, C., Davis, C. L., Blakeley, B., & Lugg, M. (2010). Further developments in high-speed detection of rail rolling contact fatigue using ACFM techniques. Insight, 52(7), 358-360. https://doi.org/10.1784/insi.2010.52.7.358
32. Peng, Z. K., & Chu, F. L. (2004). Application of the wavelet transform in machine condition monitoring and fault diagnostics: a review with bibliography. Mechanical Systems and Signal Processing, 18(2), 199-221. https://doi.org/10.1016/S0888-3270(03)00075-X
33. Pollock, A. A. (1986). Classical wave theory in practical AE testing. The 8th International Acoustic Emission Symposium,
34. Rizzo, P., Coccia, S. (2009). Noncontact rail monitoring by ultrasonic guided waves. Encyclopedia of Structural Health Monitoring, 2397. https://doi.org/10.1002/9780470061626.shm041
35. Rohringer, W., Heine, T., Sommerhuber, R., Lehmann, N., & Fischer, B. (2018). Optical Microphone as Laser-Ultrasound Detector DAGA 2018 München,
36. Sadeghi, F., Jalalahmadi, B., Slack, T. S., Raje, N., & Arakere, N. K. (2009). A Review of Rolling Contact Fatigue. Journal of Tribology-Transactions of the Asme, 131(4), 041403. https://doi.org/10.1115/1.3209132
37. Sadoudi, L., Moulin, E., Assaad, J., Benmeddour, F., Bocquet, M., & Hillali, Y. E. (2016). Experimental Study of Acoustic Noise Correlation Technique for Passive Monitoring of Rails. Materials Sciences and Applications, 07(12), 848-862. https://doi.org/10.4236/msa.2016.712065
38. Thomas Heckel, H.-M. T., Marc Kreutzbruck & Sven Rühe. (2009). High speed non-destructive rail testing with advanced ultrasound and eddy-current testing techniques. NDTIP Proceedings, Prague.
39. Thomas, H. M., Heckel, T., & Hanspach, G. (2007). Advantage of a combined ultrasonic and eddy current examination for railway inspection trains. Insight, 49(6), 341-344. https://doi.org/10.1784/insi.2007.49.6.341
40. Xiong, Z., Li, Q., Mao, Q., & Zou, Q. (2017). A 3D Laser Profiling System for Rail Surface Defect Detection. Sensors (Basel), 17(8), 1791-1810. https://doi.org/10.3390/s17081791
41. Yan, R. Q., Gao, R. X., & Chen, X. F. (2014). Wavelets for fault diagnosis of rotary machines: A review with applications. Signal Processing, 96, 1-15. https://doi.org/10.1016/j.sigpro.2013.04.015
42. Zhang, X., Cui, Y., Wang, Y., Sun, M., & Hu, H. (2018). An improved AE detection method of rail defect based on multi-level ANC with VSS-LMS. Mechanical Systems and Signal Processing, 99, 420-433. https://doi.org/10.1016/j.ymssp.2017.06.029
43. Zhang, X., Feng, N., Wang, Y., & Shen, Y. (2014). An analysis of the simulated acoustic emission sources with different propagation distances, types and depths for rail defect detection. Applied Acoustics, 86, 80-88. https://doi.org/10.1016/j.apacoust.2014.06.004
44. Zhang, X., Feng, N., Wang, Y., & Shen, Y. (2015). Acoustic emission detection of rail defect based on wavelet transform and Shannon entropy. Journal of Sound and Vibration, 339, 419-432. https://doi.org/10.1016/j.jsv.2014.11.021

45. Zumpano, G., & Meo, M. (2006). A new damage detection technique based on wave propagation for rails. International Journal of Solids and Structures, 43(5), 1023-1046. https://doi.org/10.1016/j.ijsolstr.2005.05.006

ACKNOWLEDGEMENTS

This study was conducted with the support from the USDOT Tier 1 University Transportation Center on Railroad Sustainability and Durability.

ABOUT THE AUTHOR

Lei Jia, M.S.

Mr. Lei Jia is a Ph.D. student working on this research project. He has acquired multiple certifications in Python, Ruby, and Java, and applied them to solve challenging problems in railway non-contact health inspection. His current research focuses on developing and testing novel methods and algorithms for detecting and analyzing rail defects and anomalies using dynamic testing and machine learning techniques. He obtained his MS degree from Jiangsu University.

Jee Woong Park, Ph.D.

Dr. Jee Woong Park is Associate Professor of Civil and Environment Engineering and Construction. He is specialized in construction management, asset management, construction automation, and informatics. He has his MS degree from Stanford University and his Ph.D. from Georgia Tech.

Ming Zhu, Ph.D.

Dr. Ming Zhu is the Electrical Engineering Laboratory Director of the Department of Electrical and Computer Engineering at the University of Nevada Las Vegas. His research interests include circuits and VLSI design, robotics and automation, AI/machine learning algorithms and applications, computer and network architectures, computation algorithms and system design. He has a Ph.D. in Electrical Engineering from the University of Nevada Las Vegas.

Yingtao Jiang, Ph.D.

Dr. Yingtao Jiang is a professor in the Department of Electrical and Computer Engineering at the University of Nevada, Las Vegas. His research interests include semiconductors, microelectronics, computer-aided design, unmanned vehicle systems and applications, AI/machine learning algorithms and applications, sensors and instrumentations, computer architectures, wireless communications and STEM education. He has a Ph.D. in Computer Science from the University of Texas at Dallas.

\

Lihao Qiu, M.S.

Mr. Lihao Qiu was a MS student and is a Ph.D. student in Electrical and Computer Engineering while he worked on this research project. His BS degree was from Shanghai Maritime University.

Hualiang (Harry) Teng, Ph.D.

Dr. Hualiang (Harry) Teng is a Professor of Civil and Environmental Engineering and Construction. He is specialized in railroad system, intelligent transportation system, and highway safety. He has his Ph.D. from Purdue University.